REPORT DOCUMENTATION PAGE

Form Approved OMB NO. 0704-0188

1. REPORT DATE (DD-MM-YYYY)	2. REPORT TYPE	3. DATES COVERED (From - To)
12-04-2011	Final Report	1-Sep-2009 - 31-Mar-2010

4. TITLE AND SUBTITLE
Gradient-Index Optics Final Report

5a. CONTRACT NUMBER

5b. GRANT NUMBER
W911NF-09-C-0077

5c. PROGRAM ELEMENT NUMBER
8620AV

6. AUTHORS
Narkis Shatz, Ph.D

5d. PROJECT NUMBER

5e. TASK NUMBER

5f. WORK UNIT NUMBER

7. PERFORMING ORGANIZATION NAMES AND ADDRESSES
SAIC
Science Applications International Corporation (SAIC)
10260 Campus Point Dr.
San Diego, CA 92121 -

8. PERFORMING ORGANIZATION REPORT NUMBER

9. SPONSORING/MONITORING AGENCY NAME(S) AND ADDRESS(ES)
U.S. Army Research Office
P.O. Box 12211
Research Triangle Park, NC 27709-2211

10. SPONSOR/MONITOR'S ACRONYM(S)
ARO

11. SPONSOR/MONITOR'S REPORT NUMBER(S)
56484-PH-DRP.1

12. DISTRIBUTION AVAILIBILITY STATEMENT
Approved for Public Release; Distribution Unlimited

13. SUPPLEMENTARY NOTES
The views, opinions and/or findings contained in this report are those of the author(s) and should not contrued as an official Department of the Army position, policy or decision, unless so designated by other documentation.

14. ABSTRACT
SAIC has performed an effort to advance the state of the art in gradient-index (GRIN) nanolayered polymer optics. The goal of this study was to take significant risks off the table with regard to practical high-performance GRIN optical designs. The DARPA BOSS program had demonstrated a remarkable ability to finely control the behavior of light passing through a GRIN lens composed of hundreds of thousands of polycarbonate and acrylic plastic layers. The generalization of existing advanced imaging and nonimaging design capabilities to incorporate

15. SUBJECT TERMS
Imaging Optics, Nonimaging Optics, Gradient Index Optics, Camera, Concentrator, Night Vision

16. SECURITY CLASSIFICATION OF:			17. LIMITATION OF ABSTRACT	15. NUMBER OF PAGES	19a. NAME OF RESPONSIBLE PERSON
a. REPORT	b. ABSTRACT	c. THIS PAGE			Narkis Shatz
UU	UU	UU	UU		19b. TELEPHONE NUMBER: 858-826-6282

Report Title

Gradient-Index Optics Final Report

ABSTRACT

SAIC has performed an effort to advance the state of the art in gradient-index (GRIN) nanolayered polymer optics. The goal of this study was to take significant risks off the table with regard to practical high-performance GRIN optical designs. The DARPA BOSS program had demonstrated a remarkable ability to finely control the behavior of light passing through a GRIN lens composed of hundreds of thousands of polycarbonate and acrylic plastic layers. The generalization of existing advanced imaging and nonimaging design capabilities to incorporate manufacturable GRIN lenses can provide imaging lens systems that are compact and lightweight and concentrators that operate closer to the thermodynamic limit. We have built the most sophisticated polymer GRIN lens system to date - a lightweight, fast, SWIR GRIN lens based on performance metrics consistent with Army Night Vision Lab (NVL) portable imaging programs.

List of papers submitted or published that acknowledge ARO support during this reporting period. List the papers, including journal references, in the following categories:

(a) Papers published in peer-reviewed journals (N/A for none)

Number of Papers published in peer-reviewed journals: 0.00

(b) Papers published in non-peer-reviewed journals or in conference proceedings (N/A for none)

Number of Papers published in non peer-reviewed journals:

(c) Presentations

Number of Presentations:

Non Peer-Reviewed Conference Proceeding publications (other than abstracts):

Number of Non Peer-Reviewed Conference Proceeding publications (other than abstracts):

Peer-Reviewed Conference Proceeding publications (other than abstracts):

Number of Peer-Reviewed Conference Proceeding publications (other than abstracts):

(d) Manuscripts

Number of Manuscripts:

Patents Submitted

Patents Awarded

Awards

Graduate Students

NAME	PERCENT_SUPPORTED

FTE Equivalent:
Total Number:

Names of Post Doctorates

NAME	PERCENT_SUPPORTED

FTE Equivalent:
Total Number:

Names of Faculty Supported

NAME	PERCENT_SUPPORTED

FTE Equivalent:
Total Number:

Names of Under Graduate students supported

NAME	PERCENT_SUPPORTED

FTE Equivalent:
Total Number:

Student Metrics

This section only applies to graduating undergraduates supported by this agreement in this reporting period

The number of undergraduates funded by this agreement who graduated during this period: .....
The number of undergraduates funded by this agreement who graduated during this period with a degree in science, mathematics, engineering, or technology fields:.....
The number of undergraduates funded by your agreement who graduated during this period and will continue to pursue a graduate or Ph.D. degree in science, mathematics, engineering, or technology fields:.....
Number of graduating undergraduates who achieved a 3.5 GPA to 4.0 (4.0 max scale): .....
Number of graduating undergraduates funded by a DoD funded Center of Excellence grant for Education, Research and Engineering: .....
The number of undergraduates funded by your agreement who graduated during this period and intend to work for the Department of Defense .....
The number of undergraduates funded by your agreement who graduated during this period and will receive scholarships or fellowships for further studies in science, mathematics, engineering or technology fields: .....

Names of Personnel receiving masters degrees

NAME

Total Number:

Names of personnel receiving PHDs

NAME
Total Number:

Names of other research staff

NAME	PERCENT SUPPORTED
FTE Equivalent:	
Total Number:	

Sub Contractors (DD882)

Inventions (DD882)

Scientific Progress

Technology Transfer

Gradient-Index Optics

Final Report

March 31, 2010

Contract W911NF-09-C-0077
Issued by US ARMY RDECOM ACQCTR-W911-NF

Narkis Shatz, Ph.D.
Principal Investigator

Science Applications International Corp.
10260 Campus Point Dr. MS C4
San Diego, CA 92121

Table of Contents

Executive Summary

SAIC has teamed with Case Western Reserve University, the Naval Research Laboratory, Optical Research Associates and the University of Rochester to perform an effort to advance the state of the art in gradient-index (GRIN) nanolayered polymer optics. This effort culminated in a workshop, where hardware was demonstrated. The goal of this study was to take significant risks off the table with regard to practical high-performance GRIN optical designs.

The DARPA BOSS program had demonstrated a remarkable ability to finely control the behavior of light passing through a GRIN lens composed of hundreds of thousands of polycarbonate and acrylic plastic layers. The generalization of existing advanced imaging and nonimaging design capabilities to incorporate manufacturable GRIN lenses can provide imaging lens systems that are compact and lightweight without sacrificing performance, and concentrators for solar concentrating photovoltaics and for sensor systems that operate closer to the thermodynamic limit and which have reduced thickness relative to comparable non-GRIN designs. Our imaging optics work looked at lens design for camera-type applications and the nonimaging work looked at new algorithms which are required for developing solar photovoltaic designs. The imaging design approach enhanced techniques developed at NRL and Optical Research Associates. The nonimaging design approach looked to generalize established techniques of advanced nonimaging optical design, such as the edge-ray method, the simultaneous multiple-surface (SMS) method, global optimization, and the recent SAIC-developed generalized functional (GF) method.

We have built the most sophisticated polymer GRIN lens system to date. We have designed, developed, and delivered a lightweight, fast, SWIR GRIN lens based on performance metrics consistent with Army Night Vision Lab (NVL) portable imaging programs. This is a natural transition path for the GRIN lens technology as it simultaneously leverages the GRIN materials advantages in the SWIR, the expertise developed under the DARPA BOSS program in designing SWIR GRIN optics, and the emerging-technology state-of-the-art in SWIR detection. Furthermore this has demonstrated the advantages of the GRIN optics specifically for the needs of a potential customer. This lens will provide an attractive alternative to current lenses for fielded, portable SWIR systems and illustrates the advantages of the GRIN systems. The specifications for the lens were determined from preliminary designs in consultation with NVL. The proposed GRIN optics was based upon existing design tools and fabrication techniques in order to meet the 6 month timeline for assembly of the finished lens.

SAIC has developed a GRIN ray tracing algorithm to be used in global optimization and performance analysis of its GRIN nonimaging concentrators. In addition, we have made significant progress in developing a versatile parametrization scheme for use in globally optimizing GRIN lens designs. The parametrization scheme is the mathematical model that specifies a unique lens design for each set of specific values of N optimization parameters that define an N-dimensional design space to be searched by the global-optimization algorithm. The parametrization scheme we are developing is a generalization of the two-dimensional simultaneous multiple surface method. We believe that this parametrization scheme will be of

significant value in designing globally-optimized high-performance achromatic lenses for use as concentrators as well as for imaging applications.

ORA has implemented a polynomial representation of a spherical/cylindrical Gradient Refractive IndexGRIN in LightTools to describe the revolutionary materials developed by Case Western Reserve University and researchers at the Naval Research Laboratories. This implantation in an industry standard software package will allow users to easily design optical systems with the new class of materials. The polynomial function and the graphical user-interface (GUI) in LightTools are described in detail.

The University of Rochester has documented work on GRIN dispersion for use in spectrometers, and GRIN optics for curved image plane design, such as an intraocular lens. Techniques for modeling and accurately measuring GRIN components are presented, and additional GRIN optics research and potential applications are also presented.

The SAIC team has succeeded in meeting the project goals in a short time frame, with little existing infrastructure. This is a testament to the promise of the polymer GRIN technology. Despite the nascent state of sophistication, we were able to develop a design and execute all the stages of prototype fabrication to deliver a f/1.5, 18.5 mm focal length SWIR lens with a 35° field of view for a C-mount camera with 25 um pixel resolution – all with a 7.7 g mass. By contrast, the StingRay optics has a mass of 57.7 g: 7.5 times heavier. Our GRIN seedling lens performed equally well as the StingRay lens, with 40% fewer lens elements and nearly ¼ the volume. Figure 1 is a picture of the two lenses placed next to each other.

Figure 1: Picture of the StingRay lens (foreground) compared to the GRIN lens developed in this program. The StingRay lens weighs in at 57.74 g, while the GRIN lens weighs 7.74 g.

SAIC Final Report

1. INTRODUCTION

SAIC has developed a GRIN ray tracing algorithm to be used in global optimization and performance analysis of its L-GRIN (layered GRIN) nonimaging concentrators. In addition, we have developed a versatile parametrization scheme for use in globally optimizing L-GRIN lens designs. The parametrization scheme is the mathematical model that specifies a unique lens design for each set of specific values of N optimization parameters that define an N-dimensional design space to be searched by the global-optimization algorithm. The parametrization scheme we are developing is a generalization of the two-dimensional simultaneous multiple surface method. We believe that this parametrization scheme will be of significant value in designing globally-optimized high-performance achromatic lenses for use as concentrators as well as for imaging applications. We discuss two important special cases of the parametrization scheme: the L-GRIN singlet and the L-GRIN cemented doublet.

2. GRIN RAY-TRACING ALGORITHM

For this project the refractive-index distributions for all GRIN components are assumed to be spherically symmetric. This means that the refractive index inside the GRIN material is a function only of the radial coordinate r in a spherical coordinate system. We designate this radial refractive-index function as $n(r)$. The surfaces of constant refractive index for such a GRIN material are concentric spheres centered on a common center, as shown in Figure 2. Although the index distribution is spherically symmetric, the optical surfaces themselves are allowed to be aspherical.

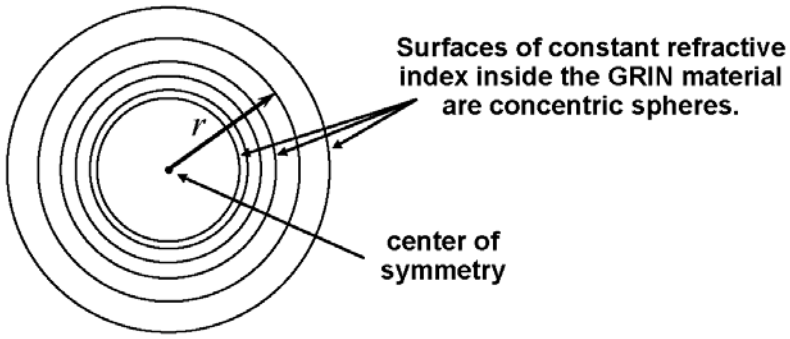

Figure 2. Spherically symmetric refractive-index distribution.

Due to the spherical symmetry of the index distribution, each ray path inside the GRIN material is confined to a plane containing the center of symmetry of the distribution. Because the ray path is confined to a plane, the formula for the shape of the path is two-dimensional. The method we use to compute the ray path is closely related to a method described by Brizard.[1] The solution for the ray path is based on Fermat's Principle, which states that light propagating from point A to point B in a non-uniform medium follows a path that minimizes the travel time between the two points. The calculus of variations is used to derive a formula for the propagation path that

minimizes the travel time. The ray-path geometry in the plane containing the path itself and the center of symmetry of the GRIN material is illustrated in Figure 3.

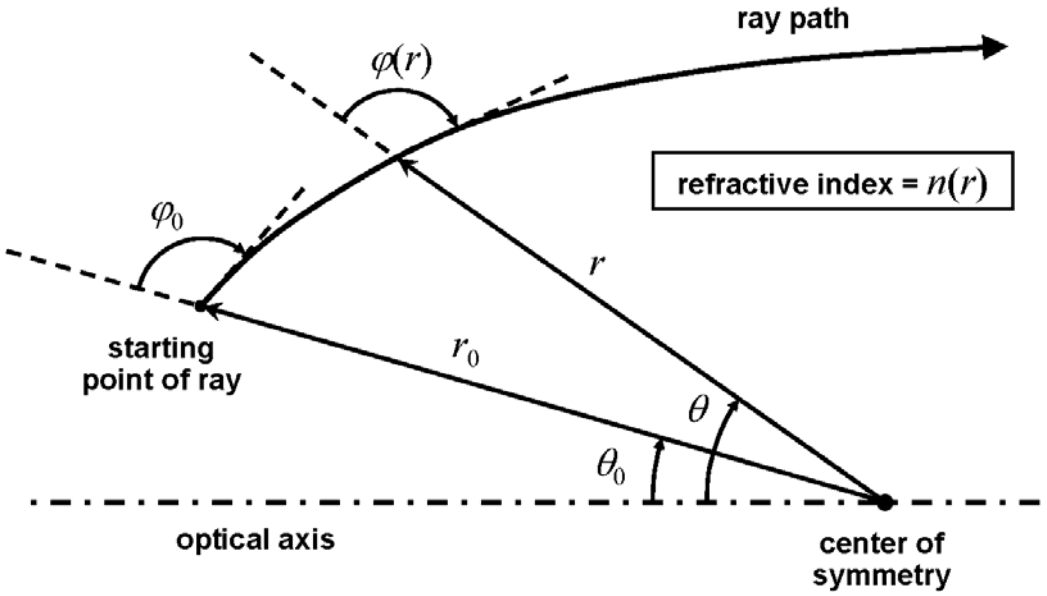

Figure 3. Geometry of ray path within a spherically-symmetric GRIN medium.

We define the r,θ-coordinate system such that the radial coordinate r is the distance from the center of symmetry and the angular coordinate θ is measured relative to the optical axis. We also define the ray-propagation direction $\varphi(r)$ for each point on the ray path, as shown in Figure 2. The ray's starting point is defined by the initial radial and angular coordinates r_0 and θ_0, respectively, as well as the initial ray-propagation direction φ_0. Using the calculus of variations, we find that the geometry of the ray path can be expressed in the form

$$\theta(r) = \theta_0 + \text{sign}(\tfrac{\pi}{2} - \varphi_0) \cdot n_0 r_0 \sin(\varphi_0) \int_{r_0}^{r} \frac{d\rho}{\rho \sqrt{n^2(\rho)\rho^2 - n_0^2 r_0^2 \sin^2(\varphi_0)}}, \tag{1}$$

where n_0 is the refractive index of the GRIN material at the starting point of the ray. For a general radial index distribution $n(r)$ we can obtain the ray path by numerical integration of Eq. (1). The function $\theta(r)$ must then be inverted to obtain the ray-path function $r(\theta)$. It would be more convenient in practice to be able to compute the function $r(\theta)$ directly. Another problem with Eq. (1) is that the singularity that occurs when

$$\rho = \frac{n_0 r_0 \left|\sin(\varphi_0)\right|}{n(\rho)} \tag{2}$$

can cause difficulties in performing the numerical integration. For ray tracing, an alternative form of the solution for the ray path is more convenient. Specifically, we use the first-order differential equation

$$\frac{dr}{d\theta} = \frac{\text{sign}(\tfrac{\pi}{2} - \varphi_0)}{n_0 r_0 \sin(\varphi_0)} \cdot r \sqrt{n^2(r) r^2 - n_0^2 r_0^2 \sin^2(\varphi_0)}, \tag{3}$$

which is the differential equation from which Eq. (1) was derived. To compute the ray path, we integrate Eq. (3) directly using standard techniques for the numerical solution of differential equations. Once the ray path has been computed, the ray direction at any point on the path can be obtained from the formula

$$\sin[\varphi(r)] = \frac{n_0 r_0 \sin(\varphi_0)}{n(r) r} . \tag{4}$$

While it is true that the ray direction could be estimated from the computed function n(r), Eq. (4) should, in general, provide more accurate results.

We now present three examples of ray paths computed by solving Eq. (3) numerically using a standard fixed-step Runge-Kutta method. We also compute the solution exactly in each case, so that the accuracy of the numerical solution can be determined.

For our first example, we consider the constant-index plano-convex lens depicted in Figure 4. This lens has a 20-mm-radius spherical front surface, a planar back surface, and a thickness of 10 mm. The refractive index is 1.5 inside the lens and 1.0 outside. The starting point of the ray traced through this plano-convex lens was defined by the initial conditions r_0 = 30 mm, θ_0 = 20°, and φ_0 = 157°. Using numerical solution of Eq. (3) with the radial index function of Figure 5, the ray was traced from its initial location, through the spherical surface, to its intersection with the planar surface. Snell's law was then used to trace the ray through the planar surface to the point at which the ray intersects the optical axis. For comparison with the numerically-computed ray path, we also calculated the entire ray path exactly using only Snell's law. This exact calculation was made possible by the fact that the refractive index of the lens is constant.

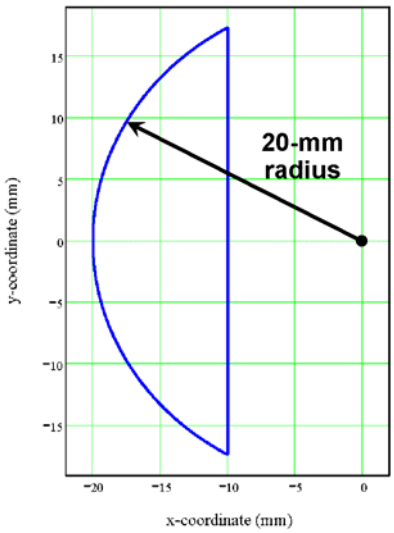

Figure 4. Constant-index plano-convex lens used as the first test case for the GRIN ray-tracing algorithm.

The numerically-computed ray path through the lens is shown in Figure 6. The ray tracing accuracy is depicted in Figure 7, which was obtained by plotting the difference between the numerically-computed and exact *y*-coordinates of the ray path as a function of the *x*-coordinate. A *y*-coordinate error of less than 0.06 μm was obtained over the entire ray path. However, to achieve this low error level, a relatively computationally-intensive 20,000-step numerical

integration was required. The reason such a large number of steps had to be used is that, for testing purposes, the GRIN ray tracing algorithm was used to trace the ray through the refractive-index discontinuity at the spherical lens surface. In practice, the GRIN ray tracing algorithm would only be used to trace rays through continuous index distributions, which requires far fewer steps to achieve a given level of ray tracing accuracy. At index discontinuities, the ray would, in practice, always be traced using Snell's law.

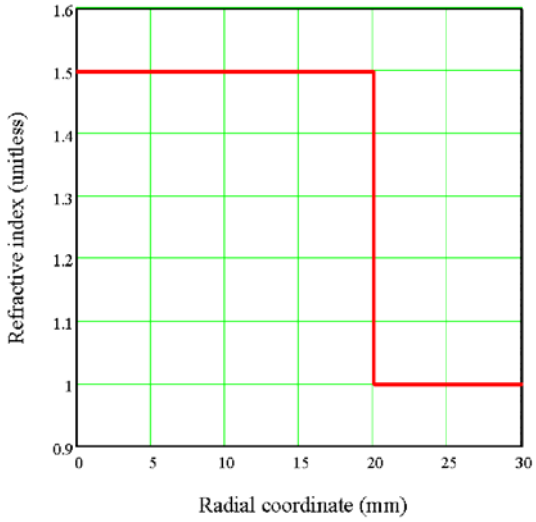

Figure 6. Radial index function used in computing the ray path from the initial ray location to the planar surface for the constant-index plano-convex lens.

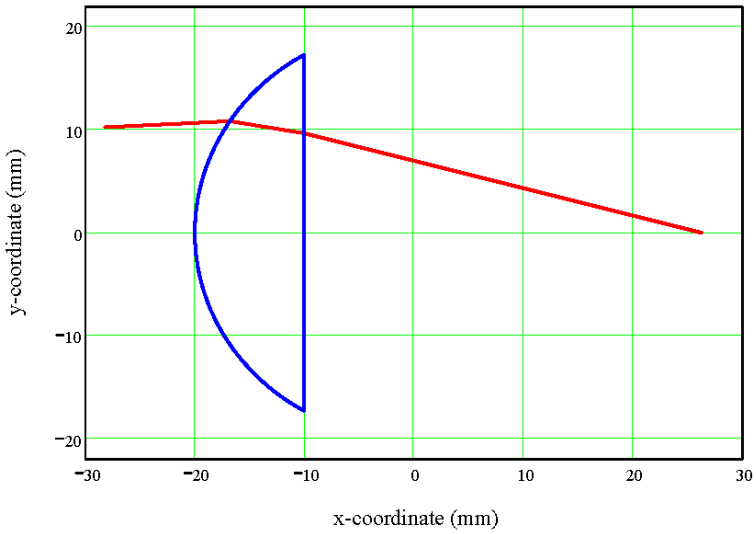

Figure 7. Computed ray path through the constant-index plano-convex lens.

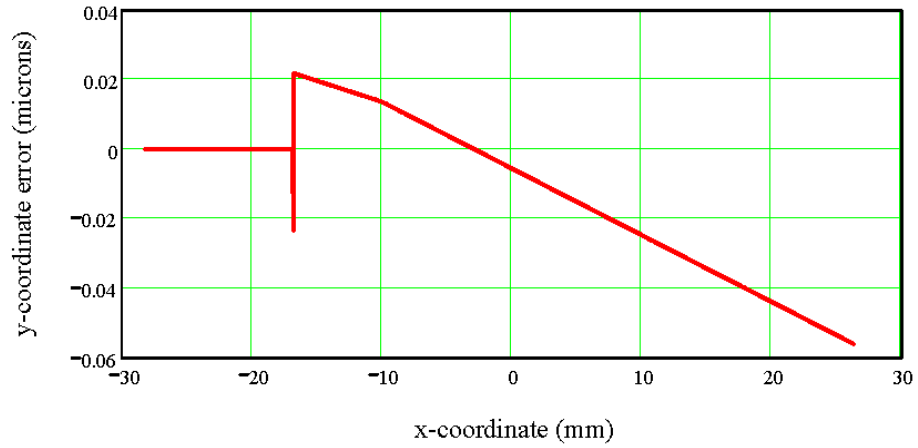

Figure 8. Error in y-coordinate for computed ray path through the constant-index plano-convex lens.

As a second example, we consider a GRIN lens having the same shape as in the first example (Figure 4), but with the inverse-*r*-dependent refractive-index distribution shown in Figure 8. The center of symmetry of the refractive-index distribution is located at the origin of Figure 4. The starting point of the ray traced through this plano-convex GRIN lens was defined by the initial conditions r_0 = 30 mm, θ_0 = 20°, and φ_0 = 157° (i.e., the same as in the first example). In this case we used Snell's law to trace the ray from its starting point, through the spherical surface, and into the lens. Inside the lens, we used numerical integration of Eq. (3) with the index function of Figure 8 to compute the ray path from the spherical surface to the planar surface. Snell's law was then used to trace the ray through the planar surface to the intersection with the optical axis. For comparison with the numerically-computed ray path, we also calculated the entire ray path exactly using Snell's law combined with an exact solution of Eq. (3) inside the lens. The exact solution inside the lens was made possible by the fact that the inverse-*r*-dependent radial distribution simplifies the form of Eq. (3) by canceling out the *r*-dependence inside the square root.

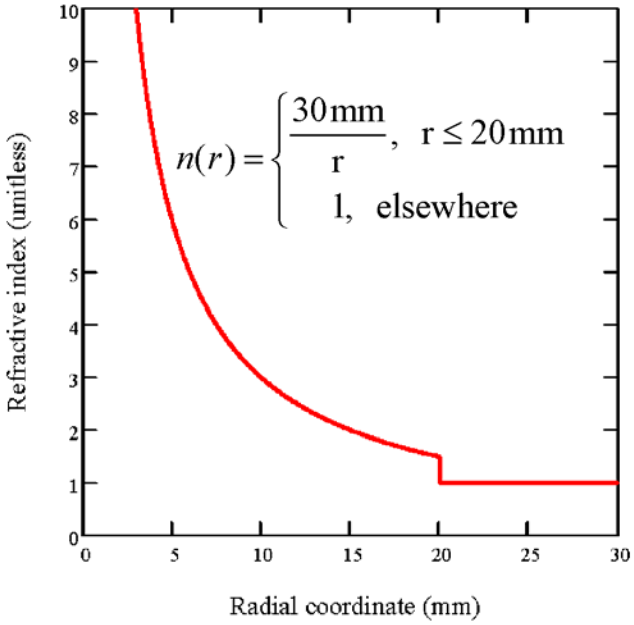

Figure 9. Radial refractive-index function for plano-convex GRIN lens.

The numerically-computed ray path through the lens is shown in Figure 9. The ray tracing accuracy is depicted in Figure 10, which, as in the first example, was obtained by plotting the difference between the numerically-computed and exact *y*-coordinates of the ray path as a function of the *x*-coordinate. A *y*-coordinate error of less than 0.05 μm was obtained over the entire ray path using only 250 steps for the numerical integration. The number of integration steps required was much lower than in the first example, due to the fact that Snell's law was used to trace the ray through the index discontinuity at the spherical surface, rather than attempting to use the GRIN formula for this purpose.

As our third and final example, we consider the 40-mm-diameter spherical GRIN lens shown in Figure 11. The GRIN distribution for this lens is the inverse-*r*-dependent refractive-index function shown in Figure 12. The center of symmetry of the refractive-index distribution is located at the origin of Figure 13, which also corresponds to the center of the spherical lens surface. The starting point of the ray traced through this spherical GRIN lens was defined by the initial conditions r_0 = 20 mm, θ_0 = 0°, and φ_0 = 91°. In this case, the ray started inside the GRIN medium and remained within it. The ray was traced from $\theta = \theta_0$ to θ = 3600° using numerical integration of Eq. (3). For comparison with the numerically-computed ray path, we also calculated the entire ray path using an exact solution of Eq. (3) inside the lens. As in the second example, the exact solution inside the lens was made possible by the fact that the inverse-*r*-dependent radial distribution simplifies the form of Eq. (3) by canceling out the *r*-dependence inside the square root.

The numerically-computed ray path through the lens is shown in Figure 14. The ray tracing accuracy is depicted in Figure 15, which was obtained by plotting the difference between the numerically-computed and exact *r*-coordinates of the ray path as a function of the θ-coordinate. An *r*-coordinate error of less than 0.06 μm was obtained over the entire ray path using only 150 steps for the numerical integration. The number of integration steps required was much lower

than in the first example, due to the fact that the numerical GRIN ray-tracing algorithm was not used to trace rays through any refractive-index discontinuities.

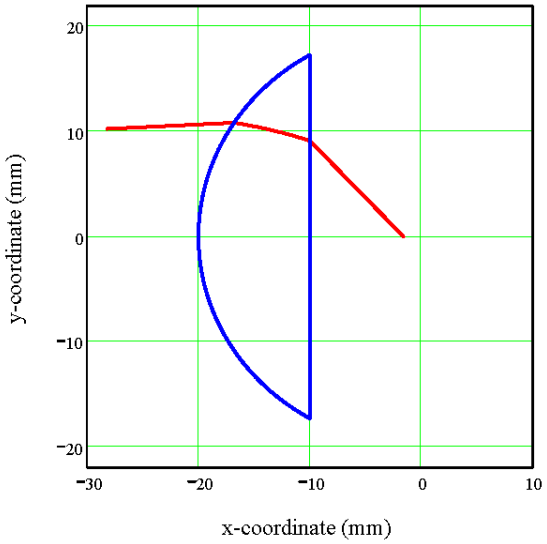

Figure 10. Computed ray path through the plano-convex GRIN lens.

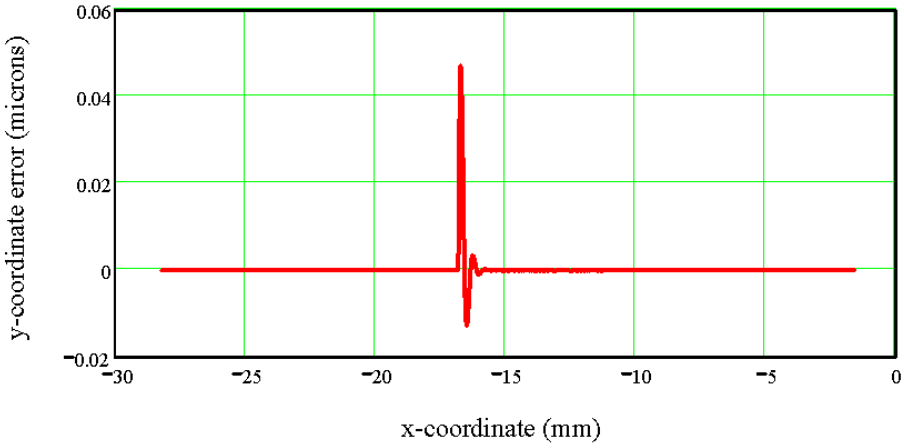

Figure 11. Error in y-coordinate for computed ray path through the plano-convex GRIN lens.

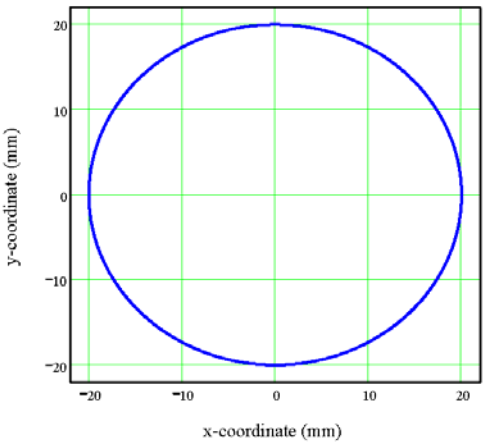

Figure 12. Spherical GRIN lens used as the third test case for the GRIN ray-tracing algorithm.

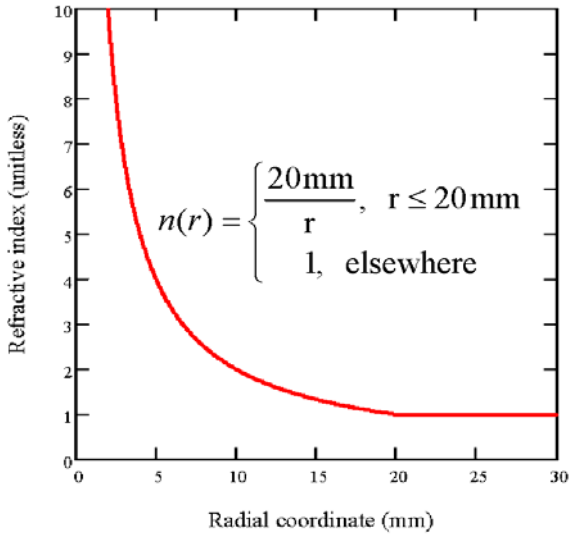

Figure 13. Radial refractive-index function for spherical GRIN lens.

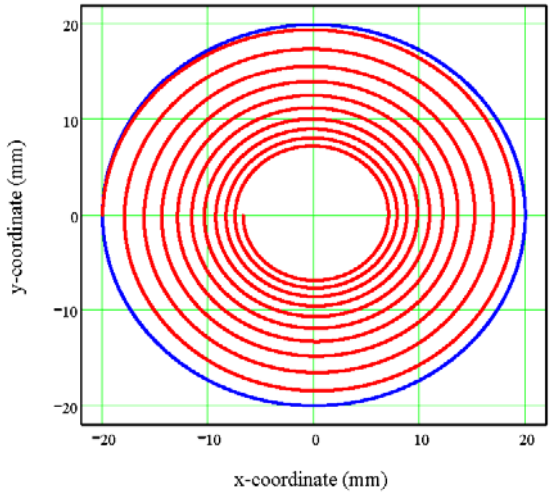

Figure 14. Computed ray path within the spherical GRIN lens.

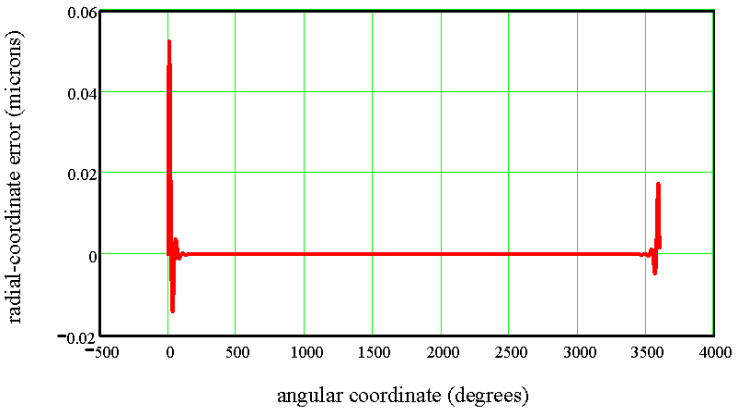

Figure 15. Error in the *r*-coordinate as a function of the angular coordinate θ for the computed ray path within the spherical GRIN lens.

3. PARAMETRIZATION SCHEME FOR GRIN-CONCENTRATOR OPTIMIZATION

The parametrization scheme developed under Phase 1 for use in designing L-GRIN nonimaging concentrators is based on a generalization of the two-dimensional simultaneous multiple surface (2D SMS) design method. This method should be capable of producing high-performance concentrator designs. Since it generates imaging-concentrator designs, it should also be capable of producing high-performance low-f-number achromatic imaging optics. The original 2D SMS method[2,3] allows one to design an optical component consisting of two axisymmetric (or bilaterally-symmetric and translationally-symmetric) aspheric optical surfaces which, for monochromatic meridional rays, together produce a perfect off-axis image of an infinitely distant off-axis point source located at a specific angular offset relative to the optical axis. Each of the two optical surfaces can be either reflective or refractive. For nonimaging applications, such lenses can be used in conjunction with a secondary concentrator to fully utilize the available target phase space. Alternatively, incorporation of two or more air-spaced lenses into the generalized 2D SMS method itself should accomplish the same purpose.

In the original 2D SMS method, it is required that the rays propagate in a constant-refractive-index medium both before and after refraction (or reflection) at each of the two optical surfaces. To generalize the 2D SMS method for use in designing GRIN lenses, we need to remove the restriction that rays must propagate in constant-index media after intersecting the first SMS surface and prior to intersecting the second SMS surface. Since we are interested in designing lenses in this project, we consider only refractive optical surfaces. That is, we assume that no reflective optical surfaces are involved in the design. We begin with a non-isotropic axisymmetric optical medium, with its symmetry axis corresponding to the desired optical axis of the SMS lens to be designed. In its most general form, this non-isotropic medium can include any combination of axisymmetric GRIN materials, constant-index materials, and axisymmetric aspheric optical surfaces that define interfaces between the different materials involved. Air gaps are allowed to be included as part of this medium. We assume that a set of N_{medium} real parameters completely specifies the characteristics of the non-isotropic medium, where N_{medium} is a finite positive integer. Any or all of these N_{medium} parameters can be varied by the global optimization algorithm during its search for an optimal optical design.

The generalized 2D SMS lens will take the form depicted notionally in Figure 16. The lens will be designed to concentrate flux incident from the left of SMS surface #1 within a specified acceptance angle onto a target located to the right of SMS surface #2. The refractive indices to the left and right of the lens are assumed to be unity (i.e., air) and n_0, respectively. In the case of a non-immersed target, we have $n_0 = 1$.

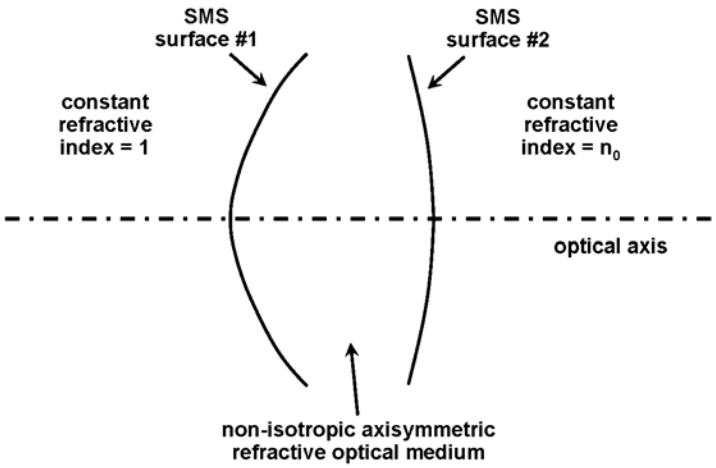

Figure 16. Notional depiction of generalized 2D SMS lens.

We now describe the method to be used to design a generalized 2D SMS lens. Before designing the lens, we must select a set of specific values of the N_{medium} parameters that specify the non-isotropic axisymmetric optical medium. This represents a single point in the N_{medium}-dimensional parameter space that defines the family of allowed non-isotropic optical media. The required acceptance angle of the lens is θ_{acc}, measured relative to the optical axis. The first SMS surface is required to intersect the optical axis at $x = x_a$, where the optical axis is coincident with the x-axis. The upper edge of the target is located at $(x,y) = (x_t,y_t)$, where y is the coordinate orthogonal to the optical axis. The thickness of the lens is controlled by specifying the desired value of the optical path length Φ_0 for propagation between the two SMS surfaces of a ray incident on SMS surface #1 at the optical axis and initially propagating in air at the acceptance angle relative to the optical axis. Optical path length is defined as the integral along the ray path of the propagation distance times the refractive index. Finally, we must select a specific wavelength value λ_{SMS} for which the lens is to be designed. The design process can then be described as the following series of steps:

Step 1. We begin this Step by defining a planar wavefront of wavelength λ_{SMS} propagating towards the lens at the acceptance angle θ_{acc}, as shown in Figure 17. A ray is traced perpendicular to this wavefront such that it intersects the first point on SMS surface #1, which lies on the optical axis at $x = x_a$. Due to the required symmetry of the lens, we know that SMS surface #1 must be perpendicular to the optical axis at this first point. Making use of this fact, we use Snell's law to trace the ray through SMS surface #1 and into the non-isotropic optical medium. Since we know the ray's initial position and direction within this medium, we can trace the ray through it, making use of the GRIN ray-tracing algorithm to trace the ray through any GRIN regions intersected by the ray. While tracing the ray, we keep track of the optical path length of that portion of the ray

path lying within the non-isotropic medium. By definition, the intersection of the ray with SMS surface #2 occurs when this optical path length equals the previously-specified value Φ_0. This fact allows us to find the first point on SMS surface #2. The tilt angle of SMS surface #2 at this point is determined using Snell's law and the condition that the ray must intersect the upper edge of the target at $(x,y) = (x_t,y_t)$. Once the ray has been traced from the wavefront, through the lens, and to the target, we compute the total optical path length Φ_{tot} corresponding to the complete ray path.

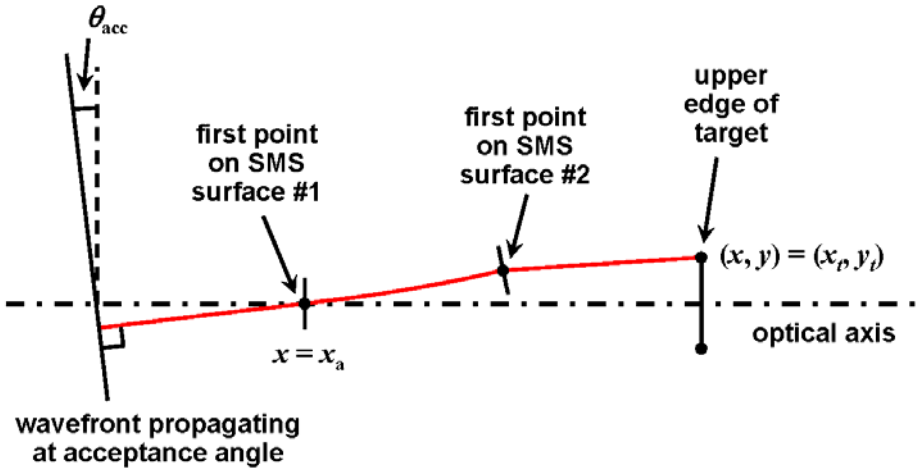

Figure 17. Step 1 in the process of designing the generalized 2D SMS lens. The traced ray, which propagates from left to right, is shown in red. Between SMS surfaces #1 and #2, the ray propagates within the non-isotropic refractive medium.

Step 2. We begin this Step by defining a planar wavefront propagating towards the lens at angle $-\theta_{acc}$, as shown in Figure 18. This wavefront must be defined such at it intersects the optical axis at the same x-coordinate as the wavefront defined in Step 1. We trace a ray from the lower edge of the target at position $(x,y) = (x_t,-y_t)$ to the first point on SMS surface #2. Based on the previously-computed tilt angle of SMS surface #2 at this point, we use Snell's law to trace the ray into the non-isotropic refractive medium. Since we know the ray's initial position and direction within this medium, we can trace the ray through it, making use of the GRIN ray-tracing algorithm to trace the ray through any GRIN regions intersected by the ray. We next need to determine the point along the ray path at which SMS surface #1 is intersected. To do this, we use the fact that when the ray exits SMS surface #1 it is required to propagate in a direction perpendicular to the planar wavefront oriented at angle $-\theta_{acc}$. Based on this requirement, we can compute the total optical path length of the ray from the target to the wavefront for different potential intersections with SMS surface #1. From Fermat's principle, we know that the correct intersection point must satisfy the requirement that the total optical path length be equal to Φ_{tot}. To determine the correct intersection point, we perform a one-dimensional search for the intersection point for which the ray's total optical path length from the lower edge of the source to the planar wavefront equals Φ_{tot}. Once the correct intersection point of the ray with SMS surface #1 has been obtained, Snell's law is used to compute the tilt angle of the surface at that point.

Step 3. In this Step we trace a ray from the original planar wavefront propagating towards the lens at the acceptance angle θ_{acc}, as shown in Figure 19. The ray is traced perpendicular to this wavefront such that it intersects the second point on SMS surface #1. Snell's law is used to trace the ray through SMS surface #1 and into the non-isotropic optical medium. Since we know the ray's initial position and direction within this medium, we can trace the ray through it, making use of the GRIN ray-tracing algorithm to trace the ray through any GRIN regions intersected by the ray. After intersecting SMS surface #2, we require that the ray must intersect the upper edge of the target. To determine the point along the ray path at which the ray intersects SMS surface #2, we perform a one-dimensional search to find the intersection point for which the total optical path length of the ray equals Φ_{tot}. Snell's law is then used to compute the tilt angle of SMS surface #2 at that point.

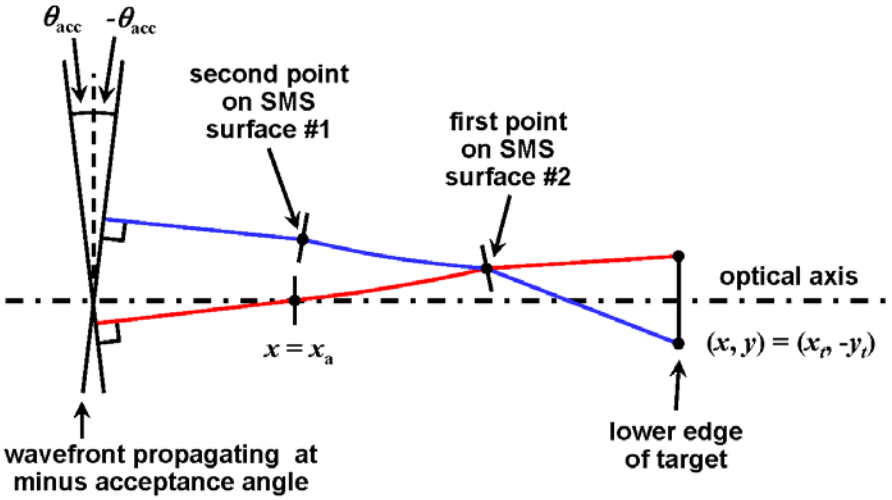

Figure 18. Step 2 in the process of designing the generalized 2D SMS lens. The traced ray, which propagates from right to left, is shown in blue. Between SMS surfaces #1 and #2, the ray propagates within the non-isotropic refractive medium. The previously traced ray is also shown.

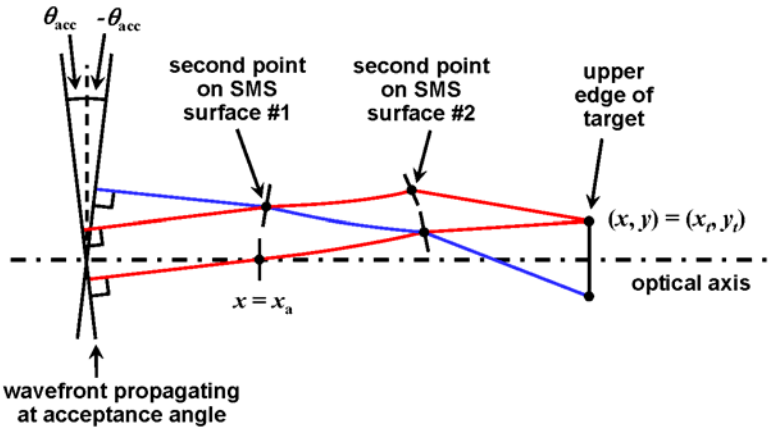

Figure 19. Step 3 in the process of designing the generalized 2D SMS lens. The traced ray, which propagates from left to right through the second point of each of the two SMS surfaces, is shown in red. Between SMS surfaces #1 and #2, the ray propagates within the non-isotropic refractive medium. The previously traced rays are also shown.

Step 4. In this Step, which is illustrated in Figure 20, we trace a ray from the lower edge of the target at position $(x,y) = (x_t,-y_t)$ to the second point on SMS surface #2. Based on the previously-computed tilt angle of SMS surface #2 at this point, we use Snell's law to trace the ray into the non-isotropic refractive medium. Since we know the ray's initial position and direction within this medium, we can trace the ray through it, making use of the GRIN ray-tracing algorithm to trace the ray through any GRIN regions intersected by the ray. We next need to determine the point along the ray path at which SMS surface #1 is intersected. To do this, we use the fact that when the ray exits SMS surface #1 it is required to propagate in a direction perpendicular to the planar wavefront oriented at angle $-\theta_{acc}$. Based on this requirement, we perform a one-dimensional search for the intersection point with SMS surface #1 for which the ray's total optical path length from the lower edge of the source to the planar wavefront equals Φ_{tot}. Once the correct intersection point of the ray with SMS surface #1 has been obtained, Snell's law is used to compute the tilt angle of the surface at that point.

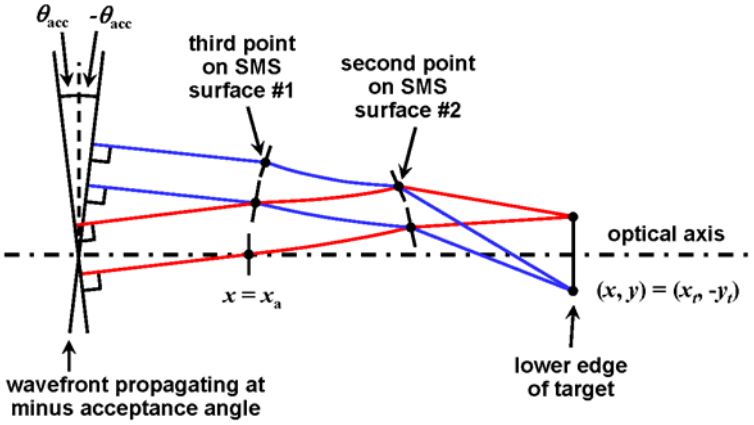

Figure 20. Step 4 in the process of designing the generalized 2D SMS lens. The traced ray, which propagates from right to left through the second point on SMS surface #2 and the third point on SMS surface #1, is shown in blue. Between SMS surfaces #1 and #2, the ray propagates within the non-isotropic refractive medium. The previously traced rays are also shown.

Step 5. At this point in the design process we alternately repeat steps analogous to Steps 3 and 4 until a series of points on both SMS surfaces have been generated that extend beyond the required aperture radius relative to the optical axis. Based on the required symmetry of the lens, we also generate sampled points below the optical axis. Associated with each point on each lens surface is a value of the tilt-angle (i.e., the slope) of the surface at that point. The result is illustrated notionally in Figure 21.

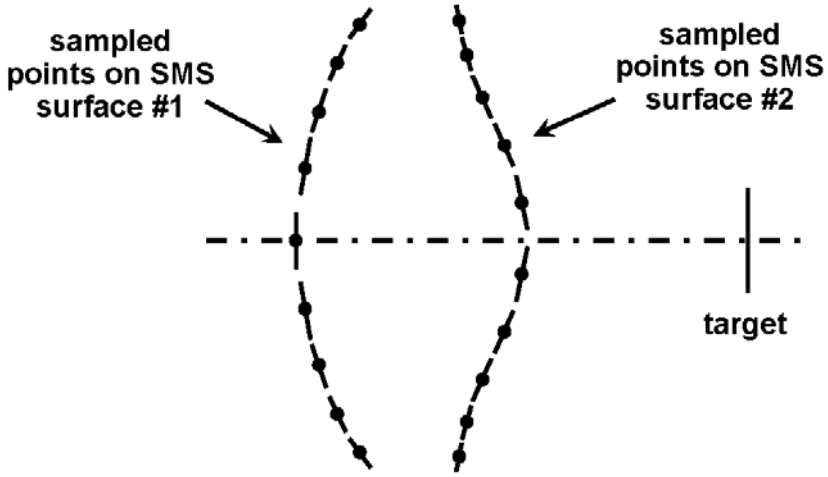

Figure 21. Set of sampled points and tilt angles on the two SMS surfaces obtained by means of Steps 1 – 5.

Step 6. Using Hermite-spline interpolation, which incorporates both position and slope information, we generate continuous versions of both SMS surfaces. The result is illustrated notionally in Figure 22.

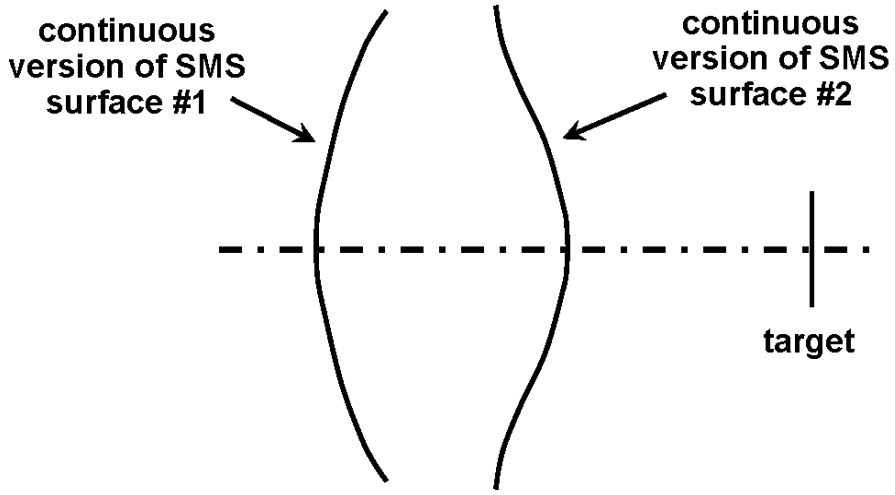

Figure 22. Continuous versions of the two SMS surfaces obtained by interpolation (Step 6).

The shapes of the two surfaces of the generalized 2D SMS lens will be recomputed once for each iteration of the global optimization process. After generating the shapes of these two surfaces, small deviations may, if desired, be added to one or both of the shapes to slightly perturb the design. The optimization parameters will include some or all of the following:

- The N_{medium} parameters that specify the non-isotropic axisymmetric optical medium.
- The x-coordinate x_a of SMS surface #1.
- The x-coordinate of the target, x_t, used in generating the SMS lens design. (In practice it is redundant to vary both x_a and x_t, so one can be held constant during the optimization process while the other is varied.)

- The half width y_t of the target.
- The acceptance angle θ_{acc} of the SMS lens.
- The optical path length parameter Φ_0 which controls the thickness of the SMS lens.
- The wavelength λ_{SMS} for which the lens is to be designed.
- The x-axis shift Δx_t of the target location, relative to x_t.
- Shape perturbations added to the two SMS surfaces after their shapes have been computed using the generalized 2D SMS design method.

The parametrization scheme outlined above provides should provide the flexibility required to design a wide range of high-performance achromatic GRIN lens designs for use in concentration (e.g., solar applications), projection (e.g., lighting applications), and imaging (e.g., cameras and other imaging sensors). It is capable of designing lenses of varying degrees of complexity, as required by the application. For example, it could be used to design GRIN singlets, GRIN cemented doublets, GRIN air-spaced doublets, and GRIN lenses with more than two elements.

4. SMS L-GRIN SINGLET LENS

We now describe an important special case of the parametrization scheme described in the previous section. Illustrated in Figure 23, this type of lens is referred to as an SMS L-GRIN singlet lens. It has only two optical surfaces, both of which are aspheric surfaces generated using the generalized 2D SMS method described in the previous section. Between these two optical surfaces is an L-GRIN material, with continuously varying refractive index as a function of position.

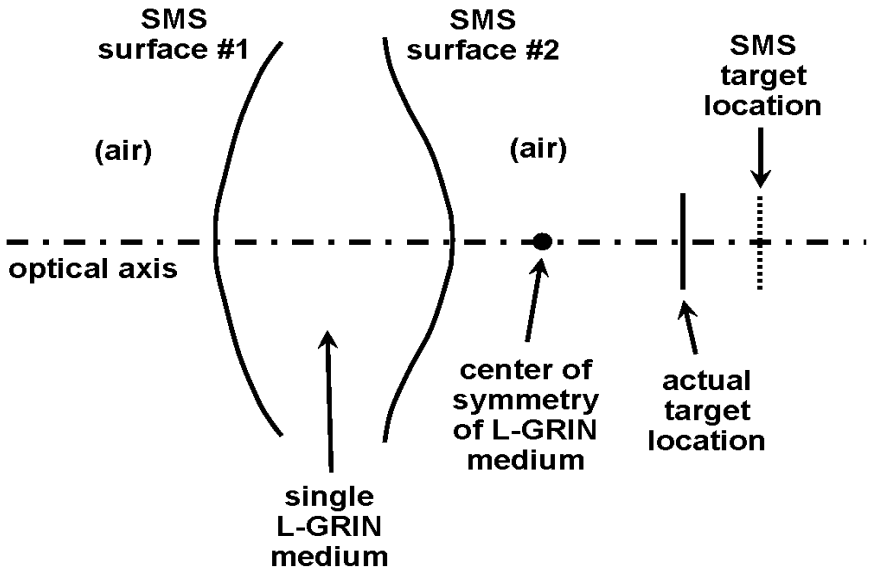

Figure 23. Notional depiction of geometry of SMS L-GRIN singlet lens.

The parametrization scheme for this lens must define the characteristics of the L-GRIN medium, the target position relative to the lens, and the shapes and spacing of the two SMS surfaces. The

L-GRIN medium is specified by providing the axial position x_{sym} of its center of symmetry and its L-GRIN material ratio $\tau(r)$ as a function of the distance r from the center of symmetry. The L-GRIN material ratio is defined in such a way that the effective refractive index of the medium takes the form

$$n_{GRIN}(r,\lambda) = \tau(r)n_1(\lambda) + [1-\tau(r)]n_2(\lambda), \tag{5}$$

where $n_1(\lambda)$ and $n_2(\lambda)$ are the refractive indices of the two L-GRIN materials as functions of the wavelength λ. The material ratio is defined such that its value is greater than or equal to zero and less than or equal to unity for all values of r. To specify the material-ratio function as part of the parametrization scheme, we use a finite number of spline knots, with cubic-spline interpolation between the points, as depicted in Figure 24. For r-values below the minimum r-value of the knots and above their maximum r-value, the material ratio is assumed to be a constant, as shown in Figure 22. Any portions of the interpolated curve that having τ-values less than zero they are set equal to zero. Similarly, any portions of the curve having τ-values greater than unity are set equal to unity.

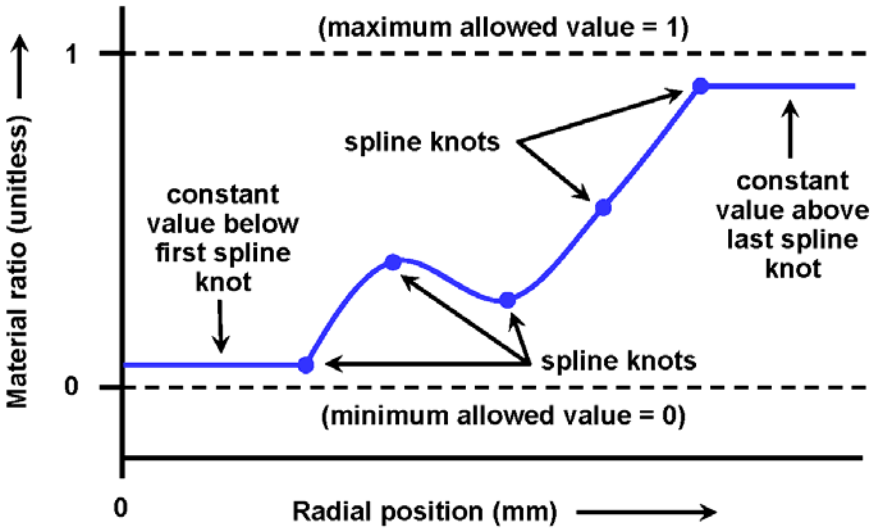

Figure 24. Parametrization scheme for the L-GRIN material ratio as a function of radial position using cubic-spline interpolation.

In addition to the parameters characterizing the L-GRIN medium, we must specify values for a number of other parameters in order to generate the shapes of the two SMS lens surfaces. These parameters include the axial position x_a of the SMS surface #1, the SMS axial target position x_t, the SMS target half width y_t, the acceptance angle θ_{acc}, the optical-path-length parameter Φ_0 controlling the thickness of the lens, and the wavelength λ_{SMS} used in generating the SMS design.

A lens designed using the generalized 2D SMS method described previously will provide ideal performance only for meridional rays having wavelength λ_{SMS}. Since the lens will need to operate with broadband light for both meridional and skew rays, we must perturb the single-wavelength, meridional design in order for the optimization algorithm to produce the best possible performance. To do this, we shift the target along the axis by the amount Δx_t and add

shape perturbations to the shape profiles of the two optical surfaces. The shape perturbations will take the form of cubic-spline functions, defined in such a way that the lens shape reverts to the exact single-wavelength, meridional SMS design when all the perturbations are set equal to zero.

To summarize, the parametrization scheme for the SMS L-GRIN singlet lens will utilize the following parameters:

- The axial position x_{sym} of the center of symmetry of the L-GRIN medium.
- The spline knots defining the material-ratio function of the L-GRIN medium.
- The x-coordinate x_a of SMS surface #1.
- The x-coordinate of the target, x_t, used in generating the SMS lens design. (In practice it is redundant to vary both x_a and x_t, so one can be held constant during the optimization process while the other is varied.)
- The half width y_t of the target.
- The acceptance angle θ_{acc} of the SMS lens.
- The optical path length parameter Φ_0 which controls the thickness of the SMS lens.
- The wavelength λ_{SMS} for which the lens is to be designed.
- The x-axis shift Δx_t of the target location, relative to x_t.
- Shape knots defining shape perturbations added to the two SMS surfaces after their shapes have been computed using the generalized 2D SMS design method.

We expect the total number of optimization parameters required to design a lens of this type will be on the order of 30. In other words, the global-optimization algorithm will be required to search a hyperspace having approximately 30 dimensions in order to find the design having optimal performance. Incorporating the generalized 2D SMS design method into the parametrization scheme as described above should significantly reduce the number of iterations required to find the global optimum, since it will insure that all points in the design space are relatively close to the optimum point.

5. SMS L-GRIN CEMENTED DOUBLET LENS

Depending on the specific application, the singlet lens discussed in the previous section may not possess sufficient degrees of freedom to produce the required performance. In such cases improved performance may be obtainable by adding a second element. The geometry, depicted in Figure 25, incorporates two L-GRIN elements which are cemented together at a spherical interface. Generalizations in which the cemented surface is an asphere are also possible, but we believe a spherical surface will simplify the fabrication process while providing sufficient degrees of freedom for most applications of interest. The parametrization scheme for this type of lens is similar to that for the previously-described singlet, except that we now have parameters defining the L-GRIN medium characteristics (i.e., the axial position of the center of symmetry and the material-ratio function) for two media rather than just one. In addition, we must specify the axial position and curvature of the spherical cemented surface.

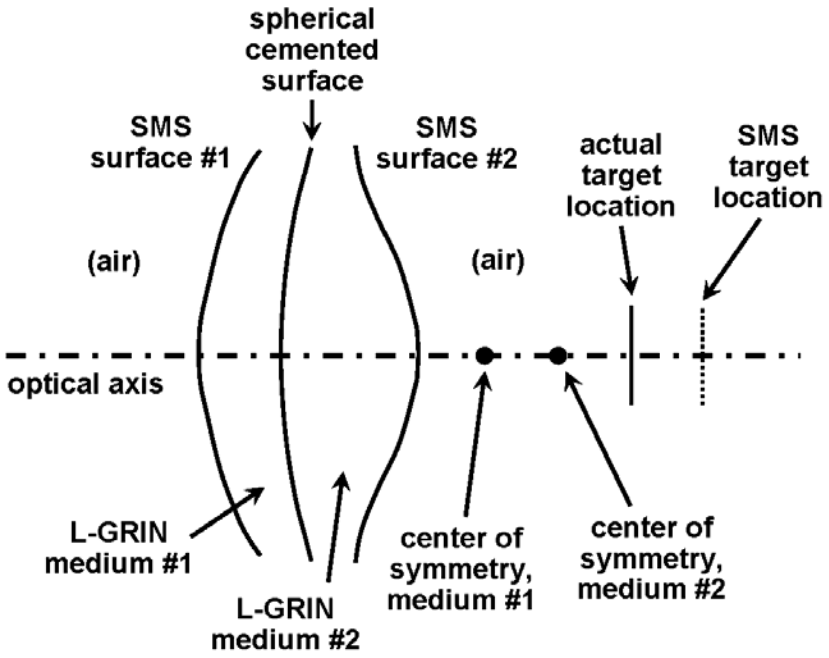

Figure 25. Notional depiction of geometry of SMS L-GRIN cemented doublet lens.

The parametrization scheme for the SMS L-GRIN cemented doublet lens will utilize the following parameters:

- The axial positions x_{sym1} and x_{sym2} of the centers of symmetry of the two L-GRIN media.
- The spline knots defining the material-ratio function for each of the two L-GRIN media. (See Figure 22.)
- The x-coordinate x_a of SMS surface #1.
- The x-coordinate of the target, x_t, used in generating the SMS lens design. (In practice it is redundant to vary both x_a and x_t, so one can be held constant during the optimization process while the other is varied.)
- The half width y_t of the target.
- The acceptance angle θ_{acc} of the SMS lens.
- The optical path length parameter Φ_0 which controls the thickness of the SMS lens.
- The wavelength λ_{SMS} for which the lens is to be designed.
- The x-axis shift Δx_t of the target location, relative to x_t.
- The axial position Δx_{cem} of the spherical cemented surface, measured relative to SMS surface #1.
- The curvature of the spherical cemented surface.
- Shape knots defining shape perturbations added to the two SMS surfaces after their shapes have been computed using the generalized 2D SMS design method.

We expect the total number of optimization parameters required to design a lens of this type will be on the order of 45. In other words, the global-optimization algorithm will be required to search a hyperspace having approximately 45 dimensions in order to find the design having optimal performance. As in the case of the SMS L-GRIN singlet lens, incorporating the generalized 2D SMS design method into the parametrization scheme should significantly reduce the number of iterations required to find the global optimum, since it will insure that all points in the design space are relatively close to the optimum point.

A special case of the SMS L-GRIN cemented doublet lens that may be of use in practice can be obtained by replacing one of the two L-GRIN media with a constant-index material. Although this reduces the number of available degrees of freedom, it also simplifies the design process as well as manufacturing and may provide the required level of performance in many applications.

6. SMS L-GRIN AIR-SPACED DOUBLET LENS

For many nonimaging applications of interest, a singlet lens or cemented doublet is not capable of bending the incident rays by a sufficiently large angle to produce optical concentration near the thermodynamic limit. This is due to the constraints imposed by Snell's law of refraction for available refractive indices. One method of overcoming this problem is to use an air-spaced doublet lens. This allows each ray to be refracted at four consecutive air-polymer interfaces, rather than just two. For almost all problems this provides a sufficiently large ray-bending capability to achieve the desired result.

The SMS L-GRIN air-spaced doublet lens is depicted in Figure 26. The parametrization scheme is identical to that for the cemented doublet of the previous section, except that two additional parameters are required: the position and curvature of the second spherical surface. As is discussed in the previous section, one or both of the spherical surfaces could be aspheric, if desired. However, we do not expect this to be necessary in most cases. In many cases it may be possible to replace one or the other of the two L-GRIN media with a constant-index material.

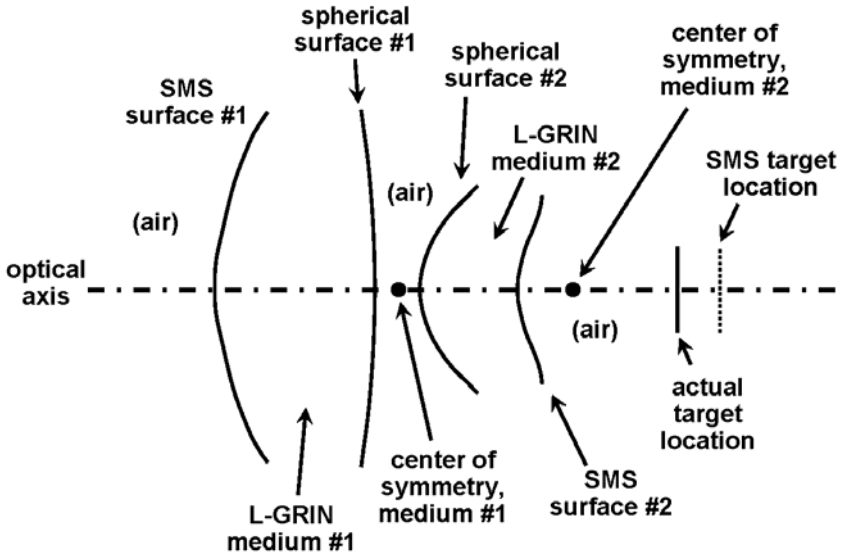

Figure 26. Notional depiction of geometry of SMS L-GRIN air-spaced doublet lens.

7. SMS L-GRIN LENS COMBINED WITH TIR EDGE-RAY CONCENTRATOR

Another configuration of interest is an SMS L-GRIN lens combined with a total-internal-reflection (TIR) edge-ray secondary concentrator, as depicted in Figure 25. The SMS L-GRIN lens is a singlet or cemented doublet, of the type discussed in Sections 4 and 5 above. The TIR edge-ray concentrator can be either axisymmetric or may have a square cross section when used with a square target. It is fabricated of a constant-index (i.e., non-GRIN) material and has a spherical entrance surface. The immersed target is optically cemented to the exit aperture of the edge-ray concentrator. The parametrization of the SMS lens is as described previously. The TIR edge-ray concentrator is designed using well-known techniques.[4] After its shape has been generated, the edge-ray concentrator is shifted along the axis and shape perturbations are added to its profile. This type of design should be capable of operation near the thermodynamic limit. The nonimaging nature of the secondary concentrator should also provide good uniformity at the target, which is often an important feature for solar concentrators.

The optimization parameters are the parameters of the SMS lens combined with the parameters defining the shape profile and position of the edge-ray concentrator. The edge-ray-concentrator-related parameters are as follows:

- Curvature c_{edge} of the refractive spherical entrance surface.
- Diameter (or width, for a square-cross-section concentrator) D_{exit} of the exit aperture.
- Axial shift Δx_{edge} of the edge-ray concentrator relative to its nominal position. When Δx_{edge} equals zero, the axial position of the entrance pupil of the edge-ray concentrator coincides with the SMS target location.
- Shape knots defining shape perturbations added to the profile of the TIR surface of the edge-ray concentrator.

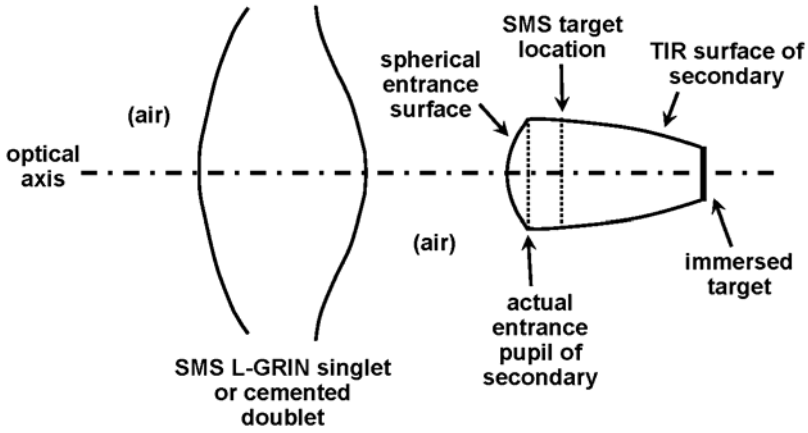

Figure 25. Notional depiction of geometry of SMS L-GRIN lens combined with TIR edge-ray concentrator.

8. REFERENCES

1. A. Brizard (2008). *An Introduction to Lagrangian Mechanics*. Singapore: World Scientific Publishing Company, pp. 14-25.
2. R. Winston, J. C. Miñano, and P. Benítez, with contributions by N. Shatz and J. Bortz (2005). *Nonimaging Optics*, New York: Elsevier Academic Press, Chapter 8.
3. P. Benítez and J. C. Miñano (1995). "Analysis of the image formation capability of RX concentrators," Proc. SPIE, v. 2538, pp. 73-84.
4. R. Winston, et al., op. cit., Chapters 4 and 5.

Case Western Reserve University Final Report

1. ABSTRACT

The objective of the Gradient Index Optics Seedling project is to design and fabricate a compact, superior imaging system utilizing spherical GRIN lens technology. The sponsored work involved optical system image characterization, design and fabrication of a GRIN lenses system. Case Western Reserve University's focus for this seedling was centered on the fabrication of nanolayered optical materials for construction of the prescribed GRIN optical lens components. Recent efforts have focused on constructing GRIN elements for two designed multicomponent imaging systems: 1) a five component optical system composed of two separate GRIN lenses, and 2) a three component optical system consisting of two GRIN lenses. In addition to the fabrication of GRIN materials for these imaging systems, focus on the future expansion of GRIN optics manufacturing were investigated in three target areas: 1) optimizing GRIN lens fabrication through use of fewer nanolayered films, 2) extending GRIN power through the design of higher Δn nanolayered systems, and 3) a bio-inspired approach toward fabrication of an aspheric GRIN lenses similar to the human eye. A brief summary of each of these projects complete with results, where obtained, is described in the following report.

2. NANOLAYERED MATERIALS FOR GRIN LENS FABRICATION

The hierarchically structured polymer GRIN lens optical materials developed in the DARPA BOSS program represent a powerful optical technique due to increased freedom in optical correction and design. The GRIN lenses are constructed to conform to a wide range of optical variables including: lens surface curvature, lens diameter/size, and in the magnitude and shape of the internal refractive index distribution based solely on slight alterations to the highly flexible lens fabrication process. To support fabrication of novel GRIN lenses, nanolayered film coextrusion was first undertaken to build a catalog of materials, each differing in refractive index, from which the NRL prescribed lens refractive index distribution designs would be constructed.

3. Forced Assembly Nanolayer Film Processing

The initial step in producing GRIN optical elements lies in making a transparent polymer film with a specified refractive index using the novel nanolayer polymer coextrusion forced-assembly technology. The process, Figure 1, uses layer-multiplication to produce large sheets of layered polymers with hundreds to thousands of layers[1-7]. Recent advances enable the facile production of nanolayer polymer films with tens of thousands of layers and layer thicknesses as small as 5 nm[3,4]. Polymer pairs were chosen so that the constituents in the alternating layers have substantial differences in the index of refraction (n). The resulting layered films possess a modulation in the index with a period corresponding to the layer thickness. When the modulation period is on the order of the quarter of the wavelength of light ($\lambda/4n$), the films are dielectric reflectors or 1D photonic crystals. This technology has been used to make a variety of polymer dielectric reflectors and filters with specific transmission properties and pass bands including a variety of commercial products[8, 9, 10]. When the layer thickness within a nanolayered

film is 50 nm or less, the index modulation is much less than the wavelength of light. The films are now transparent with a refractive index given by effective medium theory.

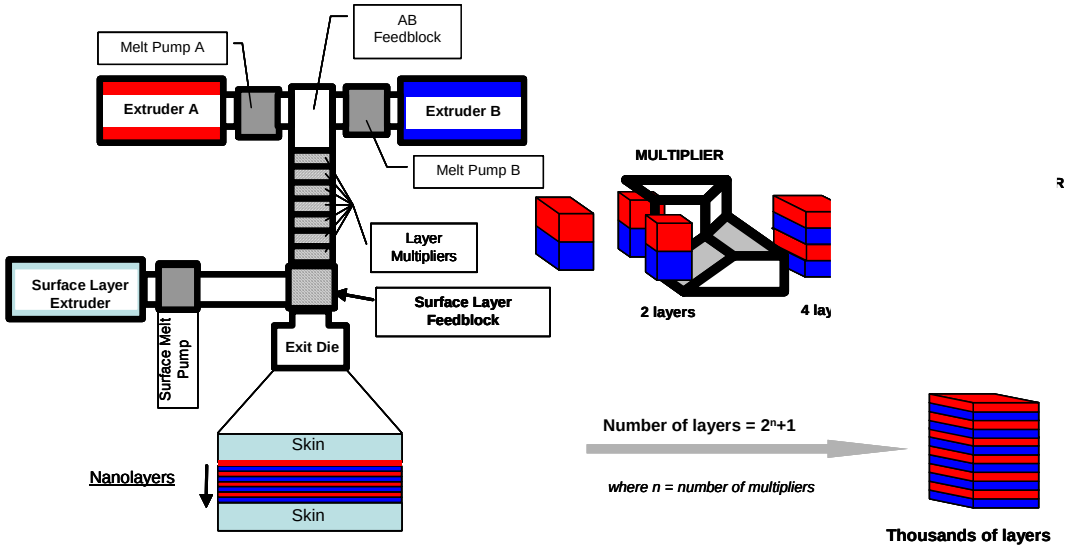

Figure 1: Two component multilayer coextrusion system with multipliers and surface layer extruder.

Utilizing the forced-assembly coextrusion process, a set of 51 films were fabricated by layering polymethyl-methacrylate (PMMA) (n=1.49) with a styrene-acrylonitrile copolymer with 17 wt % acrylonitrile (SAN17) (n=1.57). A sacrificial LDPE skin layer is added during coextrusion. This LDPE layer has been shown to improve the surface quality of the PMMA/SAN17 nanolayer films while additionally excluding contaminants during transportation and storage prior to stacking the GRIN sheet. The composition of the PMMA/SAN17 nanolayered film was varied by adjusting the relative thickness of the alternating polymer layers. The observed index varies linearly with the composition (relative layer thickness) as expected from effective medium theory, Figure 2.

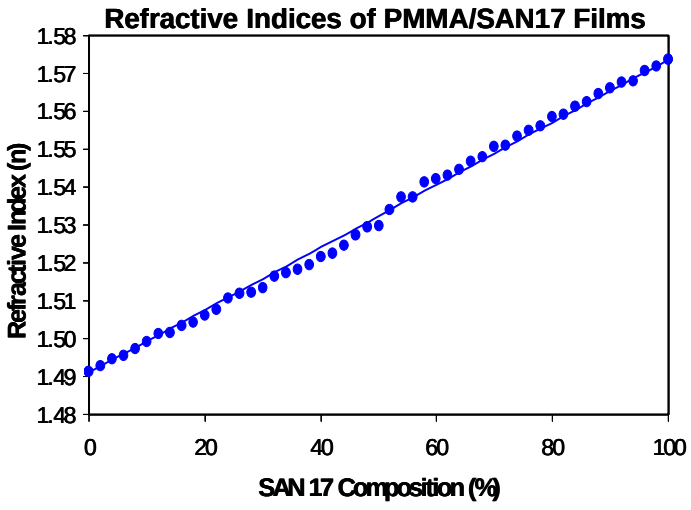

Figure 2: 51 compositions of 4,096 layer PMMA/SAN17 nanolayer film were coextruded. Individual film refractive index was varied from 1.49 to 1.57 for production of GRIN materials

The superior flexibility in designating and building different refractive index gradients into GRIN lenses lays in the production of these nanolayered optical films. Through designation of different compositions/refractive index films in a sequential film stacking recipe, the construction of prescription refractive index distributions was now undertaken based on GRIN lens designs from NRL.

4. SYSTEM I: DEVELOPMENT OF FIVE ELEMENT GRIN IMAGING SYSTEM

Based on a computer simulated optical modeling designs from NRL, a five component optical system was translated for construction, Figure 3. The five element design prescribed the fabrication of two GRIN lenses components of identical refractive index distributions. Based on the NRL design, a series of 101 individual nanolayered films were sequentially stacked to develop the specified refractive index gradient distribution. Transformation of individual nanolayered film stacks into a flat GRIN sheet was accomplished under heat and pressure in a hydraulic press.

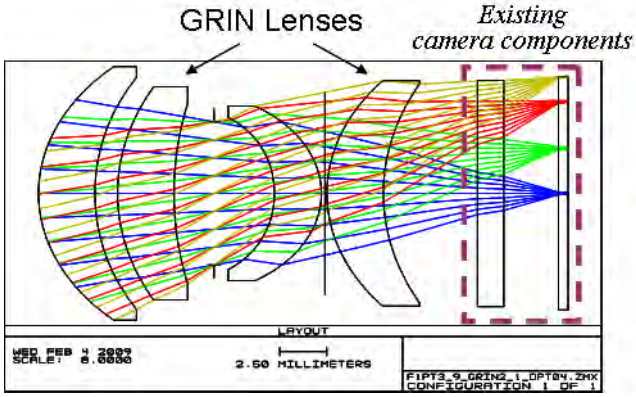

Figure 3. Five element optical design from NRL. System requires fabrication of two GRIN lenses.

Upon successful sheet formation, the refractive index distribution was determined by ATR-FTIR microspectroscopy using the characteristic peaks for SAN17 at 698 cm^{-1} and 1727 cm^{-1} for PMMA. The refractive index was calculated from the composition since this was a layered effective medium. A comparison of measured and prescribed refractive index showed excellent correlation in the GRIN stacks, Figure 4.

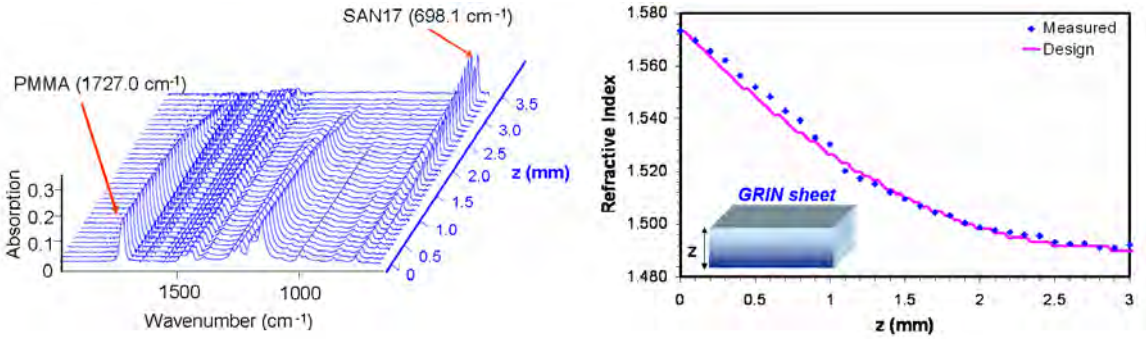

Figure 4: (Left) Measured ATR-FTIR spectrum of nanolayered GRIN sheet. (Right) Comparison of measured and design GRIN sheet refractive index based from ATR-FTIR scans.

Flat GRIN sheet light transmission was measured as a function of half angle to ensure high optical clarity of the stacked material, Figure 5. Light transmission through the GRIN sheet displayed transmission values similar to optical grade monolithic plastic stacks demonstrating an acceptable quality for further lens fabrication.

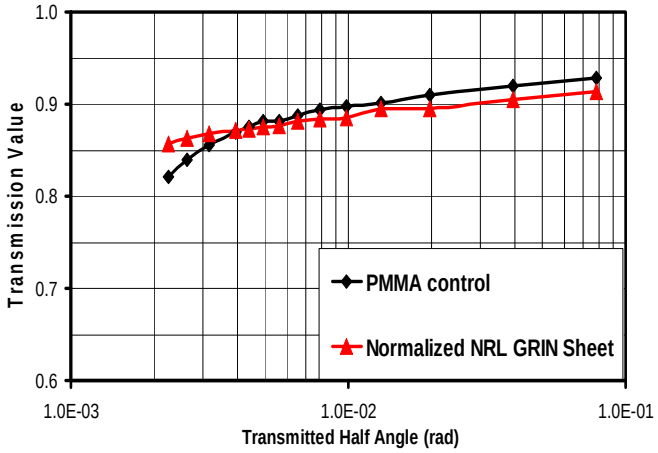

Figure 5: Flat GRIN sheet transmission performance.

Spherical meniscus shaped GRIN lenses were formed from the flat sheet via a second heated compression step. A piece of flat GRIN sheet was placed between a convex spherical mold with specified radius, R_1= , and a concave spherical mold, R_2= . The final lens thickness was equal to the difference $\Delta R = R_2 - R_1$, which is required to maintain a radially symmetric refractive index profile in the final spherical lens. After shaping, the convex GRIN lens surface curvature was confirmed via optical topography scans using a placido cone topographer. Two GRIN lenses of the prescribed GRIN distribution and shape were translated to NRL for further optical characterization and diamond turning to final lens geometry.

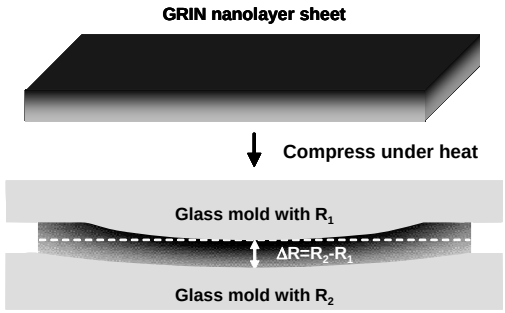

Figure 6: Shaping a flat GRIN sheet into aconcave-convex GRIN lens.

5. SYSTEM II: DEVELOPMENT OF THREE ELEMENT GRIN IMAGING SYSTEM

A second, three element optical system was designed by NRL to highlight the optical effectiveness of GRIN systems, Figure 7. This three component system combines one traditional spherical GRIN lens with a second axial GRIN lens, a nanolayered GRIN optic with a refractive index distribution decoupled from the lens surface curvature.

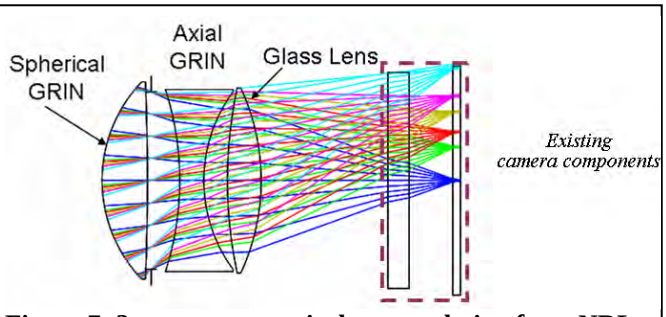

Figure 7: 3 component optical system design from NRL with two GRIN lenses.

Fabrication of a 25 mm diameter spherical GRIN lens with a Δn=0.07, following the NRL prescribed refractive index distribution, was undertaken by initially stacking a series of 109 individual nanolayered films in a clean room facility to develop the specified refractive index gradient distribution. Transformation of

individual nanolayered film stacks into a flat GRIN sheet was accomplished under heat and pressure in a hydraulic press. To ensure high optical quality of the GRIN sheet, light transmission measurements as a function of transmitted half angle were measured, Figure 8.

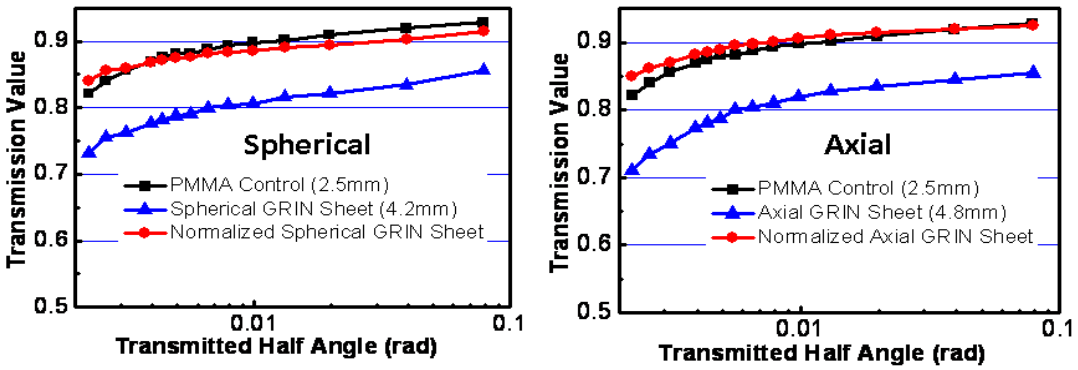

Figure 8: Flat GRIN sheet optical transmission values for (left) spherical design GRIN sheet and (right) axial design GRIN sheet

Spherical meniscus shaped GRIN lens preforms were formed from the flat GRIN sheet via a second heated compression step. A circular, 25 mm diameter, piece of flat GRIN sheet was placed between a convex spherical mold with specified radius, R_1= 20.2 mm, and a concave spherical mold, R_2= 17.0 mm. The final lens thickness was equal to the difference $\Delta R = R_2 - R_1$=3.2 mm, which is required to maintain a radially symmetric refractive index profile in the final spherical lens. After shaping, the convex GRIN lens surface curvature was confirmed to match the design specification via topography scans using a placido cone topographer, Figure. 9.

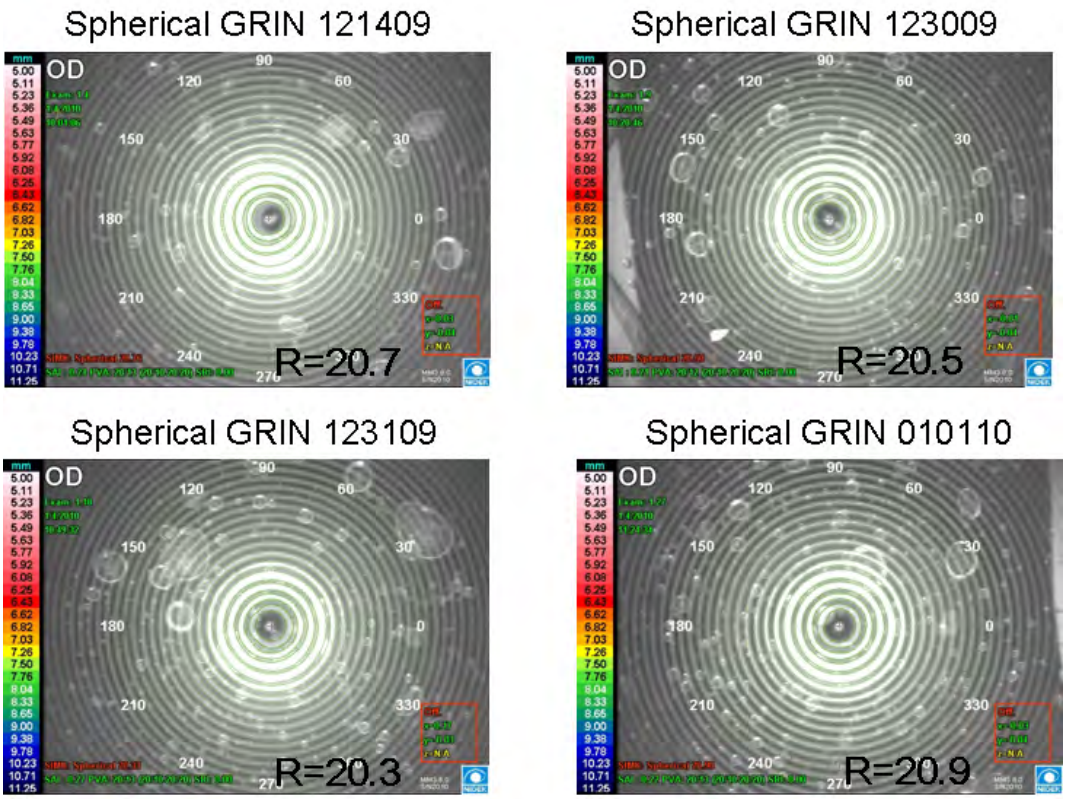

Figure 9: Placido-cone topography scans of four spherical GRIN performs exhibiting good agreement against prescribed R=20.2 mm surface curvature.

The refractive index distribution through the lens thickness was determined through a sacrificial ATR-FTIR microspectroscopy characterization technique. The refractive index of the GRIN perform as a function of position through the lens thickness was polishing the perform to a plano-convex shape and subsequently measuring the ATR-FTIR spectrum of the lens at 50 micron intervals. The series of ATR-FTIR scans as a function of position was utilized to determine PMMA/SAN17 composition as a function of position using the relative heights of characteristic peaks for SAN17 at 698 cm^{-1} and 1727 cm^{-1} for PMMA. The refractive index was then calculated from these measured compositions using the layered effective medium prediction for an additive refractive index. A comparison of measured and prescribed refractive index showed good correlation in the spherical GRIN preform, Figure 10. Four spherical GRIN lens preforms of the prescribed GRIN distribution and shape were translated to NRL for further optical characterization and diamond turning to final lens geometry.

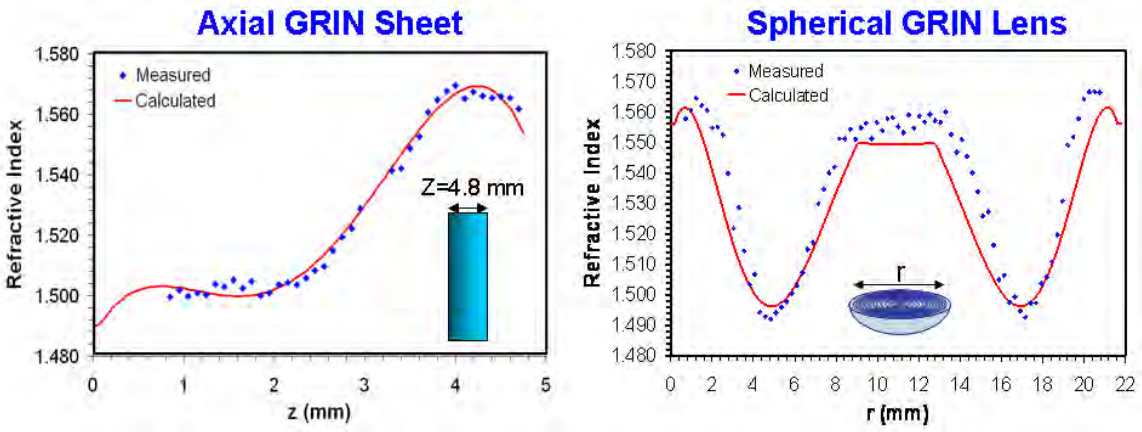

Figure 10: Comparison of NRL supplied GRIN distribution design and FTIR measured as-built refractive index distribution.

The production of a flat GRIN sheet for fabrication of a 25 mm diameter axial GRIN lens with a Δn=0.08, following the NRL prescribed refractive index distribution, was undertaken by initially stacking a series of 192 individual nanolayered films within a clean room facility to develop the specified refractive index gradient distribution. Transformation of individual nanolayered film stacks into a flat GRIN sheet was accomplished under heat and pressure in a hydraulic press. Following the previous characterization protocol, light transmission measurements as a function of transmitted half angle were measured for the axial GRIN sheet, Figure 8. Axial GRIN distributions do not require subsequent shaping steps, molding into spherical preforms transforms the GRIN distribution from axial to radial, prior to the final diamond turning step. Therefore, the refractive index distribution through the flat GRIN sheet was measured by the ATR-FTIR characterization technique to ensure the refractive index distribution corresponded to the design specifications. Utilizing a procedure similar to that undertaken for the spherical GRIN lens, a sacrificial axial GRIN sheet was halved and the refractive index profile was determined as a function of sheet thickness. A comparison of measured and prescribed refractive index showed good correlation in the axial GRIN sheet Figure 10. Four axial GRIN sheets of the prescribed GRIN distribution and thickness were translated to NRL for further optical characterization and diamond turning to final lens geometry. Final assembly of the diamond turned GRIN optics with a final commercial monolithic lens for seedling demonstration devices was completed at NRL

6. FUTURE FOCUS: OPTIMIZATION & EXPANSION OF GRIN CAPABILITIES

A continued effort to expand on existing nanolayered GRIN technology boundaries will be imperative for translation of this enabling optical technology into industrial and a wider array of technical applications. Three focus areas were identified in efforts to expand the current nanolayered GRIN lens fabrication: 1). optimization of GRIN fabrication, 2). nanolayer film processing of higher Δn materials, and 3). fabrication of aspheric GRIN lenses.

Translation of nanolayered GRIN technology to commercial applications will require ultimate scale-up of the lens fabrication process. Minimization of labor intensive fabrication methods is a

current focus in anticipation of potential scale-up endeavors. The stacking of individual nanolayered polymer films to achieve the desired refractive index distribution can easily be identified as the most labor intensive step in the lens fabrication process. In an effort to streamline the stacking procedure, an investigation into the effect of stacking fewer nanolayered film compositions (refractive index points) to match a prescribed lens distribution is underway.

A 4x reduction in the number of nanolayer films stacked in a GRIN lens is being attempted to investigate performance effects of streamlining the lens fabrication process. Utilizing a previously published GRIN lens design, the effect of reducing the number of optical stacked films from 104 to 26 is being attempted, Figure 11.

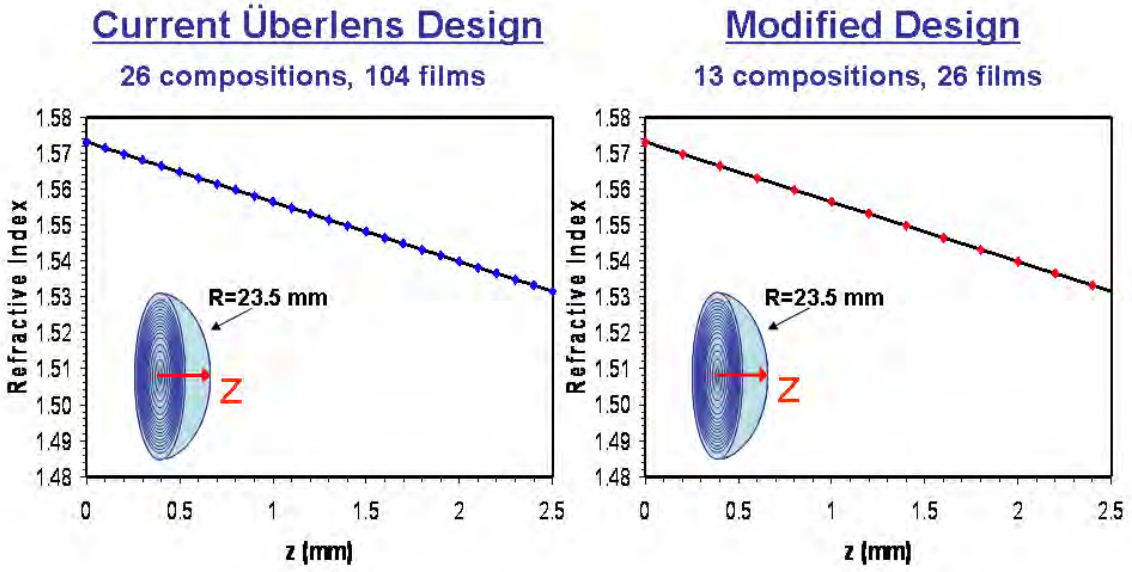

Figure 11: (Left) Current Überlens design utilizing 104 nanolayered films and 26 compositions. (Right) Modified design utilizing fewer 6 mil films and only 13 compositions.

After stacking, a flat GRIN sheet will be fabricated and characterized for GRIN distribution and optical transmission. Subsequent lens shaping will produce a spherical GRIN element with reduced number of nanolayered films that can be imaged with performance quantitatively compared to the conventional fabricated optic performance.

Current forced assembly lens technology utilizes PMMA/SAN17 ($\Delta n=0.08$) nanolayered films to construct GRIN lenses. Identification of additional layered polymeric materials with higher ($n > 1.58$) and/or lower ($n < 1.49$) refractive indices provides an opportunity to create more powerful lenses. Driven by optical simulations from NRL prescribing desired refractive indices for GRIN lenses, the identification of potential coextrudable polymers was investigated to create a new family of GRIN optics. A low refractive index polymer is polyvinylidiene fluoride (PVDF), n=1.39. PVDF is a semi-crystalline polymer, however, it is known to form a miscible blend with PMMA thereby eliminating crystallinity and increasing material transparency. A 50/50 PVDF+PMMA blend/PMMA nanolayered system was coextruded and successfully developed a bank of optical films with a lower refractive index range from 1.44 to 1.49, Figure 12. Successful

inclusion of these nanolayered films with the existing PMMA/SAN17 (n=1.49 to 1.57) system will allow for a 50% increase the available GRIN optics to Δn =0.13.

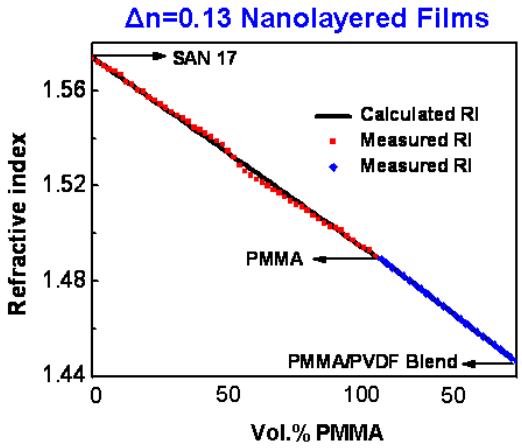

Figure 12: Higher Δn=0.13 range proposed with inclusion of PVDF into nanolayered films.

Aspheric GRIN elements could allow for even greater degrees of freedom in the design of optical systems. Aspheric GRIN lenses are prevalent in nature, including the human eye lens. A bio-inspired aspheric GRIN lens design based on the published human eye aspheric geometries and refractive index distribution[14-16] (Δn=0.04) is under joint development at CWRU and Rose Hulman University, Figure 13.

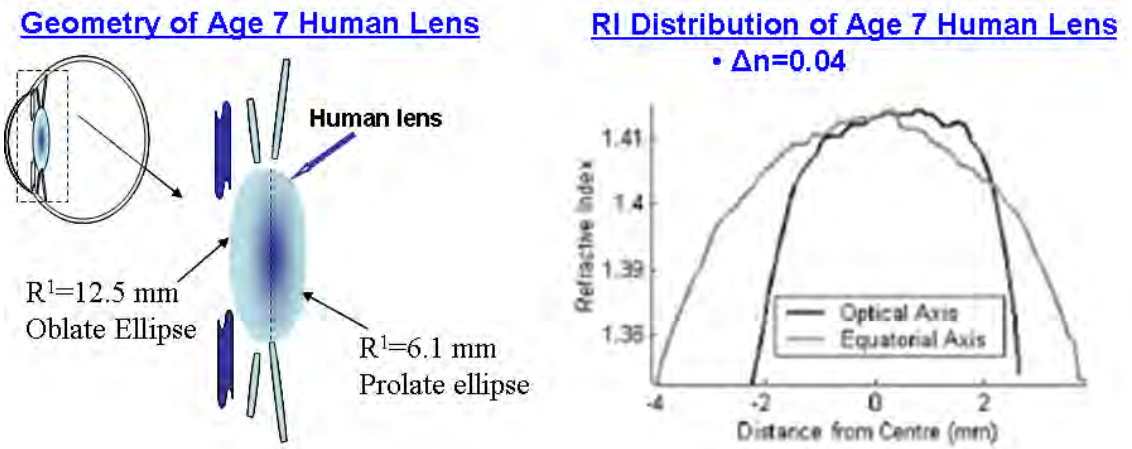

Figure 13: Human eye (left) aspheric geometry and (right) refractive index distribution from which the bio-inspired aspheric GRIN lens is being designed.

Successful fabrication of an aspheric GRIN optic could allow for even greater simultaneous aberrations (i.e. third order and higher as well as chromatic) control in a single optical element to even further reduce the required number of elements, and subsequent device size, in many optical systems. A preliminary design for an aspheric human eye lens was completed in December and proof-of-concept fabrication trials to produce the GRIN lenses are currently underway.

7. ACCOMPLISHMENTS SUMMARY

The successful fabrication of two GRIN lenses for a five element optical design and a spherical and axial GRIN lenses for a second more compact three component camera demo system was completed. Additionally, focuses on expanding GRIN optics manufacturing were initiated to investigate three target areas: 1) optimizing GRIN lens fabrication through use of fewer nanolayered films, 2) extending GRIN power through the design of higher Δn nanolayered systems, and 3) a bio-inspired approach toward fabrication of an aspheric GRIN lenses similar to the human eye. Successful coextrusion trials of a PMMA and PVDF blend/PMMA nanolayered film system have enabled an evolutionary expansion of available materials down to a refractive index of 1.44. Preliminary lens fabrication experiments are underway in the area of optimized GRIN manufacturing and creating bio-inspired aspheric GRIN lenses with the first expected results by mid-2010 pending Phase II activity.

8. REFERENCES

1. M. Ma, K. Vijayan, A. Hiltner and E. Baer, "Thickness Effects in Microlayer Composites of Polycarbonate and Poly(styrene-acrylonitrile)," *J. Mater. Sci*., 25, 2039-2046 (1990);
2. C.D. Mueller, S. Nazarenko, T. Ebeling, T.L. Schuman, A. Hiltner and E. Baer, "Novel Structures by Microlayer Coextrusion – Talc-filled PP, PC/SAN, and HDPE/LLDPE," *Polym. Eng. Sci*., 37, 355-362 (1997);
3. P. Orench, F. Ania, A. Hiltner, T. Bernal, B.J. Balta-Calleja, and E. Baer, "Basic Aspects of Microindentation in Multi-Layered Poly(ethylene terephthalate)/Polycarbonate Films," *Phil. Mag*., 84, 1841 (2004);
4. R. Tangirala, C. Weder, A. Hiltner, and E. Baer, "Design and Application of Photopatternable Nanomaterials," *Adv. Funct. Mater*. 14, 595 (2004);
5. R.Y.F. Liu, T.E. Bernal-Lara, A. Hiltner and E. Baer, "Polymer Interphase Materials by Forced Assembly," *Macromolecules* 38, 4819-4827 (2005);
6. J. Kerns, A. Hsieh, A. Hiltner, and E. Baer. "Comparison of irreversible deformation and yielding in microlayers of polycarbonate with poly(methylmethacrylate) and poly(styrene-co-acrylonitrile)," *J. Appl. Polym. Sci.* 77, 1545-1557 (2000).
7. C. Mueller, V. Topolkaraev, D.Soerens, A. Hiltner, and E. Baer. "Breathable polymer films produced by the microlayer coextrusion process," *J. Appl. Polym. Sci.* 78, 816-828 (2000).
8. Schrenk, W.J., Wheatley, J.A., Lewis, R.A., and Arends, C.B., *Nanolayer Polymeric Optical Films*. Tappi Journal, 1992, 75(6): pp. 169- 174.
9. Weber, M.F., Stover, C.A., Gilbert, L.R., Nevitt, T.J., and Ouderkirk, A.J., *Giant Birefringent Optics in Multilayer Polymer Mirrors.* Science, 2000, 287(5462):pp 2451-2456.
10. W.J. Shrenk, *Method of Making Christmas Tinsel*, US Patent #3,480,502; November 25, 1969.
11. Y. Jin, H. Tai, A. Hiltner, J.S. Shirk, and E. Baer, "A New Class of Bioinspired Lenses with Gradient Refractive Index," *J. Appl. Polym, Sci.* 104, 1834 (2007).
12. G. Beadie, M. Ponting, A. Rosenburg, T. Kazmierczak, P. Lane, Y. Yang, E. Fleet, J. Shirk, A. Hiltner, and E. Baer. "Tunable Polymer Lens," *Optics Express*. 16, 11847- 11857 (2008).

13. G. Beadie, M.L. Sandrock, M. Wiggins, R.S. Lepkowicz, A. Kamdar, M. Ponting, T. Kazmiercazk, Y. Yang, J. Shirk, A. Hiltner, and E. Baer. "Optical Properties of a Bio-Inspired Gradient Refractive Index Polymer Lens," *Optics Express*, 16, 11540- 11547 (2008).
14. Dubbelmann, M. and Van der Heijde, G.L. *Vision Research* **41** 2001
15. F. Manns et al. *Exp. Eye Research*. **78**, 39-51, 2004.
16. Jones et. al. *Vision Research* 45 2005

U.S. Naval Research Laboratory Final Report

1. Summary

This is a report on NRL's contribution to the DARPA GRIN seedling program. NRL and Case Western Reserve University were tasked to design and fabricate a prototype lens that, through the use of our GRIN optics, would exhibit real advantages over an existing, state-of-the-art optical design. The result is a design that exhibits better or equal resolution over most of the field of view of our camera at less than $1/7^{th}$ the weight, ¼ the volume, and only 60% of the lens count.

For this demonstration, we chose to develop a lens based on a SWIR, helmet-mounted monocular design funded by Night Vision Labs, and used by hundreds of soldiers today. Manufactured by StingRay Optics, this lens represents the culmination of hundreds of years of conventional optical design, hundreds of years of mechanical engineering development, and decades of perfecting the glass materials on which the optics depend. It is an excellent design, and one that StingRay can be proud of.

In contrast, our polymer optics weren't even conceived of ten years ago. Only a few, custom optical design tools existed that could optimize a design; more had to be developed during the course of this seedling just to do the work. Material fabrication hasn't yet moved beyond the original laboratory of its invention, and accurate dispersion curves were available only after we measured them as part of this program. Relevant metrology had yet to catch up with the types of fabrication variations important to the designs, and optical tolerancing was nonexistent.

The fact that we succeeded in our goals on such a short time frame, with so little existing infrastructure, is a testament to the promise of the GRIN technology. Despite the nascent state of sophistication, we were able to develop a design and execute all the stages of prototype fabrication to deliver a f/1.5, 18.5 mm focal length SWIR lens with a 35° field of view for a C-mount camera with 25 um pixel resolution – all with a 7.7 g mass. By contrast, the StingRay optics has a mass of 57.7 g: 7.5 times heavier.

2. Optical Design

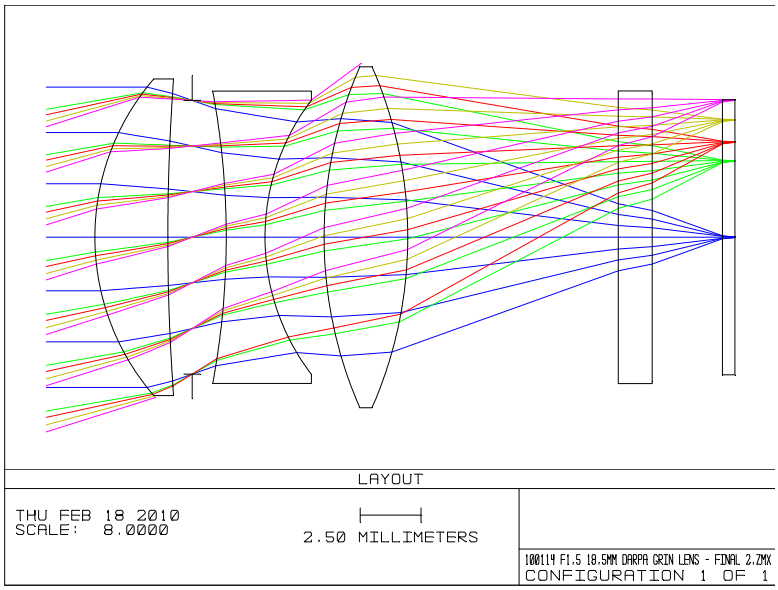

Figure 1: Final lens design for SWIR prototype lens. The first two elements are plastic GRIN lenses. The third element is a biconvex, N-SF10 glass singlet. The flat elements are parts internal to the SWIR camera. The green, red, and gold rays correspond to the vertical, horizontal, and diagonal extents of our InGaAs camera. The pink rays correspond to the field of view specified in the seedling statement of work.

Our final design is presented in Figure. 1. The primary difference between this design and the preliminary design mentioned in our Nov. 2009 three-month progress report is the nature of the third, glass lens. The earlier version had a smaller glass lens with different radii of curvature on the front and back faces. When that design was communicated to the mechanical engineers, however, the feedback we received was that the edge thickness of the glass lens was too thin. Thus, we were forced to widen the center thickness of the lens to allow for a thicker edge. As we altered the design to accommodate this change, we found that the front and back radii were close to one another in value. We decided to go ahead and make the radii the same to facilitate fabrication of the lens.

These changes did not come without some impact on the front two elements. To accommodate changes in the back lens, we were required to re-optimize the surfaces of the front two lenses. The gradient index distributions remained unchanged – only the design surfaces and lens spacings were altered. The biggest qualitative change is that the back surface of lens one changed from slightly convex to slightly concave. This had the added benefit of allowing the edge thickness of this lens to be thicker than the previous design, as well.

Figure 2 depicts the spot size performance of the lens, for the same field angles depicted in the ray trace of Fig. 1. As can be seen from the spot size distributions, the ideal (digital sensor) spot size of two-by-two pixels is maintained over nearly all the camera's imaging area. To the best of

our knowledge, this performance for a 35° FOV, 18 mm lens at f/1.5 is unmatched for a three-element conventional lens system.

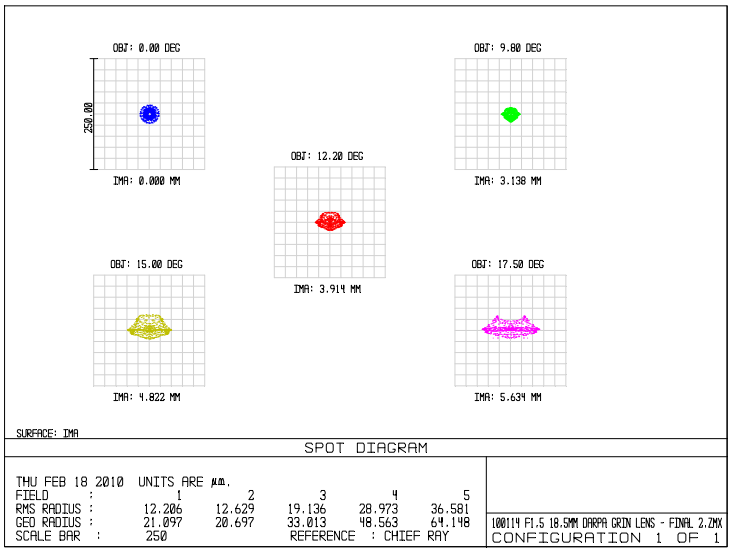

Figure 2: Calculated spot patterns of rays at the camera plane, plotted on a scale at which each gray box represents a pixel of the camera sensor. As in Fig. 1, green, red, and gold patterns correspond to the vertical, horizontal, and diagonal limits of our InGaAs camera. The pink pattern corresponds to the maximum field angle specified in the seedling statement of work.

The spot size distributions of Figure 2 provide the easiest way to see how the lens system focuses light, but are not what will be measured in the laboratory. That's because a careful measurement of the true spot size distribution would require an imaginary sensor capable of much higher spatial resolution. Instead, what is measured in the lab are modulation transfer functions (MTFs). These functions represent the Fourier transforms of the spot patterns. An infinitesimal point spot would be represented by a unit-valued MTF. A Gaussian spot would have a Gaussian MTF peaked at zero frequency and a half-width inversely proportional to the spatial resolution of the imaged spot. For a pixellated camera with a pixel pitch of Δx, a common goal is to achieve an MTF curve >0.5 at a spatial frequency of $1/(2\ \Delta x)$. For our camera, this corresponds to a spatial frequency of 20 mm^{-1}.

The MTF curves calculated for the lens are presented in Fig. 3a. Because the spot sizes in Figure 2 are not symmetric, the MTF curves are different if calculated along one axis versus another. For example, the pink spot distribution in Figure 2 is quite narrow along the vertical direction. Horizontal (tangential) edges would remain sharply focused, because it would be easy to distinguish top from bottom. Vertical (sagittal) edges, however, would be smeared out by the horizontal spot spread. This information shows up in the MTF curves. There are two pink MTF curves, one labeled T (tangential) and the other S (sagittal). As advertised, the T curve is quite good. It remains well above a value of 0.5 at the design goal of 20 mm^{-1}, while the S curve dips below 0.5 near a modest spatial frequency of 5 mm^{-1}.

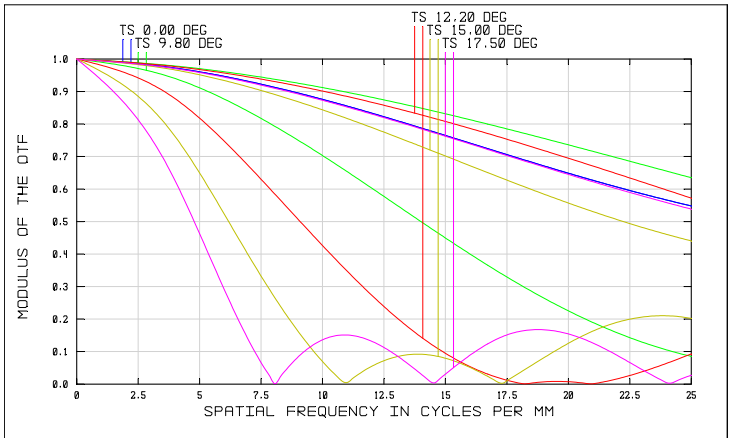

Figure 3a: Calculated modulation transfer functions (MTF curves) for the SWIR prototype.

Despite the good performance exhibited by our design, a careful comparison with the curves reported in Nov. 2009, Fig. 3b, shows that we have increased the asymmetry in the spot size distribution at the edges of the field. The sagittal MTF curves for higher field angles are lower now than they were in the Nov. design, while the transverse curves are higher.

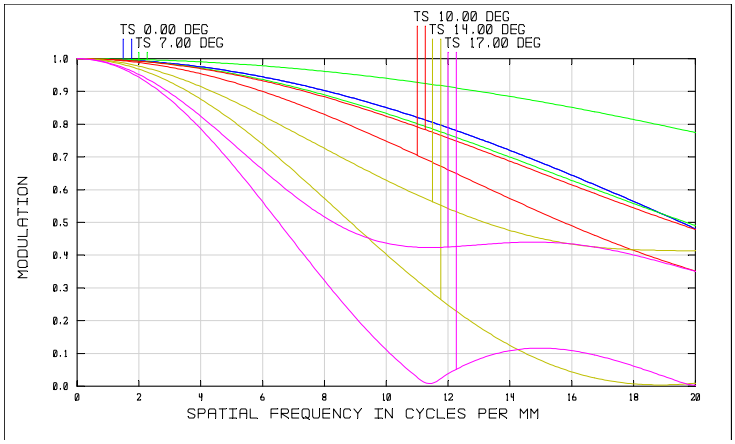

Figure 3b: Predicted MTF curves for Nov. 2009 design.

The increased asymmetry is tentatively attributed to the effect of being forced to make the back lens thicker, without the ability to balance that by altering the GRIN distributions of the front two lenses. At the stage where we received feedback from the mechanical engineers, the GRIN stacks were already fabricated.

Addendum: It should be pointed out here that great effort was expended to develop a new design in very short order. The initial lens preforms received from Case Western for element 1 were too thick. To mitigate risk to the overall project we at NRL came up with a new design which would have incorporated the thick preforms. This design differed in many respects from the one we implemented, requiring a different back lens and different curvatures on the middle one. Ultimately the design was unnecessary, because the team members at Case successfully delivered preforms which met the original thickness specs.

3. Preform Screening & Analysis

The prototype optical design called for two different GRIN lenses to be fabricated. The front lens, lens 1, had a spherical GRIN distribution. Before being diamond turned, flat GRIN stacks to be used for lens 1 were molded between two concentric surfaces as depicted in Fig. 4. Copies of lens 2, on the other hand, were diamond turned directly from flat GRIN stacks, without such a molding step. The GRIN distributions remained the same as reported in the first quarterly report, reproduced here in Fig. 5.

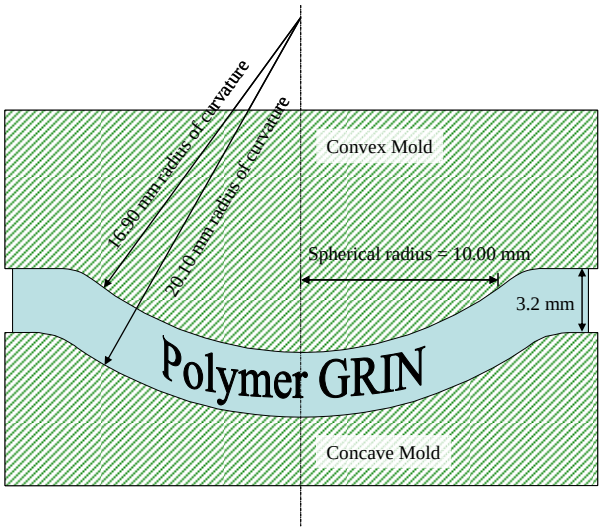

Figure 4: Geometry of spherically-molded GRIN preforms.

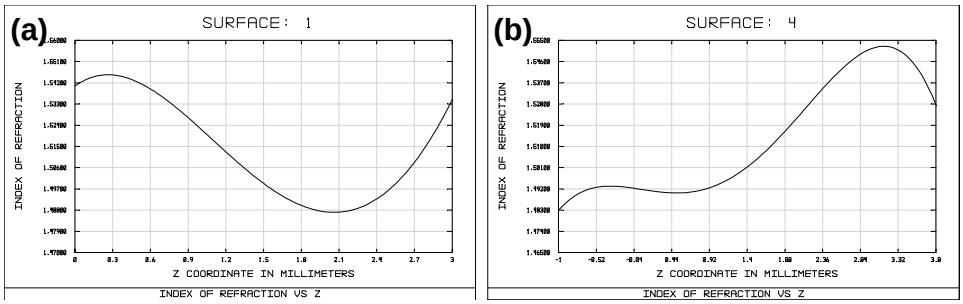

Figure 5: Gradient index distributions along the optical axis for (a) the front lens and (b) the middle lens. The x-axis origins for each plot are the left-hand side vertices, and the wavelength for which the index values are computed is 1.5 um.

Before preforms were sent to Nu-Tek for diamond turning, we at NRL screened their optical & physical properties. In addition to a careful visual inspection, we measured thicknesses, imaged a set of straight lines through each preform, and measured the wavefront of a clean HeNe laser beam transmitted through the samples.

The thickness measurement was the most straightforward, but also the most important. The first set of spherically-molded preforms received from Case Western were too thick. Instead of the design goal of 3.20 mm, we received three lenses with an average center thickness of 3.54 ± 0.02 mm. Had we been required to use them, we would have been forced to redesign the lens.

Indeed, as a risk-mitigation measure we executed a re-design to accommodate just such an eventuality.

As a sign of their commitment to the program, however, the team at Case Western was able to rapidly produce three more molded preforms that met the thickness criteria, nearly doubling the number of such elements they expected to deliver, all during late December when most people were celebrating the holidays. The four spherically-molded preforms eventually delivered to Nu-Tek for diamond turning had center thicknesses with a mean of 3.22 mm and a root-mean-squared deviation of 0.03 mm. Modeled in Zemax, the thickness variation of these lenses failed to alter spot size distributions by more than a few percent.

The thicknesses of the flat, axial GRIN sheet averaged 4.87 mm with a RMS deviation of 0.03 mm. The target thickness was 4.75 mm. In the case of the axial GRIN, however, the thickness tolerance was not as stringent. That is because much of the center thickness is polished away in the process of fabricating a negative-power lens with a final center thickness of just 1.6 mm. A slight, 50 micron adjustment to the depth cut into the GRIN sheet was all that was necessary to accommodate the extra stack thickness. With this adjustment, Zemax once again predicted no real change to the lens optical properties.

In addition to thickness measurements, we also screened the samples for optical quality. Due to the aggressive nature of our schedule, there was not time to do more than a few measurements of each sample. In Fig. 6 is a depiction of one of our simpler screening methods – capturing an image of a series of straight lines as viewed through our samples.

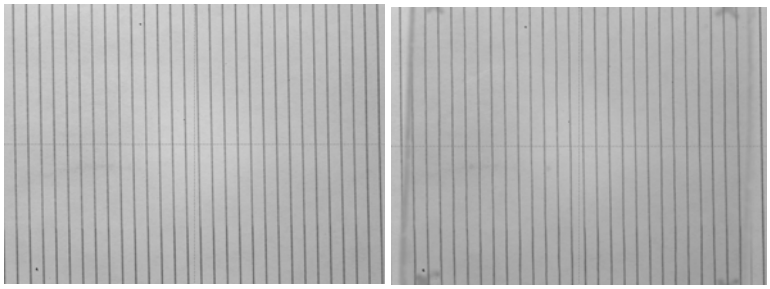

Figure 6: Picture of lines on a page (L) as viewed through axial GRIN preform 100104 (R).

While these images provide only a qualitative picture of sample quality, they serve two purposes. The most important is they provide a simple screening technique that can be communicated to Case Western. By tying later (quantitative) measurements back to these images, we provide Case Western with a simple method of looking at their sheets with an educated eye, to gauge sample quality as they go. The second purpose is to serve as a frame of reference for later, wavefront measurements, to see whether defect patterns in the more-abstract measurements can be tied to features seen naturally in visible images.

The more sophisticated of our measurements recorded the optical wavefronts transmitted through the samples, via a Shack-Hartmann-based instrument. These measurements require a bit of explanation in order to put the data into proper context. First, for the sake of completeness, one must understand the nature of an optical wavefront. This is an imaginary surface on which a

snapshot of a propagating optical wave has the same phase. It is important because the propagation of a wave after "unfreezing" the picture proceeds everywhere perpendicularly to the wavefront. An unchanging, collimated beam possesses a planar wavefront, while a perfectly focusing wave has a spherical wavefront.

A wavefront that is nearly spherical, but has some irregularity to it, won't focus properly. Instead, the focal spot will be blurred – the more irregularity to the spherical wavefront, the more blurred the spot. That explains the importance of the wavefront in imaging lenses: a lens is supposed to produce spherical wavefronts which focus down precisely onto the image plane.

The next issue to consider is the magnitude of wavefront distortions that are significant. This value is application specific. In the case of the GRIN prototype, it was determined by modeling a random phasefront modulation at the aperture stop that a 2-wave RMS distortion had only a minor impact on image quality, while a 20-wave RMS distortion severely degraded the lens performance.

If a material is truly homogeneous, then the only sources of wavefront deviation occur at the interfaces between it and some other material. A small surface ripple on an otherwise flat & parallel window will result in small ripples on the wavefront. Similarly, however, material inhomogeneities can cause wavefront distortions. Even with perfect plane parallel faces, a window can exhibit ripples in transmitted wavefronts if there are similar ripples in the material composition.

In our case, we can expect potential contributions from both types of sources – surface inhomogeneities as well as compositional ones. In an attempt to isolate the two effects, we measured transmitted wavefronts for each optic under two conditions: in one case the optic was in air, while in the other the wavefront was measured through the optic while it was submerged in water. By immersing the preforms in water we reduce the effect of surface inhomogeneities, just as a glass becomes nearly invisible when placed inside a fish tank. Bulk inhomogeneities, however, remain unchanged.

Finally, there is the issue of what is measured and how it is reported. An important aspect of the measurement is that the wavefront is ***not*** measured directly. Instead, an input wave is sampled on a grid of points and the local direction of propagation is measured at each one. This results in a set of tilt, or slope measurements – measures of the local wavefront normal vector at each point. A particular dataset is plotted in Fig. 7.

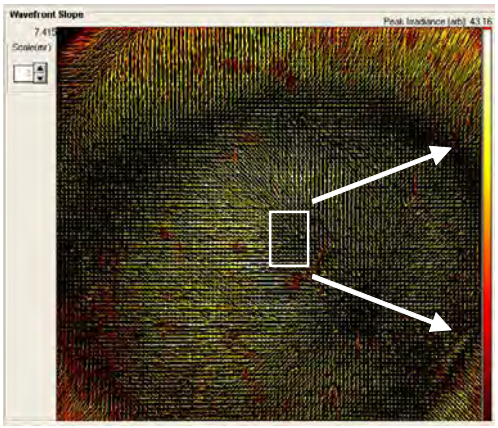

Figure 7: (L) Example plot of the raw data measured by a Shack-Hartmann instrument. Each line in these plots represents local tilt of the wavefront – direction of tilt indicated by line direction and steepness by line length. Color coding represents detected light intensity. The full field of view is 14.8 x 14.8 mm, which is sampled on grid points separated by 0.14 mm. (R) A magnified section of the overall plot.

Though it may seem that this is an acceptable way to measure a wavefront, in fact it leaves the true wavefront open for interpretation. That is because the measurement of wavefront slope does not provide the wavefront value, any more than measuring the grade of a hill tells you how high above sea level it is. This problem is illustrated in Fig. 8.

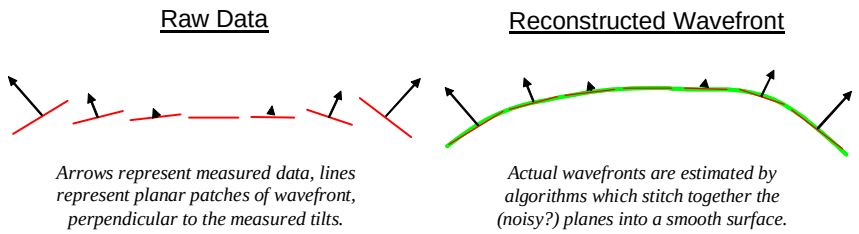

Figure 8: Understanding Shack-Hartmann data. (L) A Shack-Hartmann instrument samples light exiting a test optic at discrete points, measuring at each point the local tilt to the wavefront Since light propagates perpendicularly to the local wavefront, a measurement of the wavefront is a direct measurement of the light propagation property. (R) Measuring the local wavefront direction does not immediately provide the wavefront, however. The overall wavefront needs to be mathematically synthesized from the raw, tilt data.

To get a full picture of the measured data, therefore, it is necessary to provide not just a reconstructed wavefront but also a plot of the original, raw data file, to allow one to see whether any features evident in the raw data are glossed-over in the reconstruction process. Furthermore, another plot is useful in our case. The wavefront depicted in our software is presented as a colored contour map. However, because the color scheme is rescaled for every calculation, it is difficult to determine the severity of the wavefront distortion by eye. To alleviate this problem, a third plot is recorded along with the raw tilt and reconstructed wavefront plots – a calculated fringe pattern. This is the pattern one might see if the wavefront were viewed in an interferometer. Since each fringe represents a half-wave deviation, it is quickly evident when the wavefront exceeds several waves deviation. The contour map is still necessary, however, in order to provide the proper perspective on which fringes are peaks and which represent valleys.

4. Wavefront results: Axial GRIN

The axial GRIN preforms provide the simplest wavefront samples to analyze. That's because an axial GRIN with plane parallel surfaces, when illuminated with collimated light, should transmit flat wavefronts. Shown in Figs. 9-10 are the data collected upon viewing through axial preform #100104, through both air & water. An important point to note is that the overall fringe patterns for each case have almost identical fringes. In other words, the principle phase distortion acquired through the optic is internal. On the other hand, the magnitude of this distortion is very small – less than 0.5 waves RMS over a 14.8 mm diameter exceeding the clear aperture of the finished optic (12.0 mm).

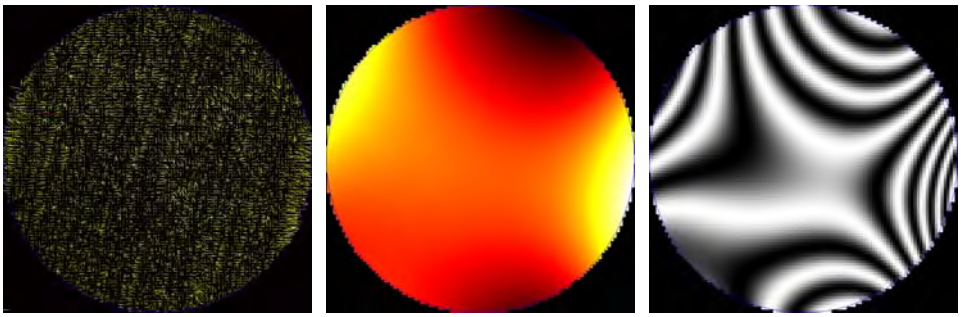

Figure 9: Shack-Hartmann measurements for axial GRIN preform 100104 in air. (L) Raw tilt data, (M) Contour map of reconstructed wavefront, and (R) Contour map presented as interferogram at 632.8 nm. The data diameter is 14.8 mm. The peak-to-valley optical path difference is 3.6 waves. RMS deviation is 0.37 waves.

Though there is little difference in the reconstructed wavefronts, there is a difference visible in the raw data. Figure 9 shows clearly-visible wavefront ripples in the air data which extend almost vertically across the field of view. Furthermore, the spatial scale of the ripples is highly suggestive of the weak ripples visible upon a close inspection of the image in Fig. 6, taken through this same structure. This ripple is *not* evident in the data of Fig. 10, however, taken while the sample was immersed in water. This indicates that the source of those ripples is almost certainly isolated on the surface of the preform. This is valuable information. First, it renders the ripple unimportant for this application, as those surfaces will be completely diamond turned away. Second, it suggests to Case Western that there is likely some surface effect occurring at the interface between their sheets and the flat molds in the stack consolidation step. This information may prove valuable in a situation in which we *wouldn't* be able to diamond turn the surface away.

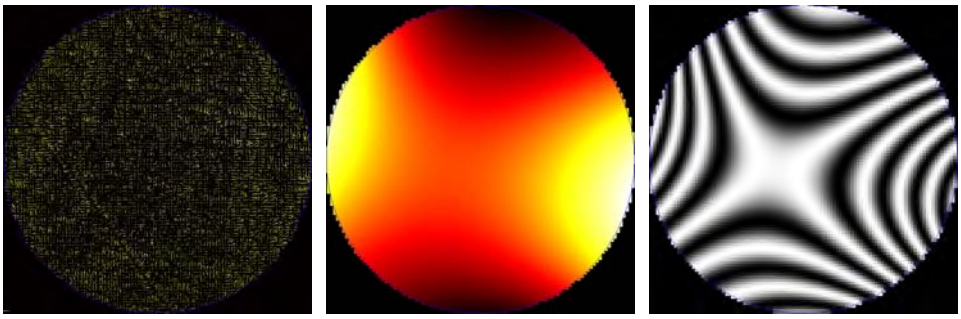

Figure 10: Shack-Hartmann measurements for axial GRIN preform 100104 in water, presented as in Figure 9. The peak-to-valley optical path difference is 3.7 waves. RMS deviation is 0.44 waves.

Though the data of Figs. 9-10 represent the best axial GRIN, even the sample with the largest wavefront deviations had less than 5 waves peak-to-valley with an RMS deviation of 0.6 waves. Remembering that it takes well over 2 waves RMS to have a significant impact on the expected optical quality of the prototype, all the axial preforms are expected to provide satisfactory imagery.

5. Wavefront results: Spherical GRIN

The spherical GRIN preforms present a much greater challenge for analysis. That is because the preforms themselves are meniscus lenses, which cause input collimated light to diverge. Furthermore, the measured wavefronts become sensitive to the exact placement & alignment of the optic with respect to the Shack-Hartmann instrument. As a result, it is not nearly as easy to quantify deviations in the measured wavefront from the design wavefront.

To best attempt this measurement, we illuminated the preform with slightly-converging light. The amount of convergence was varied while viewing the measured wavefront. The input light was considered properly chosen when the measured wavefront was at the transition between converging and diverging. What Zemax predicts for the wavefront at this stage is depicted in Figure 11.

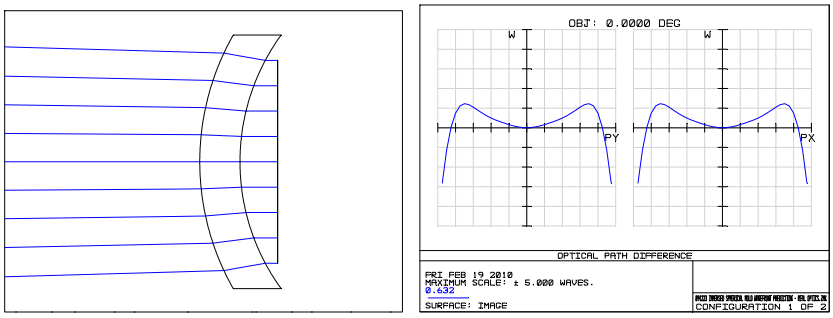

Figure 11: Calculated wavefront for ideal spherical preform. (L) Simulated raytrace. The input rays are converging on the lens in such a way that the preform collimates the transmitted wavefront as nearly as possible. (R) Plots of the transmitted wavefront. Data are plotted for rays along both transverse axes of the lens – since the lens & illumination are symmetric, the plots are identical. The horizontal axis extends ±8 mm, and the vertical axis extends ±10 waves in optical path difference, at a wavelength of 632.8 nm.

As can be seen from the right-hand side of Fig. 11, the wavefront is curved one way near the center of the lens and rapidly drops off the other way at the edge of the aperture. Peak-to-valley measurements of the optical phase difference don't mean much in this situation, as they are too sensitive to precise details of the field of view and the input light convergence. The same holds true for RMS measurements.

Nevertheless, the data were obtained. For sample #100101, these results are presented in Fig. 12.

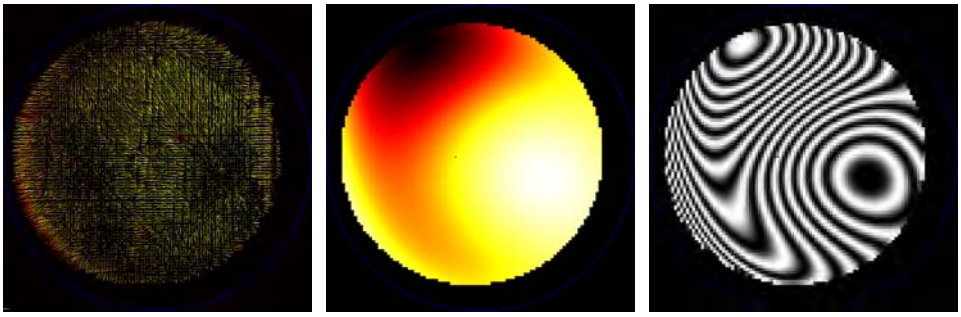

Figure 12: Shack-Hartmann measurements for spherical GRIN preform 100101. Data are presented as in Figure. 9.

An immediate observation is that the measured phase front is not symmetrical, as one would expect. Though this could be attributed to sample inhomogeneity, experimental misalignment cannot be ruled out. The wavefront is very sensitive to small displacements of the sample, and insufficient precision was available for careful sample positioning.

In the absence of hard, quantitative data on the spherical preforms, qualitative analysis of both the measured Shack-Hartmann and see-through visible images had to suffice. Figure 13 shows an image viewed through the same sample measured in Figure 12. These data were valuable for screening purposes and relative quality ranking. In no cases were wavefront deviations measured that even approached the 20 wave RMS limit necessary to ruin optical performance of the lens.

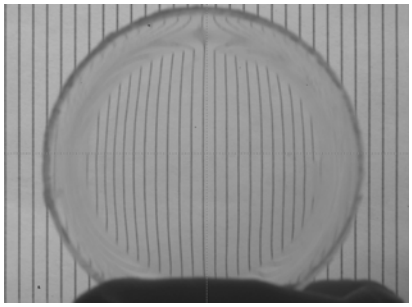

Figure 13: Image of straight lines as viewed through spherical GRIN preform 100101.

Addendum: While discussing metrology options with Robert Bupp of Nu-Tek on Feb. 23, 2010, we hit upon a different test set-up which would provide data exactly comparable to the axial data for these preforms. This opens up a much more quantitative avenue of metrology for spherical preforms in future efforts.

6. Diamond Turning Quality

Nu-Tek diamond turned a total of 26 optical GRIN surfaces during the course of this program. Of those, we have detailed maps of the 8 surfaces inside the assembled lens barrels. Several of the surfaces were of visible optical quality, demonstrating peak-to-valley surface deformations ~2 waves or less as measured by a HeNe laser. An example of such a surface is provide below:

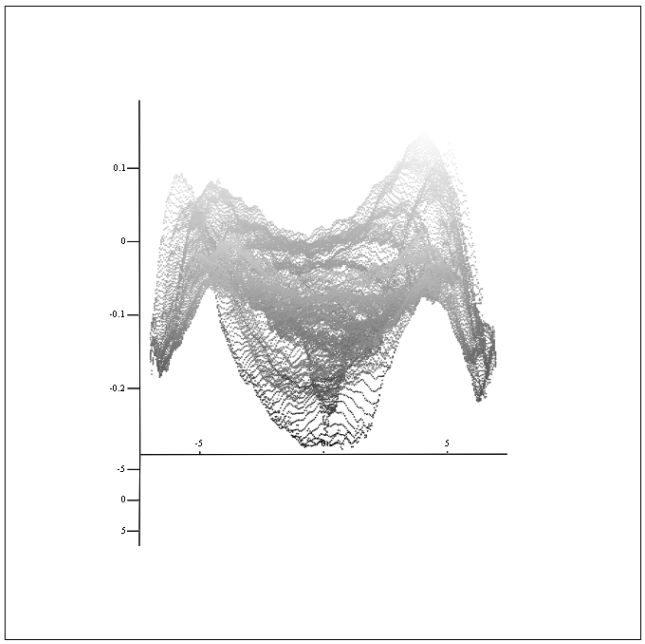

Surface map of the concave side of Lens 1. Vertical axis is labeled in waves deviation from spherical, as measured at 1.55 um.

Four of these surfaces were considered by Nu-Tek to be of inferior surface quality – three near 7 waves of peak-to-valley distortion across the field of view as measured with a HeNe laser, and a fourth outlier with over 23 waves peak-to-valley. Two comments should be made with respect to these numbers. First, is that these values do not accurately reflect the variability in lens manufacturing. Nu-Tek had to change personnel mid-stream, and the outlying surfaces resulted from the first few surfaces turned by the new engineer.

Second, while these numbers are large for the visible domain they are considerably smaller in the SWIR. Plus, our design can withstand several waves of distortion before becoming compromised, as indicated previously (Preform Screening and Analysis.) For the assembly with the worst surfaces, I calculated RMS wavefront errors measured at 1.5 um and added them up in quadrature. The final result was an estimated RMS wavefront error of 1.6 waves – less than the 2 waves recommended previously.

Thus, the GRIN materials have proven demonstrably amenable to diamond turning.

7. Mechanical Design

The mechanical design for the lens mount was subcontracted out to Welch Mechanical Designs, a small company based in Aberdeen, MD which specializes in optical mechanical engineering and assembly. A 3D model of a near-complete design is shown in Fig. 14.

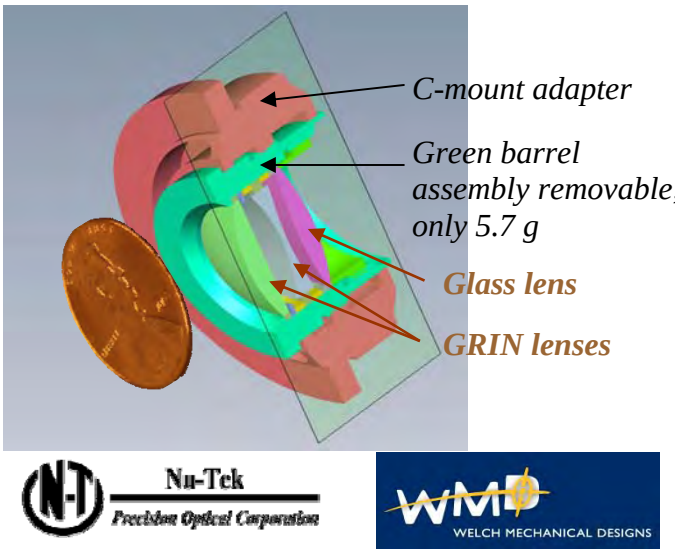

Figure 14: Cut-away of solid model depiction of lens barrel elements. Final weight of the entire assembly is < 11 g.

Broadly, the lens assembly consists of three components: 1) the outer (red) C-mount adapter, made of Delrin, which mates the optics to the lens mount on our InGaAs camera, 2) the inner (green) assembly, made of aluminum, which threads into the adapter and contains all the optics held fixed in their optimum positions, and 3) the optics and spacers which slide into place along a common bore radius within the inner assembly and are secured in place by a retaining ring threaded into the back of the assembly (behind the purple lens in Fig. 14.) The outer, C-mount adapter screws firmly into place on the camera. In several places it has material machined away to reduce weight while retaining mechanical rigidity. The inner assembly is threaded into the adapter with a fine thread, allowing for precise manual adjustment of the focal plane on the camera. A more precise drawing is provided in Fig. 15, which shows the only other component of the lens – a thin, aluminum shell which press-fits to the front of the lens. This element acts as a lens hood, minimizing stray light from propagating into the optics.

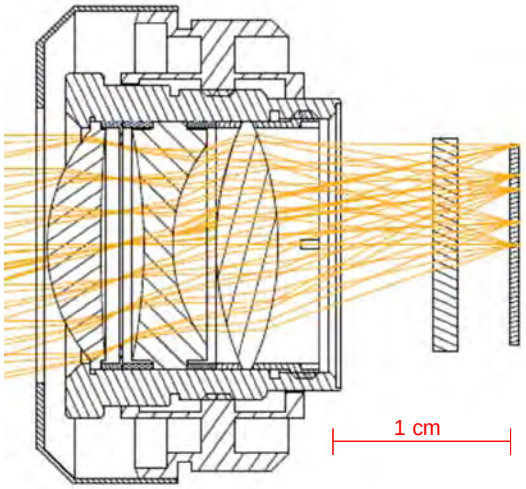

Figure 15: Mechanical drawing for lens barrel assembly. The flat elements on the right are internal to the InGaAs camera. The volume of the assembly is 8.4 cm^3.

The mass of the entire assembly, aluminum hood included, is to be less than 11 g. When fully screwed into the camera, the lens extends out only 8 mm. The volume of the lens assembly, including the aluminum cap, is 8.4 cm^3. Operationally, however, the lens does not require the C-mount adapter: the optics are fully contained in the inner assembly. This component has ***a mass less than 6 g and a volume of only 3.9 cm^3***. With a suitable camera interface, this would be sufficient for the full imaging capability of our design.

As a risk mitigation step, each assembly will come with a set of different-thickness spacers. By changing the spacers, one can assemble the system with different lens separations to account for any unexpected results in the lens material or process parameters. There was insufficient time and resources in this effort to exhaustively tolerance the design. As opposed to conventional optics where tolerancing algorithms are well established, there are no comparable algorithms to properly tolerance GRIN lens designs. Nonetheless, Prof. Rich Lepkowicz and his students at Rose Hulman Institute of Technology calculated the effects of "normal" lens variations (radii of curvature, center thickness, decentration, etc.) as compensated for by back focal length adjustment and lens spacings. Their analysis found that varying the separation between lens 2 and lens 3 was particularly helpful in accommodating adjustments in the lens specifications. The maximum variation needed in the lens spacing was around ±150 um from the nominal vertex-to-vertex distance of 2.4 mm.

8. StingRay Comparison Lens

The prototype design of Figure. 1 arose from an early collaboration with Army's Night Vision Laboratory, in Fort Belvoir, VA. As long ago as the spring of 2007, we at NRL met with a group there to discuss the then state of the art in the GRIN lenses. Excited by what they saw, they shared with us some applications that were actively seeking out lightweight SWIR lenses. In particular, they mentioned a monocular lens for a helmet-mounted night vision camera. A program was already underway to specify a lens that had high light gathering capability with low weight. They shared with us some preliminary designs for the optic, one of which is shown in Figure. 16.

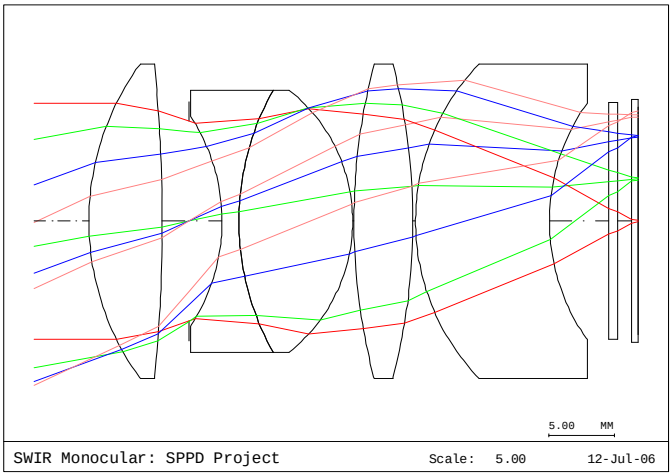

Figure 16: Preliminary optical design submitted to Night Vision Labs for a SWIR monocular. The 5 glass elements of this lens system, before integration into a mount, have a mass of 36 g.

The end result of the project was a lens designed by StingRay optics. A CAD model of the packaged StingRay lens is depicted in Fig. 17. Despite several requests, StingRay respectfully refused to share details concerning the optical layout, or even number of elements in their design.

Figure 17(a): Solid-model depiction of the StingRay lens that will be compared to our prototype. Weight of the assembly is 65 g. Optical design specifications are 18 mm focal length, f/1.1, 50° field of view, MTF curves targeted to 40 um pixels, wavelength range 1.0-1.6 um.

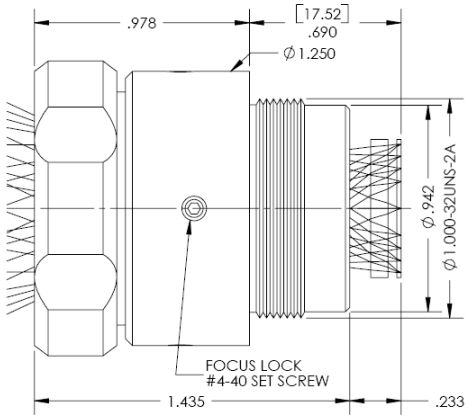

Figure 17(b): Mechanical drawing of the StingRay lens. Dimensions are in inches. The volume of this lens is approximately 1.8 in^3, or 29 cm^3.

This lens represents the state of the art in SWIR optics. It is a custom design, funded by a military institution that cares deeply about the weight carried by a soldier trying to see in the dark. StingRay is rightfully proud of this lens: many copies of it went out into the field, and are used by our soldiers today. As part of this program, we purchased a copy ourselves for the purpose of a direct comparison between this lens and our prototype. The optics are excellent, with an impressive 50° FOV at f/1.1 and MTF curves as reported by the company, copied in Fig. 18.

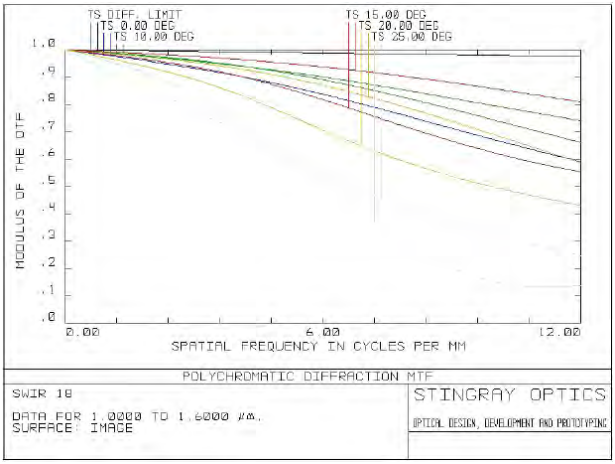

Figure 18: Design MTF curves for the StingRay lens. Note that the design goal for this lens is not 20 mm^{-1}, but rather 12 mm^{-1}. The maximum field of view is 50° and the speed is f/1.1.

One way to crudely interpret MTF curves is to locate the spatial frequency at which they reach a value of 0.5, and convert that frequency to an effective camera pixel size. For a pixellated camera with a pixel pitch of Δx, a common goal is to achieve an MTF curve >0.5 at a spatial frequency of $1/(2\ \Delta x)$. There are lots of curves in Fig. 18, each one representing either the tangential or sagittal directions for light coming in at different angles (see some of the MTF comments in the *Optical Design* section). Some of them, representing light from objects at the edge of the field of view, dip below 0.5 even before 12 mm^{-1}, but if we trend most of them by

eye we might guess that around half of them are below 0.5 at a frequency ~14 mm^{-1}. This corresponds to a camera with 36 um pixels.

By contrast, the majority of the field of view for our lens & camera is expected to have better resolution, despite the much smaller size, the much lighter weight, and with only 60% of the number of lenses. The aspect ratio of our camera sensor is similar to a Power Point slide. Within a circle which extends to the vertical edges of the sensor (defined at the very edge by the green curves of Fig. 3a) the majority of the image has MTF curves which are greater than 0.5 well past 20 mm^{-1}.

9. Polymer Film Dispersion Measurements

The GRIN modeling efforts at Optical Research Associates and at NRL need to accurately model the refractive index of a GRIN optic over a broad range of wavelengths. The model requires accurate measurements of the base polymers used in the fabrication of GRIN films. In support of this effort, NRL measured the refractive index of 4 polymer films: SAN17, 50/50 Blend PMMA/PVDF, PVDF copolymer, and PMMA. These films represent the present and near-future building blocks for GRIN lenses. Current-generation optics are made from composites of PMMA (n_d=1.49) and SAN17 (n_d=1.58). [The index values n_d cited here are those measured at the Fraunhofer d-line, an emission line of helium at a wavelength of 587.6 nm.] Case Western has already started the process of implementing a lower index polymer, PVDF (n_d=1.40), to increase the maximum Δn. The PVDF copolymer material alone is not compatible with the material processing needed to fabricate GRIN sheets, but there has been preliminary success with a blended PVDF/PMMA material (n_d=1.45).

The index values were measured at 6 different wavelengths on a Metricon Model 2010/M Prism Coupler instrument. The instrument was calibrated with a quartz standard. Following this calibration, an instrumental accuracy of ±.0001-.0002 is quoted by the manufacturer. From the measured values, fits were made to a Cauchy equation which can provide index values for intermediate wavelengths. The Cauchy equation used here is given by:

$$n(\lambda) = A + B\,\lambda^{2} + C\,\lambda^{-2} + D\,\lambda^{-4}$$

The fit parameters and the resulting RMS deviations from the original data are reported in Table I.

	A	B	C	D	RMS Fit	Abbe #
PVDF copolymer	1.396134	- 0.0008354992	+0.002932773	-1.188913×10^{-4}	2×10^{-4}	93.7
50/50 PMMA/PVDF	1.440109	- 0.0002033909	+0.004511930	-2.302767×10^{-4}	2×10^{-4}	79.1
PMMA	1.479702	- 0.0004751835	+0.004545040	-8.611963×10^{-5}	2×10^{-4}	64.9
SAN 17	1.541835	+0.001839227	+0.01489096	-9.032005×10^{-4}	9×10^{-4}	34.4

Table I: Cauchy coefficients A-D for each polymer found by least-squares fitting of dispersion data measured at 6 wavelengths (473 nm, 532 nm, 633 nm, 992 nm, 1057 nm, 1546 nm). Also reported are the root-mean-squared deviations of the fits from the data and the Abbe number for each polymer.

An example data set, showing both the measured data points and two different dispersion curve fits for the PMMA data, is shown in Figure 19. As another indication of the quality of these data, independent measurements of PMMA have been reported in OSA's Handbook of Optics, vol. II at several wavelengths from 0.365-1.014 um. For the Metricon measurements which fall within this range, a curve fitted from the Handbook data points generates values which differ from our Metricon measurements by an RMS deviation $<5x10^{-4}$.

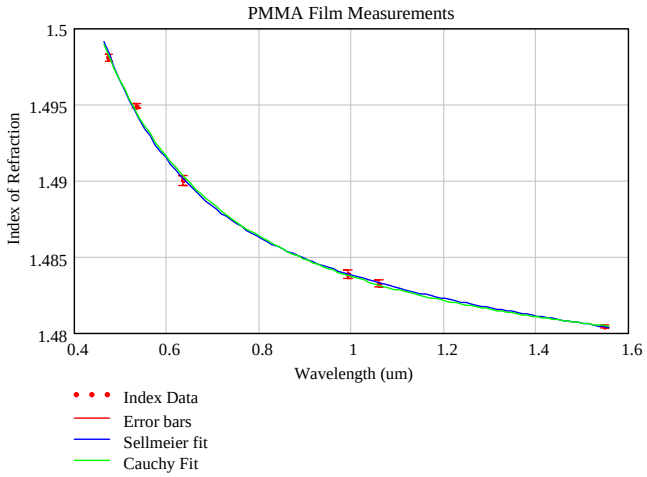

Figure 19: Discrete measurements of PMMA

Two comments can be made concerning the data reported in Table I. The first is that a plot of the SAN17 dispersion curve is found to differ from the curve reported in the previous progress report of this program by values $\sim10^{-3}$. That is directly attributable to the recent calibration of the Metricon instrument to a reference standard. The numbers reported here are more accurately measured, and the magnitude of the discrepancies is what was quoted in the previous report for an uncalibrated measurement.

The second comment relates to the RMS deviations from the fits. The fits reproduced the data to a $\sim10^{-4}$ level, as expected from the instrumental accuracy, for all materials except SAN17. For SAN17, the fit was accurate only to the 10^{-3} level. The source of the deviations in SAN17 is being investigated.

In addition to the measurements at 6 specific wavelengths in the Metricon instrument, considerable effort was expended to measure transmission spectra for each sample in a spectrophotometer over a wavelength range of 400-1700 nm. These data were taken at a spectral resolution fine enough to resolve etalon fringes, which will provide detailed information on intermediate refractive index values. An example data set is shown in Fig. 20. The gap in the data corresponds to a transition region of the instrument at which it switches both the monochrometer grating and detector. In this region the signal to noise ratio was insufficient to recover fringes at all.

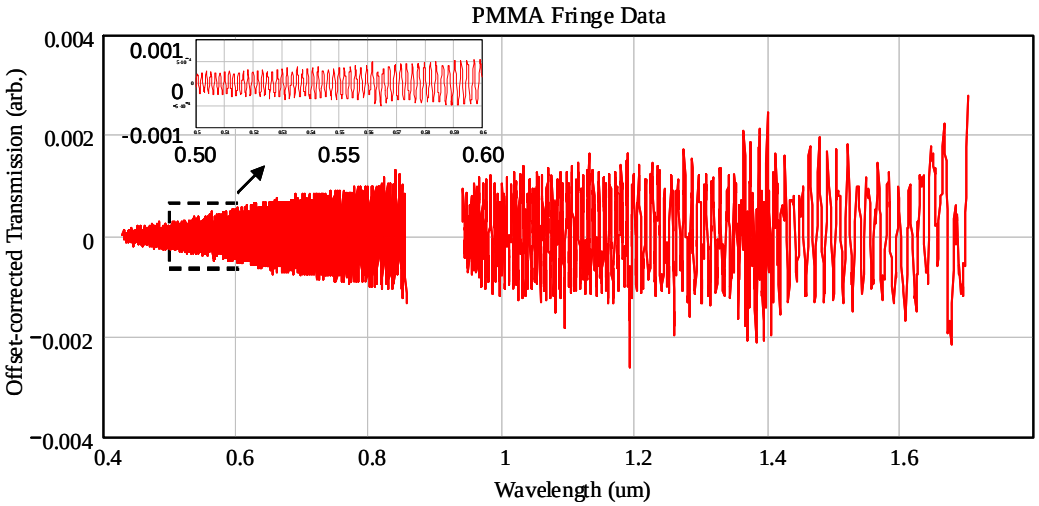

Figure 20: PMMA fringe measurements. Plotting the data at this resolution fails to resolve all fringes, which become visible upon expanding the full dataset, more than 4,800 data points.

Fringe measurements such as these should lead to a much greater density of index measurements. In principle, each peak and valley of the fringe spectrum provides its own index measurement. In practice, small systematic errors result in unacceptable errors in the analysis. Figure 21 show a dense set of dispersion measurements extracted from the data set of Fig. 20, as bounded as well as possible by the Metricon measurements of Fig. 19. As is easily seen, there is a sharp discontinuity in the data near the gap in the spectral data.

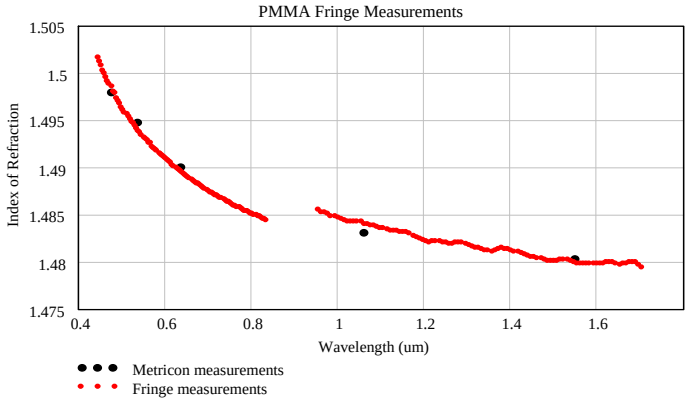

Figure 21: Index measurements extracted at each peak of the PMMA fringe data (red points) compared to the data taken in the Metricon prism coupler (black dots).

The discontinuity is not directly caused by the coverage gap itself, but rather appears to arise as a consequence of systematic errors introduced by different acquisition parameters on one side of the gap relative to the other. For the purpose of this program, it is likely that the 6 measurements from the Metricon are sufficient to generate adequate dispersion curves. Future work, however, will allow us to examine these curves more closely and identify the cause of the slope discontinuities. At that point, we should be able to measure the dispersion curves with far higher accuracy.

10. Programmatic Lessons Learned

As with all programs, this effort experienced unexpected twists and turns. There were two unexpected hurdles, in particular, that will serve to inform future efforts with the GRIN lens material.

The first hurdle was diamond turning the fine edge features requested by Welch Mechanical for proper mounting of the lenses in the lens assembly. Figure 22 contains the relevant portion of the mechanical drawing for the lens:

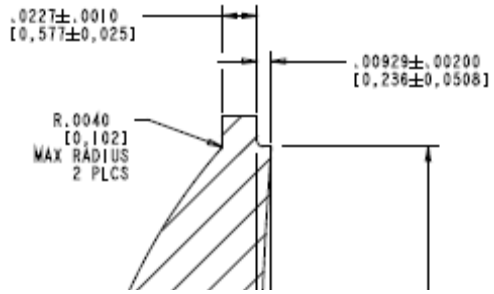

Figure 22: Portion of mechanical drawing for Lens 1, focusing on the edge details. Units of upper (lower) numbers are inches (millimeters). Note in particular the 0.236 mm lip and the very small radius of curvature (~50 microns) at the corner of the lip on the RHS.

Initial approval of this design by Nu-Tek was based on their judgment that these features would pose little trouble to the diamond turning process. This type of edge feature can be programmed into the diamond turning machine, and cutting tools exist to support the fine features requested. What was not anticipated, however, was the difficulty in securing the lens firmly enough to enable accurate machining. Customarily, optics are held in place using vacuum chucks during the diamond turning process. The force with which optics can be secured this way is proportional to their surface area. By ensuring that the vacuum force is larger than any forces imparted on the optic by the machine tools, the lens can hold steady for accurate diamond turning.

These lenses, however, unexpectedly crossed this threshold. They were small enough, and the edge detailing imparted enough force, that vacuum fixturing proved insufficient for diamond turning. As a result, new methods had to be developed to hold the lenses secure during fabrication. Developing the new methods took substantial time, compounded by the fact that the methods required diamond turning to occur at a much slower pace than anticipated initially.

The feature could not be ignored, however, due to the tiny distances already existing between lenses. Shown in Fig. 23 is a magnified portion of the drawing for the entire lens assembly, showing the details of the aperture and spacer between lenses 1 and 2.

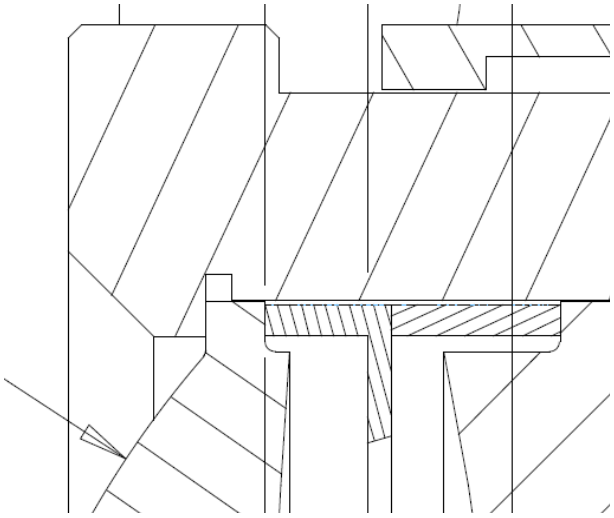

Figure 23: Expanded detail of the assembled lens. The arrow points to the front surface of Lens 1, secured against the lip of the inner, Al barrel. In contact with the right surface of the lip on Lens 1 is the aperture stop ring, followed by a precision spacer for proper spacing of Lens 2.

It was determined by Welch Mechanical that the lip on Lens 1 was required in order to maintain structural integrity of the aperture ring placed immediately to its right. In the absence of the lip on Lens 1, the tangential length of the ring would be too short to maintain sufficient rigidity during machining or lens assembly.

The second hurdle overcome during the program was potentially the most disastrous. To maintain proper optical throughput, it was clear that we would want the GRIN lenses anti-reflection coated. Because of the cost of coating runs and to ensure coating consistency, it is common practice to run all parts together in a coating run. It was naturally assumed that because the lenses were fabricated from common optical plastics, they would be amenable to standard acrylic coating processes.

Unfortunately, the GRIN materials were *not* compatible with the coating process. Every painstakingly diamond turned element was ruined in the first coating run. Not only did the coatings improperly cover the lens surfaces, the lenses themselves became “warped” while in the deposition chamber. Deformations from true were extensive. Diameters shrunk from the design value of 14.0 mm by as much as 0.5 mm, while center thicknesses grew by 0.25 mm or more. As an indication of how extensive the changes were, the front lenses went from a meniscus shape to convex-convex – the slightly concave surface swelled to the extent that it became slightly convex. These changes were accompanied by an overall warping of the parts that resembled a potato chip.

This result was difficult to overcome. Because it was the second-to-last step in the fabrication process, a process already delayed due to the issues which arose during diamond turning, it left us with nothing in hand with almost no time left to recover.

We are able to claim success for this program only due to the preparedness of Case Western Reserve University and the dedication of Nu-Tek to continue to perform costly diamond turning

in advance of any further funding. Case Western Reserve University had one pair of GRIN preforms left over from the initial sheet fabrication process, and they were able to generate another pair in just one week. Nu-Tek, despite commitments to other customers and the red ink they were accumulating on this project, managed to diamond turn first the backup preforms and then the second pair in time for the program review.

The root cause of the failure in the coating chamber is yet to be understood. It will likely require some time to isolate the different effects of the coating process, and we were forced to leave that for the future by time constraints.

It should also be pointed out that a larger-than-expected effort was undertaken on the part of NRL to characterize the lenses. This is because, after over two weeks of solid effort on NRL's part, it was reluctantly concluded that the pixels in the InGaAs camera used to characterize the lenses exhibited some crosstalk – features one pixel wide would 'blur' across neighboring pixels. Discussions with infrared camera experts both at the camera's company and in the Optical Sciences Division at NRL suggest that this is an intrinsic deficiency of the camera infrastructure, and not the result of a faulty unit. To provide accurate measurements of the lens resolution, therefore, NRL had to quickly develop a different technique for measuring the resolution: scanning a razor blade through a tightly-focused laser beam.

11. Measurements of the Delivered Lens

The delivered lens, as promised, is significantly smaller and lighter than the state-of-the-art lens it was modeled after. Figure 24 is a picture of the two lenses placed next to each other.

Figure 24: Picture of the StingRay lens (foreground) compared to the GRIN lens developed in this program. The StingRay lens weighs in at 57.74 g, while the GRIN lens weighs 7.74 g.

As one might expect from the photo, the GRIN lens is significantly lighter than the StingRay lens: 7.7 g versus 57.7 g. The volume is also obviously less. Mounted on the camera, it is clear from Figure. 25 that the GRIN lens would be less obtrusive for helmet-mounted applications, which is what the StingRay lens was designed to do.

Figure 25: Comparison of the size of each lens while placed on the InGaAs camera.

Two images captured with the InGaAs camera are presented in Figure 26. Several corrections to the raw data are required before the images can be analyzed. First, there are several corrections performed by the camera to adjust for pixel-to-pixel nonuniformity. Second, we performed corrections to account for illumination nonuniformity across the field of view. The target image contains several sharp transitions from dark to light, designed so that modulation transfer functions can be computed at different positions in the field of view.

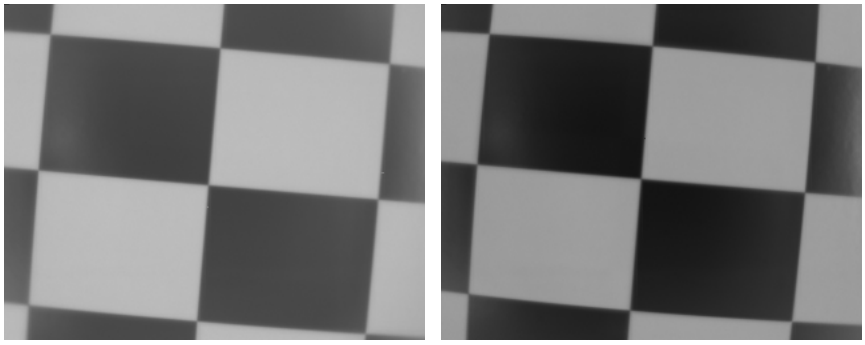

Figure 26: Test images taken with the GRIN lens (L) and StingRay lens (R).

Two principal observations can be made simply by looking at the images. First, the StingRay image exhibits a noticeable barrel distortion, as evidenced by the way straight lines at the edge of the field curve outward from the center point. By contrast, the image provided by the GRIN lens shows far less distortion. Second, the dark squares in the GRIN image are not as dark as the squares of the StingRay image. This suggests that there is an overall light background associated with the GRIN image not present in the StingRay image.

This is unsurprising, considering the lack of anti reflection coatings in the current GRIN lens. With an average index of refraction of 1.53, it is estimated that over 20% of the incident light is reflected at uncoated lens surfaces. While much of this light is expected to reflect back out of the lens barrel, a portion of it will nonetheless scatter onto the sensor, creating a background of scattered light.

A direct examination of the MTF performance of these lenses using the InGaAs camera is, regrettably, compromised by the InGaAs camera architecture. Over two weeks of measurements under various different illumination conditions through simple and complex lenses was required

before NRL was convinced of the source of the problem: neighboring pixels in the InGaAs sensor are not independent. As a result of this information sharing, edges get blurred across neighboring pixels even in the presence of ideally-sharp optics.

Measures taken to confirm this included comparing images acquired through several singlet lenses to Zemax simulations of image performance. With simple BK7 singlet lenses, Zemax can calculate with good accuracy the expected image quality at the focal plane. By limiting both the input aperture and illumination wavelength, we could set up situations specifically designed to provide sub-pixel edge features on the InGaAs camera. When this failed to result in sharp images, we tested the concept on a silicon-based camera. While we were unable to produce images sharp enough to give single-pixel resolution for this camera, which had pixels 6 times smaller at a 4.4 micron pitch, we could nonetheless confirm the agreement between our simulated and detected image resolution.

We also performed our own full-camera calibration for the InGaAs sensor, to rule out effects of gain nonlinearities. By recording a series of images taken with different signal levels, we were able to map out the signal response curve for every single pixel. We fit each curve to a nonlinear response model designed to fit the data, and then used these curves to correct raw images of our test objects. This procedure did not improve upon the onboard camera corrections, however, leaving us once again with edge features blurred across several pixels when the optics would suggest sub-pixel edges.

Subsequent conversations both with the camera company and with experts in IR sensors within NRL's Optical Sciences Division suggest that the problem is intrinsic to the sensor architecture, and not the result of a faulty unit. For completeness sake, we nonetheless provide some MTFs calculated from several captured images, taken for both narrowband and broadband imaging. The narrowband imaging was achieved by capturing images through a 30 nm FWHM bandpass filter centered at 1.55 microns, while broadband imaging was achieved by removing all filters. The target was illuminated by two incandescent bulbs indirectly, by being pointed away and scattered off white posterboards placed to either side of the target.

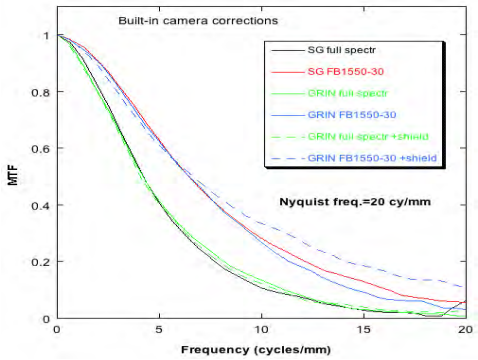

Figure 27: MTF curves calculated near the center of the field of view, from images acquired for both the GRIN and StingRay (SR) lenses. Images were acquired either through a narrowband 1550 nm filter (FB 1550-30) or with no filter at all (full spectr). Images were also acquired for the GRIN lens with a shield in place to prevent possible light leakage through the Delrin C-mount adapter. Past experience has shown that Delrin can sometimes be translucent in the SWIR.

MTF curves measured from a series of these images, similar to those shown in Figure 26, are presented in Figure 27. The curves for both the GRIN and StingRay lens are nearly identical, for narrowband and full-spectrum illumination. This comparison is not as promising as it might seem, however, because of the values of the MTF curves. For both lenses, it is anticipated that the MTF curves should remain above 0.5 well past the modest spatial frequencies depicted in Fig. 27. It was likely that the curves presented in Fig. 27 indicate the sensor response, as opposed to the lens response – a supposition proven below.

Cognizant of the limitation of the camera's resolution and determined to provide a more-accurate measure of the true lens performance, NRL rapidly assembled a test setup at a very late stage of the program. A schematic of this setup is provided in Fig. 28.

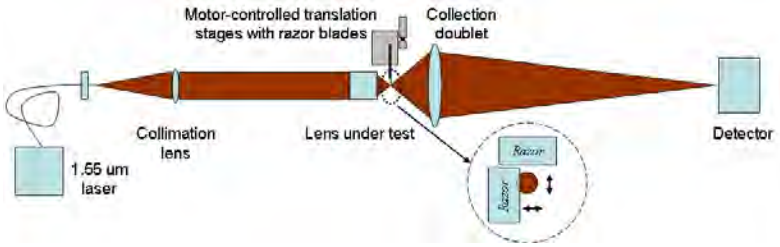

Figure 28: Experimental setup for measuring more-accurate lens resolution. See text for details.

In this test, a 1.55 μm, fiber-coupled laser source is collimated and directed onto the lens under test in such a way that the light is nearly-uniform across the input aperture of the lens. (Measurements of the input intensity profile show that there was some dropoff in intensity: ~12% at the edge of the GRIN lens and down to ~20% for the larger StingRay lens.) This light is focused down to a very small point behind the lens, the intensity distribution of which is defined as the point spread function of the lens for on-axis light.

To get an approximate measure of this function, a razor blade is moved across the spot with a translation stage using computer controlled actuators. As the razor blade moves through the focused spot, a detector records the transmitted light energy; the smaller the spot, the smaller the travel distance required by the razor blade to switch between blocked and open beam paths. The resulting plot of transmission versus razor position can be used to calculate the MTF curve of the lens.

The challenge posed by this experiment lies in the collection optics placed behind the lens under test. In order to collect all the light, these optics must have an f/# and MTF at least as good as the lens under test. The problem in this case is that we're testing state-of-the-art lenses – we *have* no collection optics of comparable quality for the SWIR. The best we could do was come up with an f/1 air spaced doublet which, while fast enough, doesn't have nearly the same MTF performance as our lenses. As a result, light captured by the lens is not focused down to a small spot at the detector. This is made up, in part, by having a fairly large detector. We used a 8 mm diameter Ge detector from New Focus. Given the optical quality of the doublet, however, even this detector isn't expected to be large enough to capture all the light collected in the experiment.

The net effect of the compromise is that the detector, being large enough to detect light from only part of the beam, will be sensitive only to a subset of the point spread function.

Shown in Figure 29 are the razor scans recorded for both the GRIN and StingRay lenses. Scans were taken in both the horizontal and vertical directions, and averaged to provide the final traces. The motorized actuators (Newport LTA-HS and LTA-HL) are specified accurate to less than a micron. The principal uncertainty in positioning is expected to lie with the quality of the stages themselves, which are little, 1.75" travel crossed-roller linear translation stages (Edmund NT56-362).

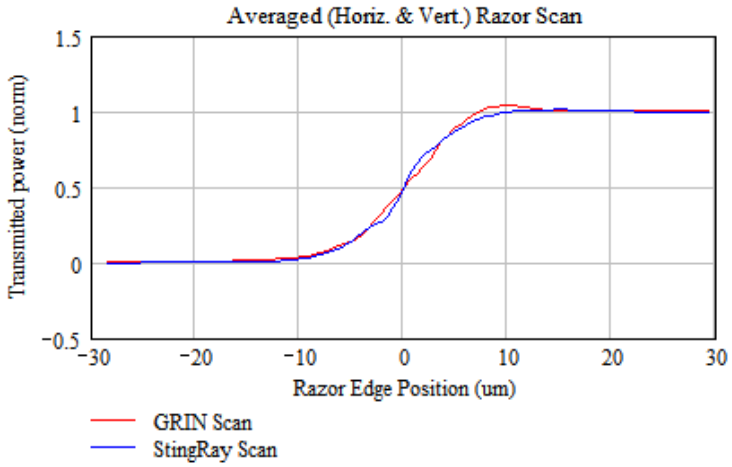

Figure 29: Razor scan data for the GRIN lens (red) and StingRay lens (blue), averaged over the horizontal & vertical directions. For each lens, the distance travelled between the 10% and 90% points on the curve is 12 μm.

Figure 29 shows that the razor profiles of focused spots behind each lens were found to be identical in this setup. The 10-90% transition distance for each lens was measured at 12 μm. By contrast, the blurry InGaAs camera recorded distances in excess of 75 μm for the same transition. It would appear that the razor scan setup is capable of measuring resolutions ~6x finer than those of the InGaAs camera, and that at this resolution the GRIN lens once again matches the performance of the StingRay optic.

The data of Figure 30, however, confirm the earlier suspicion that the collection optics in this setup fail to account for all the light transmitted by the SWIR lenses. Plotted in Figure 30 are the MTF curves for each lens as calculated from the razor scan data. Also plotted, in green, is the curve predicted by Zemax if the GRIN lens were fabricated precisely as Zemax designed it.

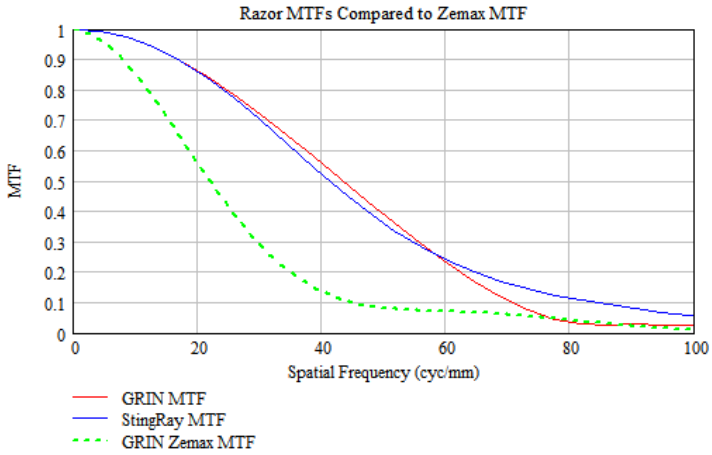

Figure 30: MTF curves calculated from the data of Fig. 29 (red & blue) compared to the Zemax prediction for the GRIN lens under the conditions of the experiment. The Zemax MTF curve is far lower than those calculated from the razor scan data, leading us to believe that the razor scan data overestimate the resolution performance.

As can be seen from the data, the razor scan curves imply focused spots even smaller than predicted for a perfectly-fabricated GRIN lens. Similarly, the StingRay MTF curves presented in Fig. 18 fail to go out as far as the blue curve shown in Fig. 30. This leads to the conclusion that the razor scan data overestimate the true lens resolution, due to the fact that the collection optics provide light from only a subset of the point spread function, making the focused spot look smaller than it actually is.

Despite the unexpected difficulties in measuring the MTF performance of our lens, one thing remains clear: in all apples-to-apples comparisons of image resolution, the GRIN seedling lens performed equally well as the StingRay lens, with 40% fewer lens elements, 7 ½ times less weight, and nearly ¼ the volume. It should also be pointed out that this performance comes without even the chance to optimize the GRIN lens spacings. As part of the barrel fabrication, Welch Mechanical provided us with a large number of custom spacer rings. As mentioned above (Mechanical Design) these rings were provided as a way to tweak the lens spacings as needed to account for fabrication tolerances. It is possible that, had we some time to experiment, we could find an optimum lens spacing capable of delivering even better performance than we see already.

Optical Research Associates Final Report

Abstract

ORA has implanted a polynomial representation of a spherical/cylindrical Gradient Refractive IndexGRIN in LightTools to describe the revolutionary materials developed by Prof. Eric Baer at Case Western Reserve University and researchers at the Naval Research Laboratories. This implantation in an industry standard software package will allow users to easily design optical systems with the new class of materials. The polynomial function and the graphical user-interface (GUI) in LightTools are described in detail. Currently, the model is undergoing testing, documentation, and implementation of a catalog of GRIN materials that can be user selected with the GUI.

1. Background

Researchers at Case Western University, working with SAIC with support and funding from the Naval Research Laboratory (NRL) have demonstrated the feasibility of a new type of GRradient INdex (GRIN) lens. This lens is modeled after recent discoveries related to the microstructure of insect and, in fact, human eyes. It has been found that eyes, in general, are formed much like trees, with concentric growth layers as illustrated in Figure 1.

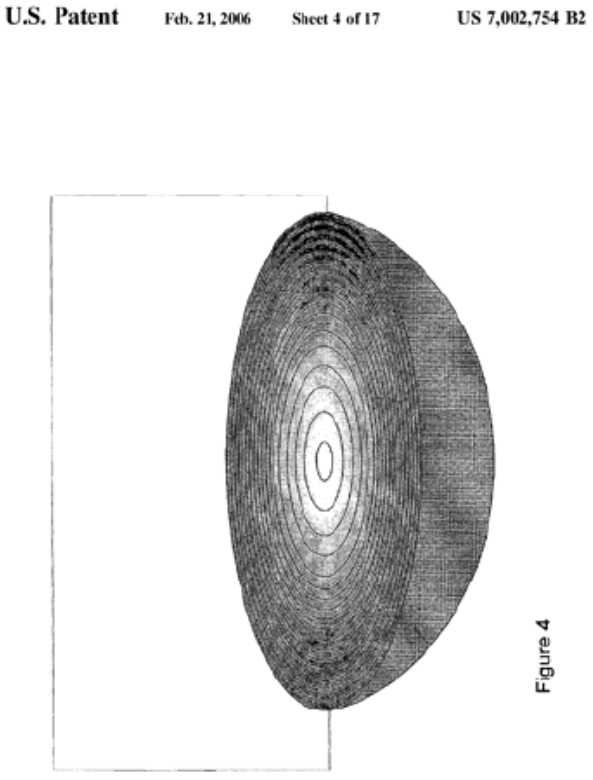

Figure 1. Illustration of the concentric layers found to be representative of most biological eyes. From US Patent 7,002,754 B2 assigned to Case Western, 2006.

Eric Baer in particular, working at Case Western, has been successful in mimicking the insect and human eye structure by perfecting a process, partially illustrated in Figure 2, whereby many thousands, and even tens of thousand of layers of polymer materials are combined to form a single Layered GRIN optical element (L-GRIN) of superior quality.

The index of refraction can be varied anywhere between that of the two materials, by changing the fraction of layers of each material. If the fractional composition of each material is varied throughout the material stack an axial GRIN material is obtained.

A cylindrical GRIN can be obtained by heating the axial GRIN and placing it between a pair of cylinders. This deforms the axial GRIN into a cylindrical GRIN, as illumstrated in Figure 2. Likewise, if a spherical GRIN can be obtained by heating the axial GRIN and placing it between a pair of concentric spheres.

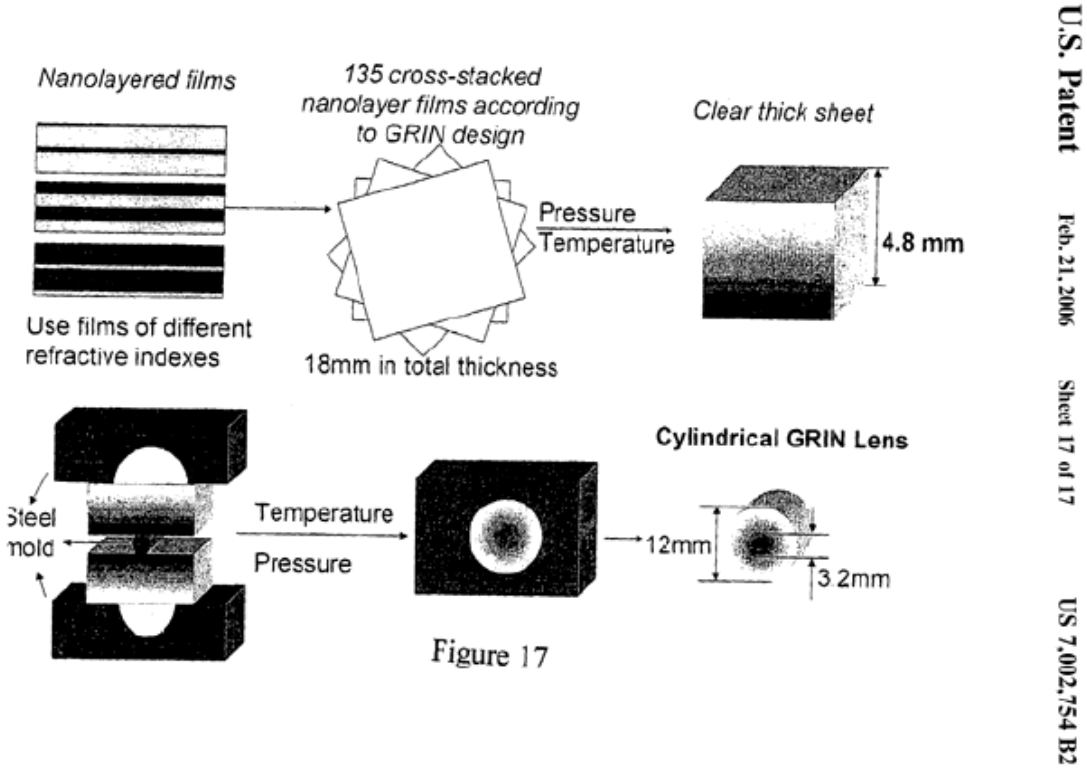

Figure 2. Illustration of the concept of assembling thin polymer film layers to create a new type of GRIN lens, the L-GRIN. From US Patent 7,002,754 B2 assigned to Case Western, 2006.

Optical Research Associates (ORA) develops, distributes, and maintains the most comprehensive and advanced optical system design and analysis software in the world. In this role, we are often involved in developing algorithms and user environments that enable integrating new optics technologies into a commercial optical design and analysis environment so that optical designers throughout the industry can explore the applicability of the newest technologies in the

applications they are working to advance. DARPA, in particular, has looked to ORA to fulfill this role since 1996.

With this background, the mission for ORA in this program is to again enable access for the national design community to an evolving optical technology, L-GRIN lenses. While there are a number of optical design and analysis environments available to the national community, ORA's optical design environments are unique in two important ways. First, they have the only commercially available global optimization environment that can operate effectively with high variable counts because of their proprietary technology, developed in the early 90s, does not scale as the number of variable to a power, as some other methods. As a result, as is the case in the world of chess playing, computer-aided design in ORA's environment has been demonstrated to outperform even the best optical designer (since 2002). Second and even more relevant to this program, in the late 70s ORA developed a differential technique that was both fast and accurate for establishing manufacturing tolerances for optical components. As a result, ORA provides the only optical simulation environment where tolerance analysis can be performed in real-time, interactively. This empowers the optics designer to not develop the best nominal optical design (which is by almost always not the most manufacturable) but to develop in fact the most manufacturable solution, which is the most relevant and effective solution. It is particularly this latter characteristic that is important for this L-GRIN development program.

2. Classic spherical GRIN lenses

In addition to animal eyes that inspired Eric Baer's research, there are several well known examples of spherical GRIN lenses in the literature. These lenses have not been commercialized, because of the difficulties in manufacturing the GRINs that this program adresses.

2.1 Luneburg lens

A Luneburg lens is perhaps the most famous spherically symmetric, variable-index refracting lens (see Fig.3 and equation 4). It forms perfect geometrical images of two given concentric spheres onto each other. The Luneburg lens is a spherical lens (usually a ball lens) generally having a gradient of decreasing refractive index *n* radially out from its center. The focusing properties of the Luneburg lens can be achieved through an infinite number of refractive-index solutions. The simpliest such solution was proposed by Rudolf Luneburg in 1944.[1] Luneburg's solution for the refractive-index creates two conjugate foci outside of the lens. The solution takes a simple and explicit form if one focal point lies at infinity, and the other on the opposite surface of the lens. J. Brown and A. S. Gutman subsequently proposed solutions which generate one internal focal point and one external focal point.[2][3] These solutions are not unique; the set of solutions are defined by a set of definite integrals which must be evaluated numerically.[4]

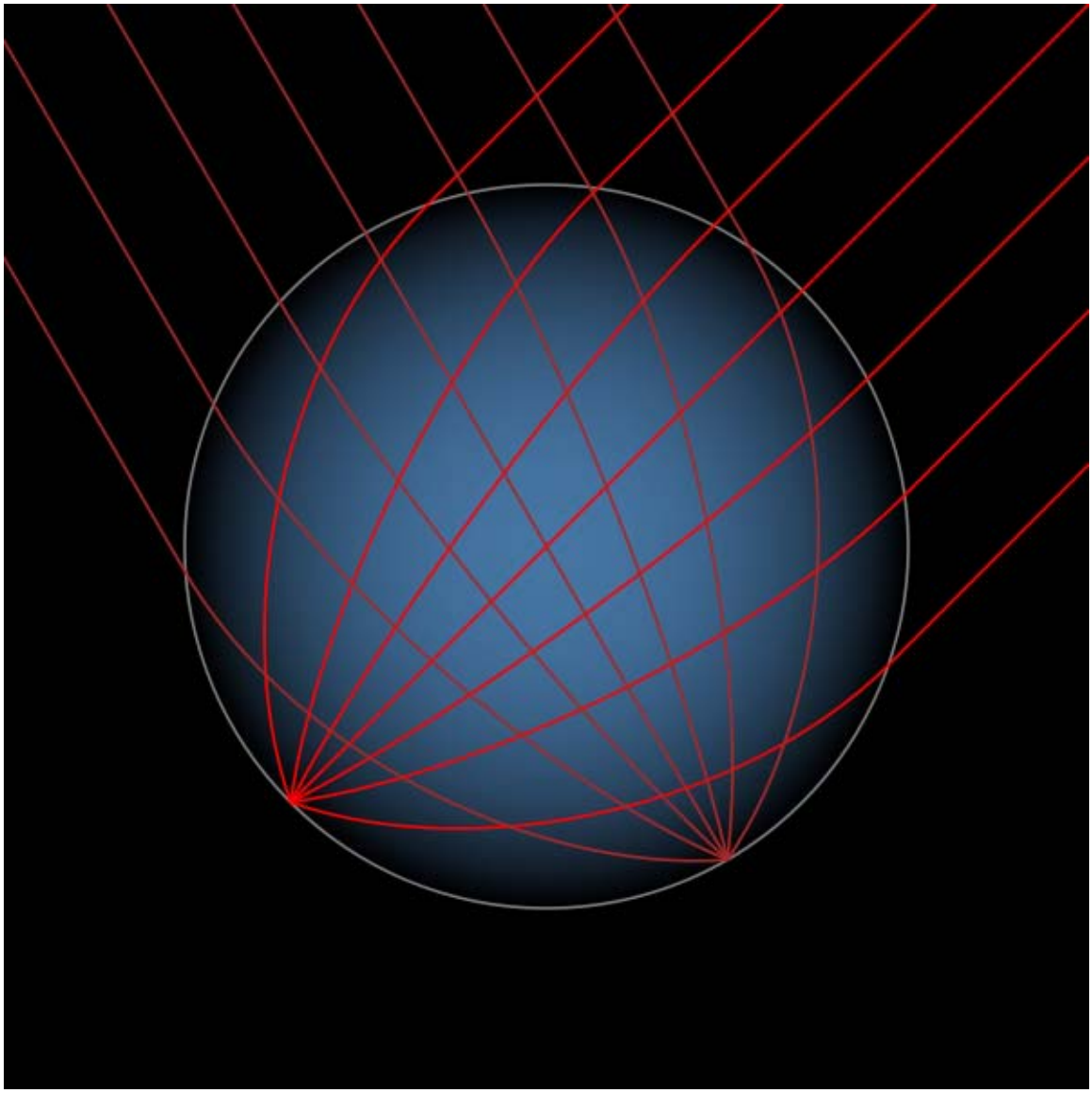

Figure 3: Cross-section of the standard Luneburg lens, with blue shading proportional to the refractive index (from Wikipedia).

2.2 Maxwell's fish-eye

Maxwell's fish-eye is also an example of the generalized Luneburg lens. The general fish-eye, which was described by Maxwell in 1854 (and therefore pre-dates Luneburg's solution), has a refractive index varying according to equation (1).

$$n = \sqrt{\epsilon_r} = \frac{n_0}{1 + \left(\frac{r}{R}\right)^2}. \qquad (1)$$

It focuses each point on the spherical surface of radius *R* to the opposite point on the same surface. Within the lens, the paths of the rays are arcs of circles. See Figure 4.

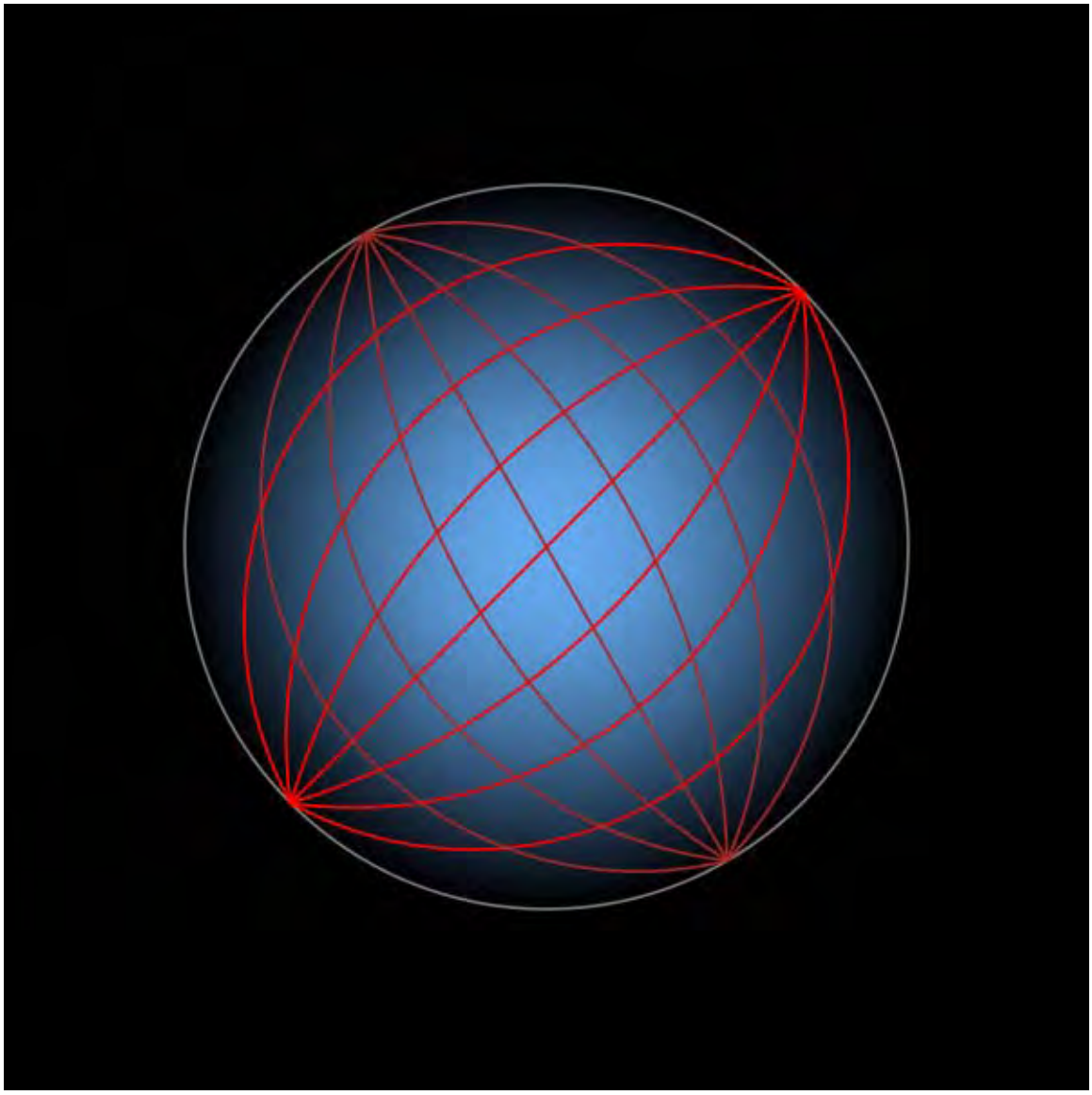

Figure 4: Cross-section of Maxwell's fish-eye lens, with blue shading representing increasing refractive index (from Wikipedia).

3. L- GRIN Representation

The refractive index of the spherical grin material is described by the following equation:

$$N(r,\lambda) = N_1(\lambda)\times T(r) + N_2(\lambda)\times\{1 - T(r)\} \quad , \tag{2}$$

where,

N(r, λ) is the effective refractive index of the material as a function of wavelength, $r = \sqrt{x^2 + y^2 + z^2}$ is the radial position, from the center of material coordinates, λ is the wavelength,
$N_1(\lambda)$ is the user defined refractive index of the first GRIN material as a function of wavelength,
$N_2(\lambda)$ is the user defined refractive index of the second GRIN material as a function of wavelength and
T(r) is the radial polynomial function that describes the fraction of material that is

The radial polynomial function, T(r), is defined as below:

$$T(r) = \left[\sum_m t_m (r/R)^m\right]^n , \tag{3}$$

where,
t_m is the user defined coefficient (real number),
n is a user defined real number,
m is a user defined positive integer with summation starting from 0, and
R is the user defined maximum radius of the GRIN material.

The maximum and minimum values of *T(r)* are user defined. Beyond these bounds the value of T*(r)* stays constant and is equal to the nearest bound.

The Luneburg lens is a special case of our spherical where $N_1 = 1$, $N_2 = 0$, $n = 0.5$, $t_0 = 2$, $t_1 = 0$, $t_2 = -1$. This results in the well known form of the classical Luneburg lens:

$$N = \sqrt{2 - (r/R)^2} \tag{4}$$

A cylindrical GRIN lens can be similarly modeled by making z = 0 in all the equations. Figure 5 shows a cubical rod (face = 6 mm width) with a cylindrical grin material ($N_1 = 2$, $N_2 = 0$, $R = 10$, $t_0 = 1$, $t_1 = 0$, $t_2 = -0.5$)

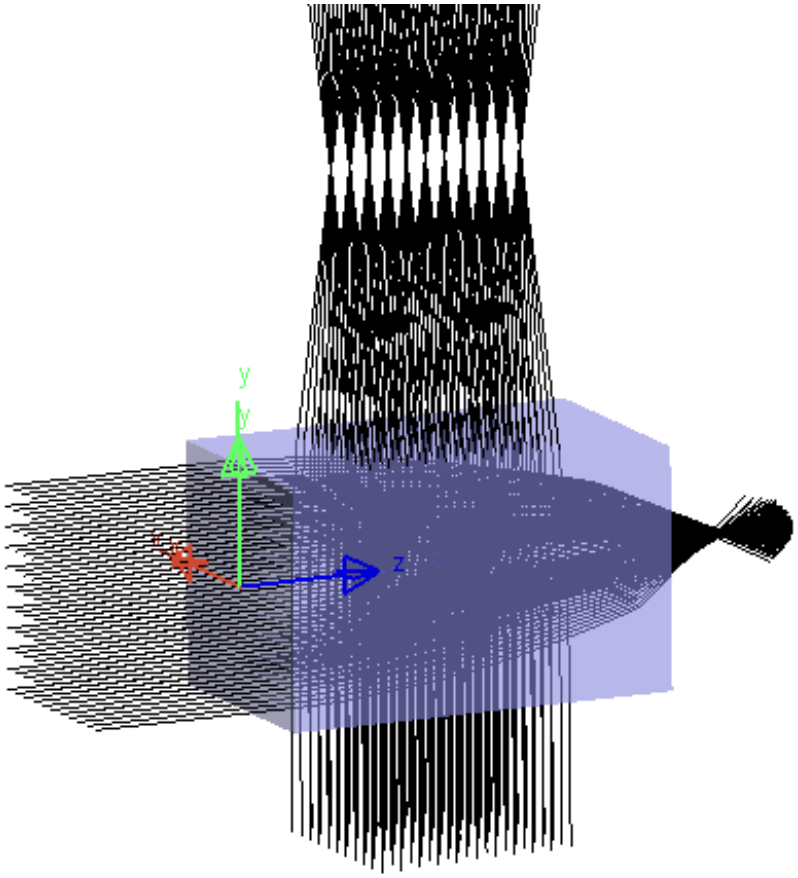

Figure 5: Material coordinate are aligned with object coordinate. A parallel bundle of rays along the z-axis focuses to a point. A parallel bundle of rays incident orthogonal to the cylinder produces a line focus.

4. Implementation in LightTools

Figures 6-10 show how the user defined GRIN is defined in the LightTools GUI

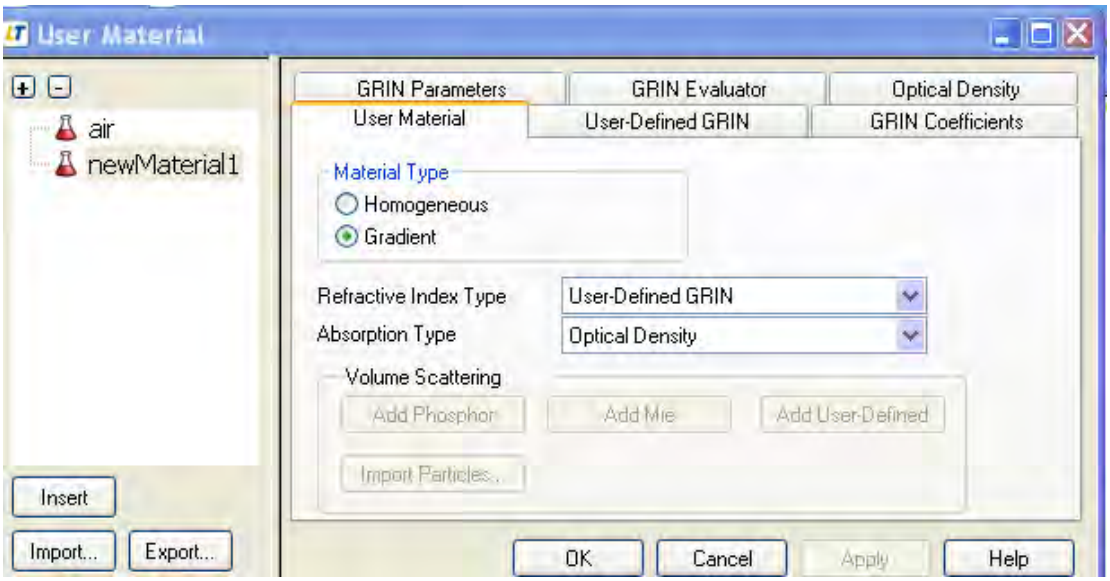

Figure 6: First tab in the LightTools L-GRIN GUI

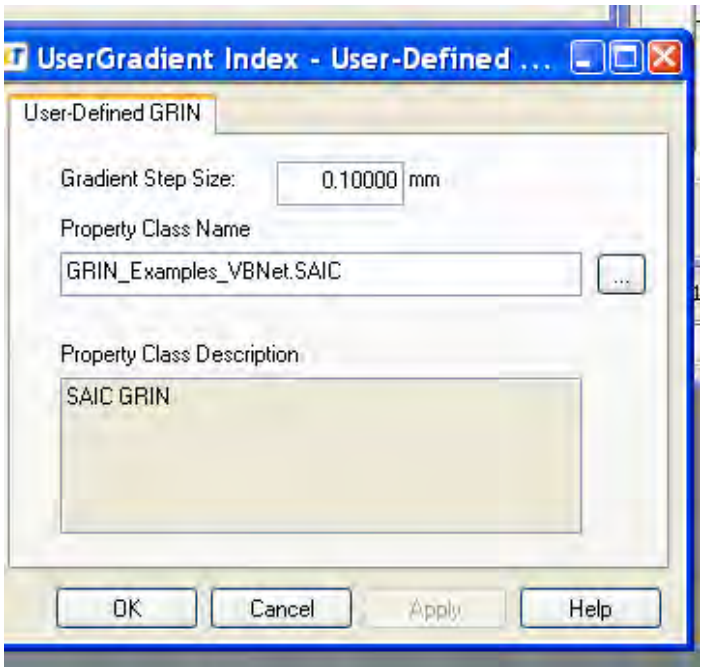

Figure 7: User Defined GRIN tab on the materials dialog box. The user specified the 0.1 mm step size for the ray to trace across the GRIN material.

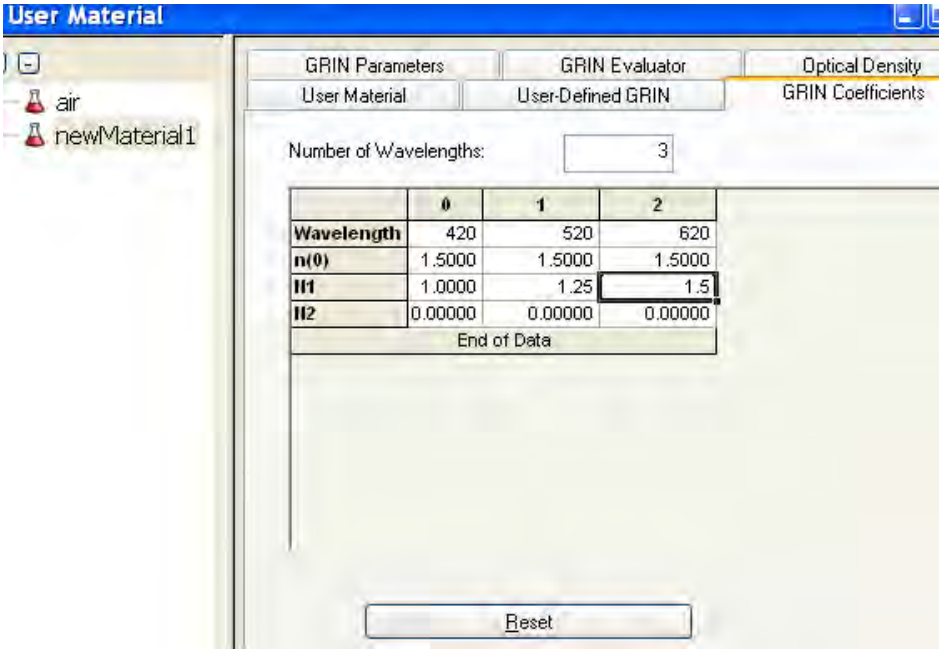

Figure 8: GRIN coefficients Tab on the material properties dialog box. The user specifies the refractive indices of N_1 and N_2 as a function of wavelength.

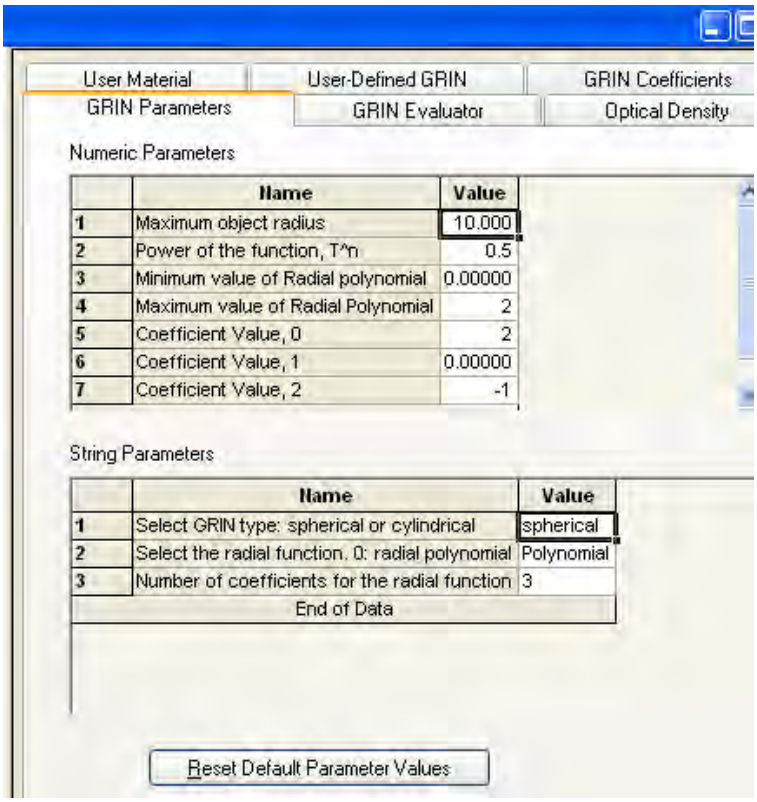

Figure 9: User defined GRIN parameters. Luneberg lens is implemented here as per Equation 4.

In LightTools, the material coordinate system coincides with the object coordinate system. LightTools provides the flexibility to translate and rotate the material coordinate system with respect to the object coordinate system as shown in the screen shot in Figure 10.

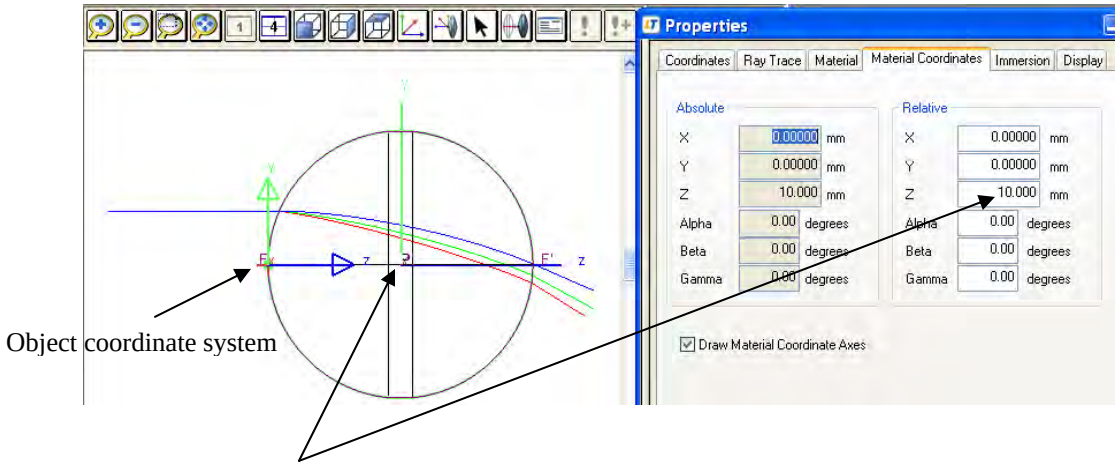

Figure 10: Material and object coordinate systems for a spherical lens with a 10 mm radius made up of Luneburg like GRIN material. The Material coordinate system is displaced by 10 mm in the z-axis. At 450 nm, the lens is the classical Luneburg lens. The red and green wavelengths have a different refractive index as per Figure 5.

The user can also pick GRIN materials from a user define catalog. Figure 11 shows a screenshot of the GUI.

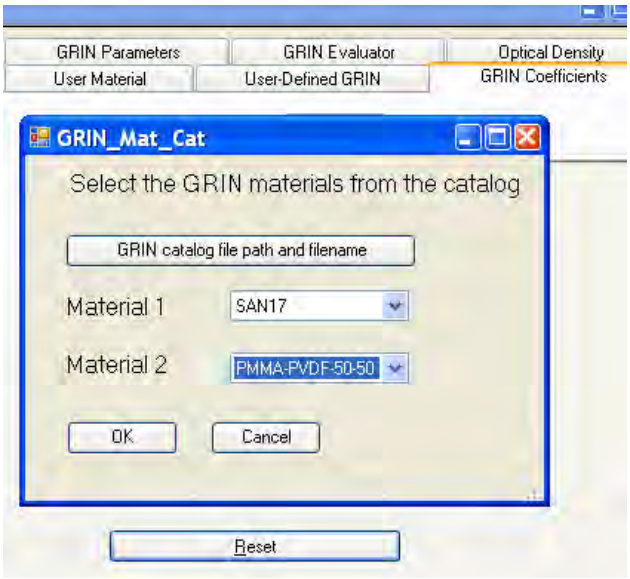

Figure 11: GUI for selecting the material from a user defined catalog of GRIN materials.

5. Optimizing the radial polynomial GRIN lens in LightTools

In this Section, we describe the optimization of a lens in LightTools. We want an 8 mm diameter lens to focus the light perfectly at a target 2 mm behind the lens. As a starting point, we input the parameters for a Luneburg lens ($N_1 = 1$, $N_2 = 0$) as shown in Figure 12.

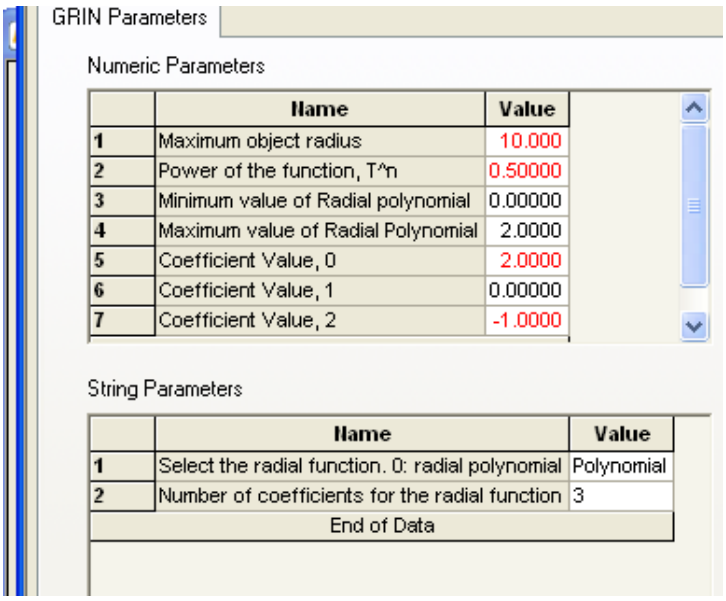

Figure 12: GRIN parameters declared as variables (in the red).

Figure 13 shows the initial configuration shows the ray trace of our initial Luneburg lens. Note that because the focus is offset from the surface of the sphere, the rays do not come to sharp focus as they do in the Luneburg lens in Figure 1.

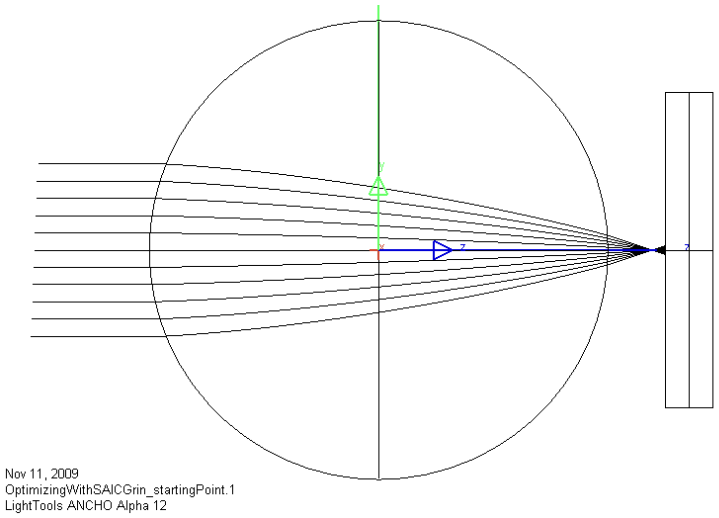

Figure 13: GRIN material to be optimized. The rays do not foucs "tightly" at the target.

To perform optimization in LightTools, the user has to to right click at the desired geometry description parameter and choose it to be a variable. The color of the parameter changes from black to red in the GUI. The user must then create a merit function to be achieved by changing the variables. In this case, the merit function is the setting that requires the y-coordinate of all the rays to be zero at the target location. The user then gives the command to optimize.

Figure 14 shows the optimized design while Figure 15 shows the optimized values of GRIN variables.

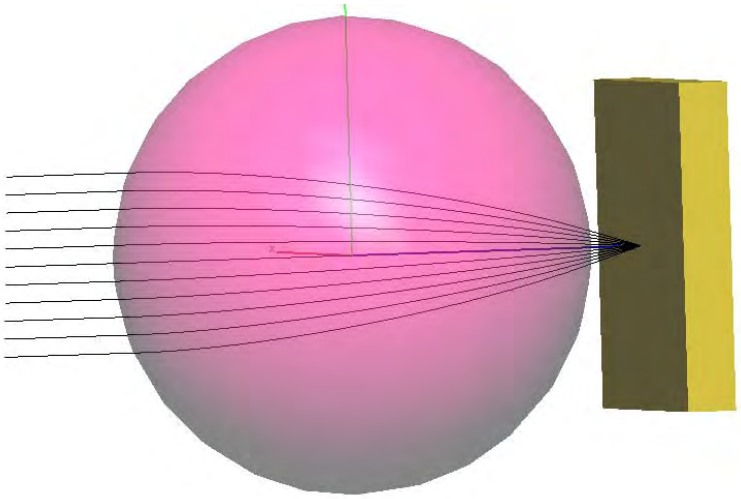

Figure 14: Optimized GRIN lens. The rays are brought to a tight focus at the target.

GRIN Parameters

Numeric Parameters

	Name	Value
1	Maximum object radius	9.0040
2	Power of the function, T^n	0.39012
3	Minimum value of Radial polynomial	0.00000
4	Maximum value of Radial Polynomial	2.0000
5	Coefficient Value, 0	1.9814
6	Coefficient Value, 1	0.00000
7	Coefficient Value, 2	-1.2091

String Parameters

	Name	Value
1	Select the radial function. 0: radial polynomial	Polynomial
2	Number of coefficients for the radial function	3
	End of Data	

Figure 15: Optimized parameters of the GRIN material (in Red).

7. Conclusions

ORA has provided a functioning utility that can be used to simulate and optimize spherical and cylindrical GRIN lenses based on two GRIN materials and a polynomial distribution function. We have added a user extensible catalog of materials, interpolation routines for refractive index, additional distribution functions, and other features requested by SAIC.

8. References

1 Luneburg, R. K. (1944). *Mathematical Theory of Optics*. Providence, Rhode Island: Brown University. pp. 189–213.
2 Brown, J. (1953). *Wireless Engineer* **30**: 250.
3 Gutman, A. S. (1954). "Modified Luneberg Lens". *J. Appl. Phys.* **25**: 855. doi:10.1063/1.1721757.
4 Morgan, S. P. (1958). "General solution of the Luneburg lens problem". *J. Appl. Phys.* **29**: 1358–1368. doi:10.1063/1.1723441.

USER MANUAL FOR GRIN FUNCTIONALITY IN LIGHTTOOLS

Installation

Double click the file: DARPA_L_GRIN_Setup.msi and accept the installation defaults. It will install the files necessary to define a user specified L-GRIN material. If the defaults are accepted, all the files will be located most likely in:

C:\Program Files (x86)\Optical Research Associates\DARPA_L_GRIN_Setup

(x86) is meant for computers deploying a 64 bit operating system.

This folder also contains the existing GRIN materials catalog file (GRIN_CATALOG_1.txt) for those materials that are going to be used for this project. The user can add new materials to this text file in a format that is described within the file.

The folder has two LightTools example files that show a simple lens made of a user-defined spherical L-GRIN material and optimizing the light focusing action by such lens by optimizing upon the L-GRIN material parameters.

Creating the L-GRIN material for a LightTools (LT) model

See the sequence of Figures below.

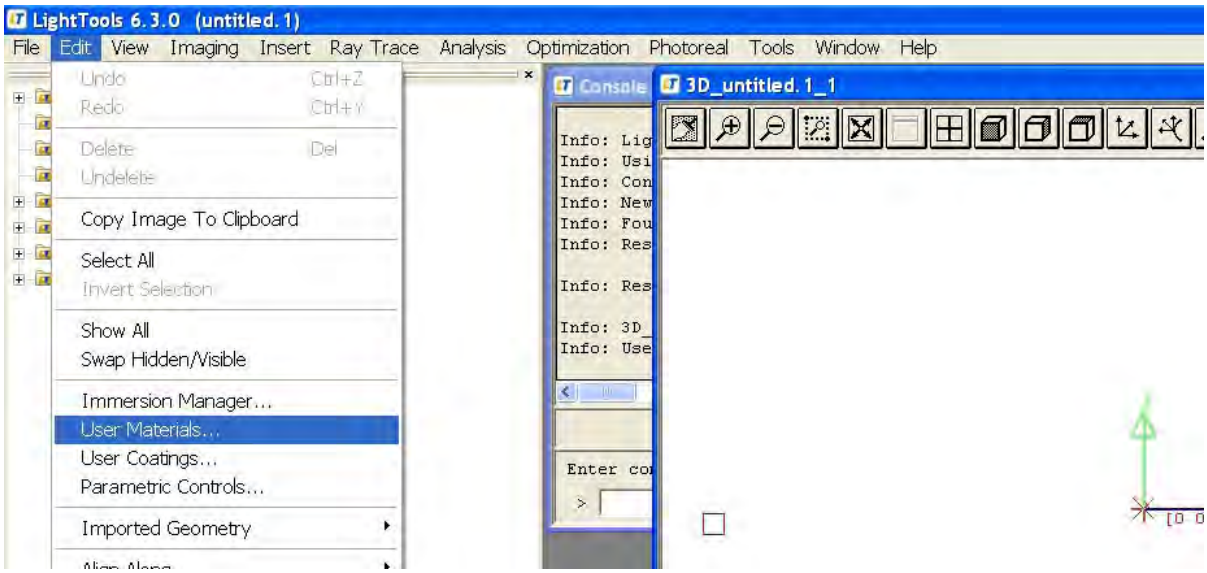

Figure U1: Click Edit -> User Materials

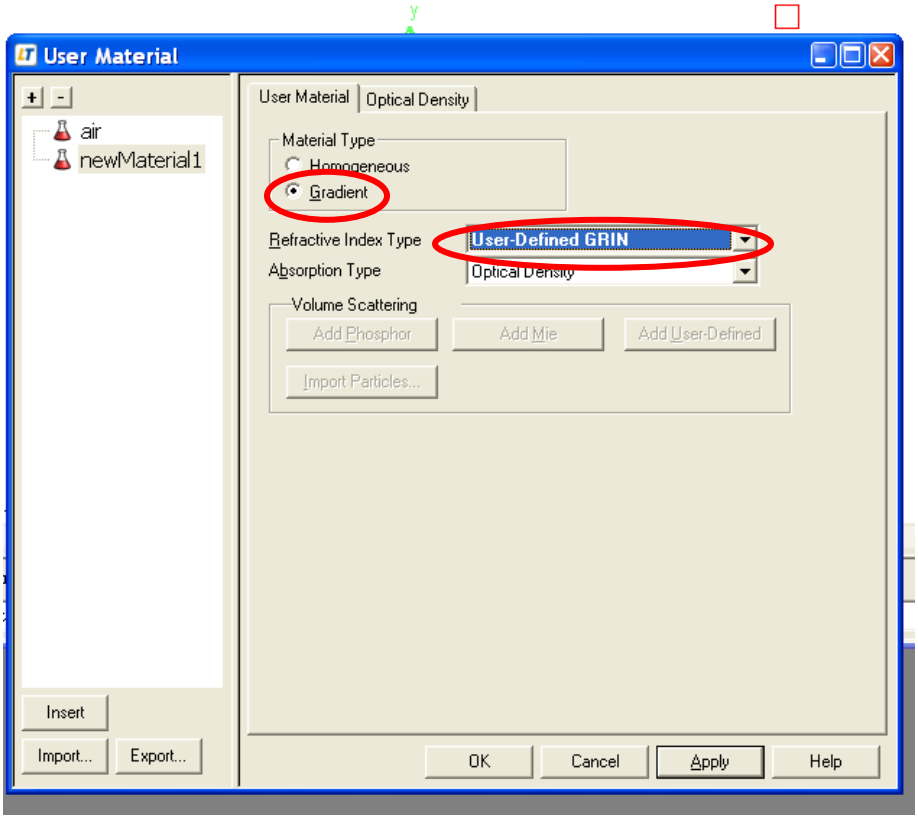

Figure U2: Click "Insert" and then select for the newMaterial1 as shown and click "Apply"

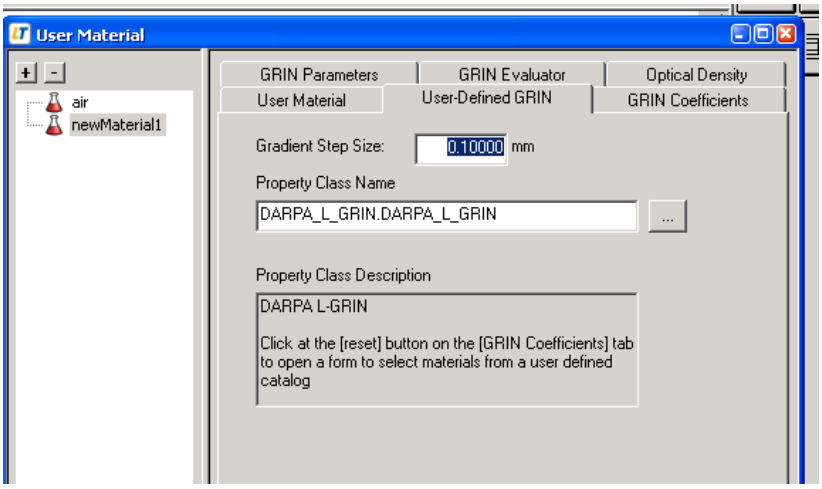

Figure U3: On the "User-Defined GRIN" tab adjust the Gradient Step Size if desired. Type in the "Property Class Name" textbox: DARPA_L_GRIN.DARPA_L_GRIN. This will load the L-GRIN material software. The property class description describes the basics of this material. To scroll down in the text box, click inside the text box and use up-down arrow keys from the keyboard.

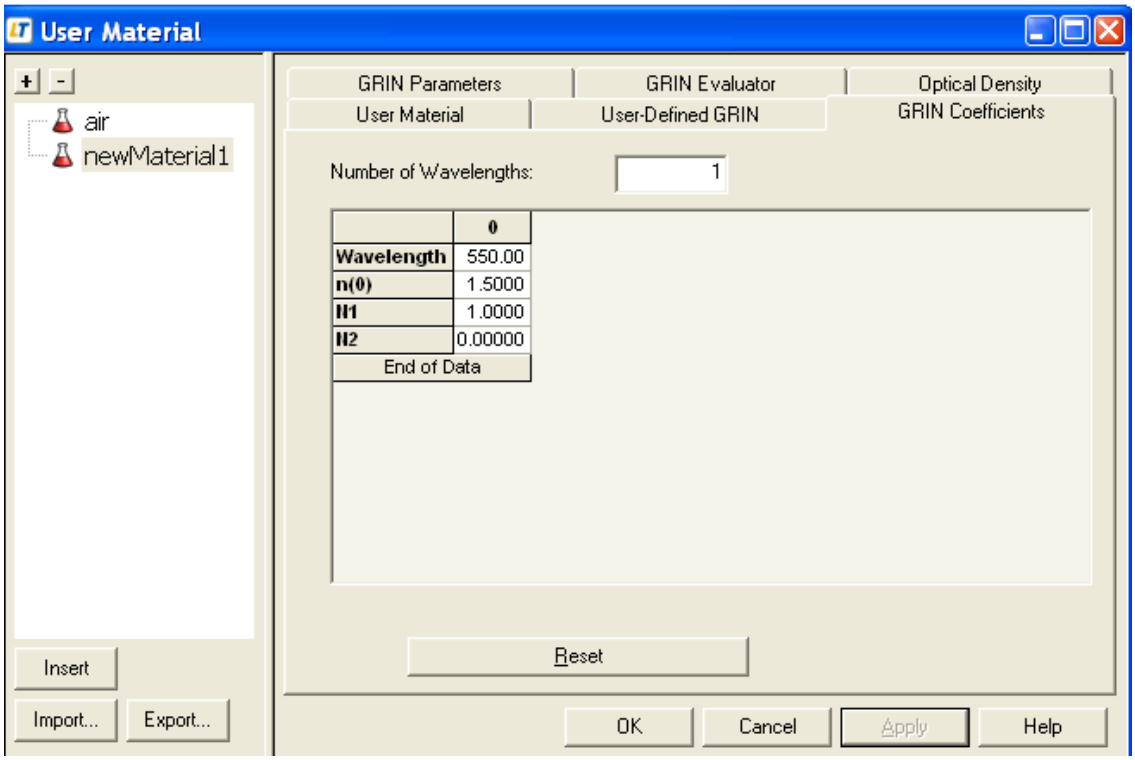

Figure U4: On the "GRIN Coefficients" tab fill in the required details: "Number of Wavelengths", Wavelength values in nm, ignore n(0) settings, N1 and N2 are the refractive index of the two GRIN materials being used. To access the GRIN catalog for L-GRIN, click at the "Reset" button.

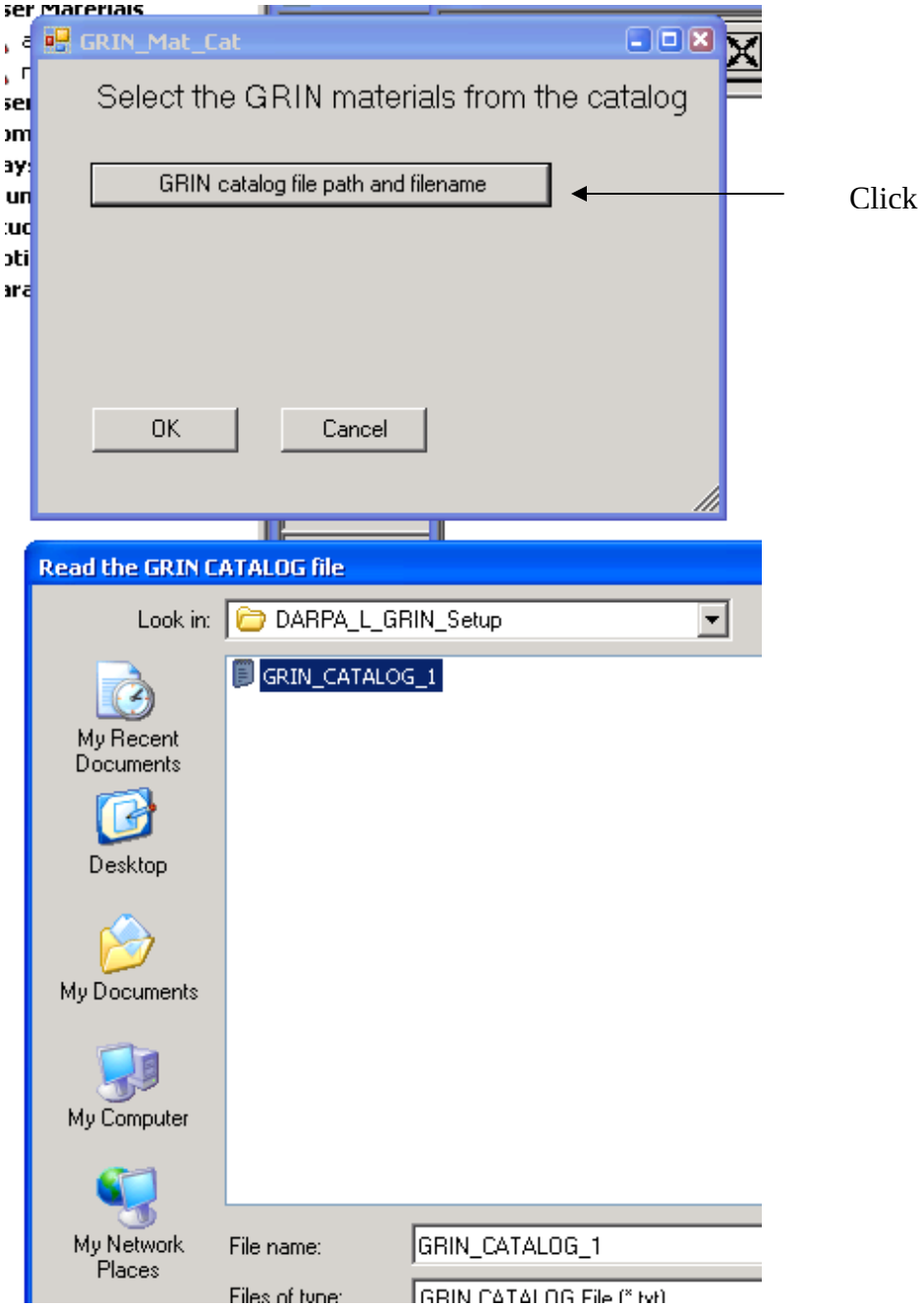

Figure U5: Select the user-created file "GRIN_CATALOG_1.txt"

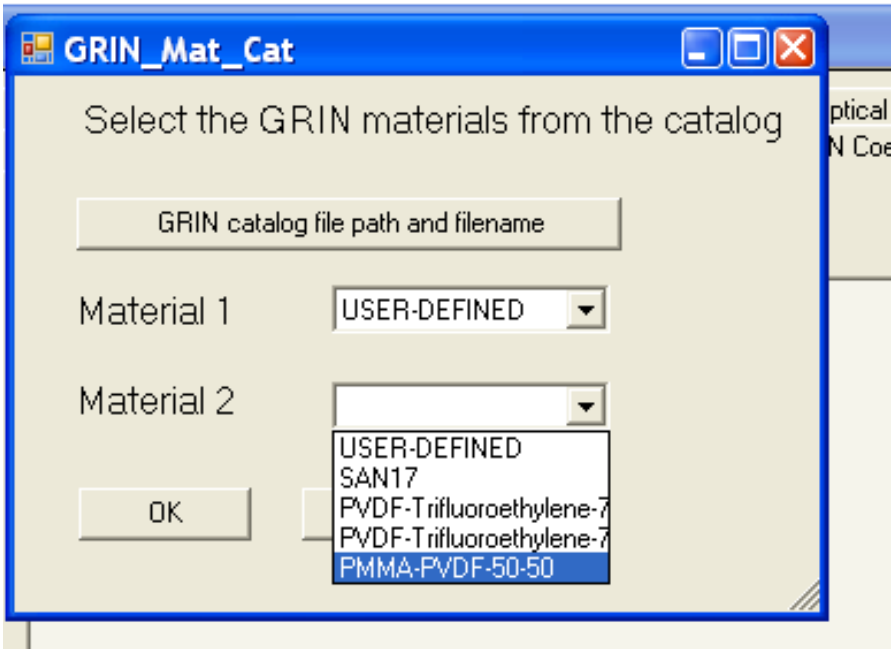

Figure U6: Select the two materials from the list boxes

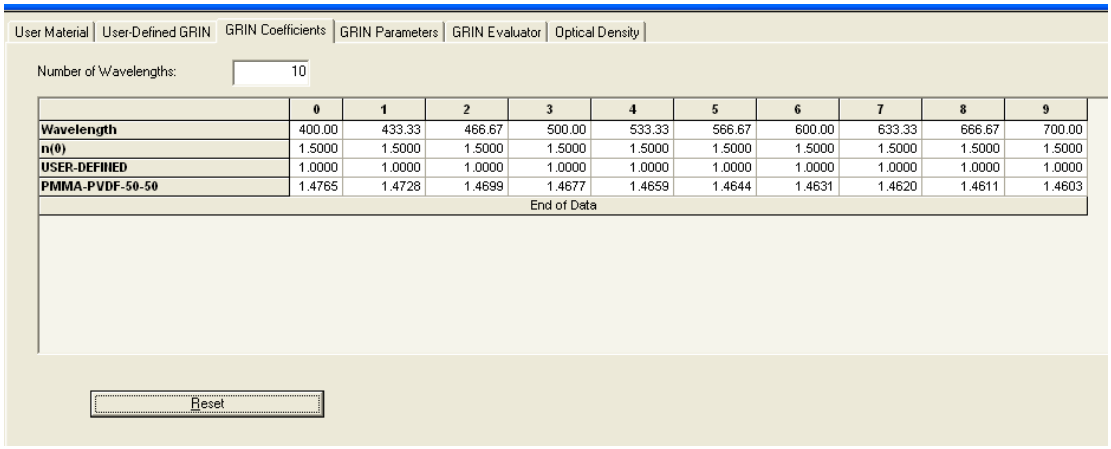

	0	1	2	3	4	5	6	7	8	9
Wavelength	400.00	433.33	466.67	500.00	533.33	566.67	600.00	633.33	666.67	700.00
n(0)	1.5000	1.5000	1.5000	1.5000	1.5000	1.5000	1.5000	1.5000	1.5000	1.5000
USER-DEFINED	1.0000	1.0000	1.0000	1.0000	1.0000	1.0000	1.0000	1.0000	1.0000	1.0000
PMMA-PVDF-50-50	1.4765	1.4728	1.4699	1.4677	1.4659	1.4644	1.4631	1.4620	1.4611	1.4603
End of Data										

Figure U7: Check the "GRIN Coefficients" tab. The two catalog materials are loaded. The number of wavelengths can be changed. The user can type in an arbitrary wavelength as well.

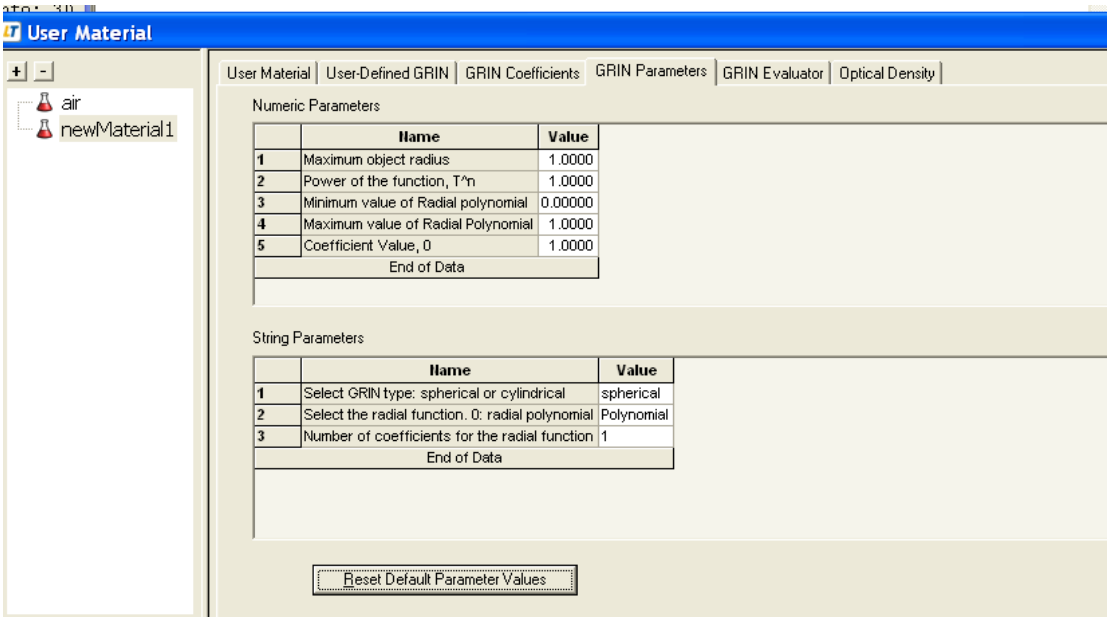

Figure U8: Click the "GRIN Parameters" tab and click at "Reset Default Parameter Values". Make selection as desired to define the L-GRIN material profile as per equations (2) – (4).

The material is now ready to be used. For example, make a "cube" object in LT and assign the new material to the object. Figure U9 shows the screen shot of the object properties. Notice the "material coordinates" tab. It allows the user to set the material coordinates relative to the object coordinates.

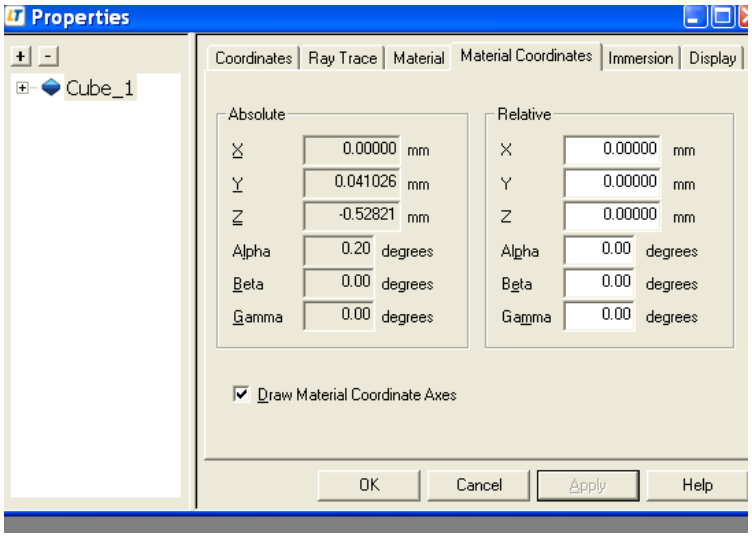

Figure U9: "Material coordinates" tab gives the user the option to change the material coordinates relative to the object coordinates.

University of Rochester Final Report

This report reviews research and projects for gradient index (GRIN) optics. Initial work on GRIN dispersion for use in spectrometers, and GRIN optics for curved image plane design, such as an intraocular lens, are discussed. Techniques for modeling and accurately measuring GRIN components are presented, and additional GRIN optics research and potential applications are also presented.

1. GRIN Dispersion

Spectral splitting has many important applications from chemical analysis and material classification to remote sensing and detection. There are various methods for splitting spectra into constituent parts, and these can be broken into three general types: diffractive, interference, and refractive. Diffractive techniques work well at longer wavelengths but become less sensitive as short wavelengths. Interference techniques also work well for longer wavelengths but require tight tolerances for short wavelength applications. Refractive techniques work best with shorter wavelengths but have typically required highly wedged prisms or large distances to give sufficient spectral separation.

Since the wedge of a prism creates the separating effect, more wedge translates to more separation. The two important parameters for determining spectral separation are the dispersion of the material, or change in index of refraction with wavelength, and the orientation of the surface with respect to the incident light. Spectrum splitting occurs only at the interface of the material. We propose using an inhomogeneous medium to split the spectrum. In this way, the entire bulk of the material may be used toward the purpose of spectral splitting. This allows for more splitting in the same space as a traditional prism or for the same amount of splitting in a small space.

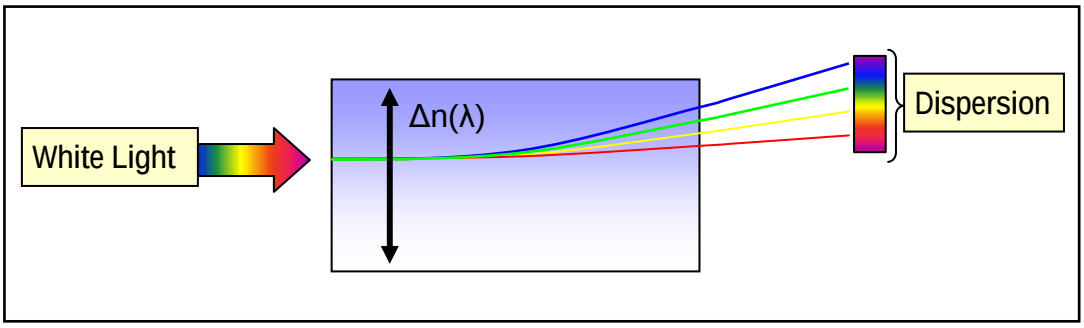

Figure 1: Schematic of a gradient index prism. The index of refraction varies as a function of height from low index at the bottom to high index at the top.

The amount of splitting is proportional to the "v-number" of the gradient. This v-number is a measure of the dispersion and is analogous to the Abbe number of a homogeneous glass. In homogenous material, this number is the ratio of the total index difference between red and blue light normalized by the index in yellow light:

$$\upsilon = \frac{n_{yellow} - 1}{n_{blue} - n_{red}}$$

Homogeneous dispersion equation

$$v_i = \frac{\Delta n_{yellow,i}}{\Delta n_{blue,i} - \Delta n_{red,i}}$$

Gradient dispersion equation

For glasses with large changes in index with wavelength, the difference between n_{blue} and n_{red} is large and the Abbe number is small. This translates to a larger color separation in a conventional prism. Conventional prisms are limited however by both materials and the amount of wedge one can introduce. Wedge is necessary because all of the color-splitting occurs at the surfaces. This is not a limitation of a gradient index prism however. Now, the color separation occurs throughout the material and large wedge angles are eliminated. Also, the choice of materials allows for tailoring of the dispersion profile. Figure 2 is a plot of the change in index with wavelength for some common polymer combinations. The v-numbers for these combinations range from +5.6 to -16.7, which are numbers impossible to achieve in homogenous systems and this is only a small sample of potential GRIN material combinations.

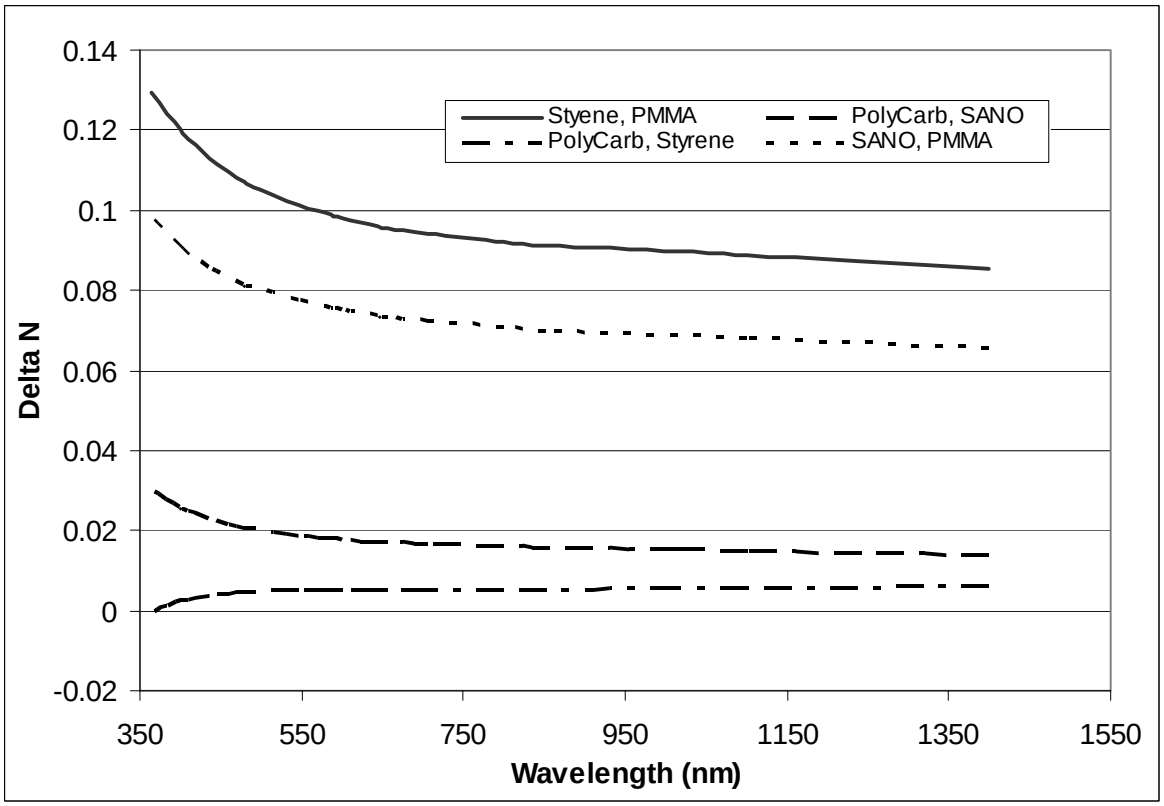

Figure 2: Plot of Δn versus wavelength for four combinations of common polymers.

One interesting feature of gradient index prisms is the ability to control the amount of dispersion by carefully choosing the materials used to form the gradient. Both index and dispersion can be controlled in this way. This allows for tailoring of the spectral splitting properties to suit a given situation or geometry. For initial studies, we chose two polymers with a large difference in index of refraction and a large difference in dispersion characteristics. The two polymers are poly(methylmethacrylate) PMMA and poly(styrene). Both of these materials transmit well in

from the near ultraviolet through the near infrared. Both materials are inexpensive, readily available, and have extensive optical material data available. The Δn versus wavelength plot is shown above for this material system (the top curve in Figure 2), with the gradient v-number being 9.3. This v-number is makes the gradient prism more dispersive than the most dispersive commercially available glass. Figure 3 shows the modeled chromatic separation of a collimated beam focused through a PMMA/Poly Styrene gradient index prism, and figure 4 shows the chromatic dispersion of visible light at the boundary layer of styrene monomer diffusing into MMA monomer in the laboratory.

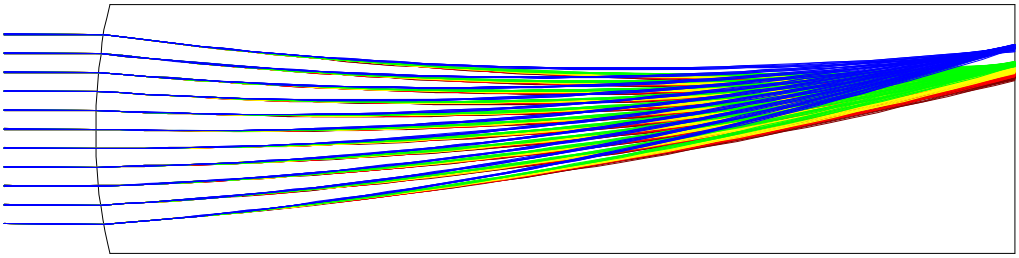

Figure 3: Modeled chromatic dispersion in linear GRIN PMMA/Styrene

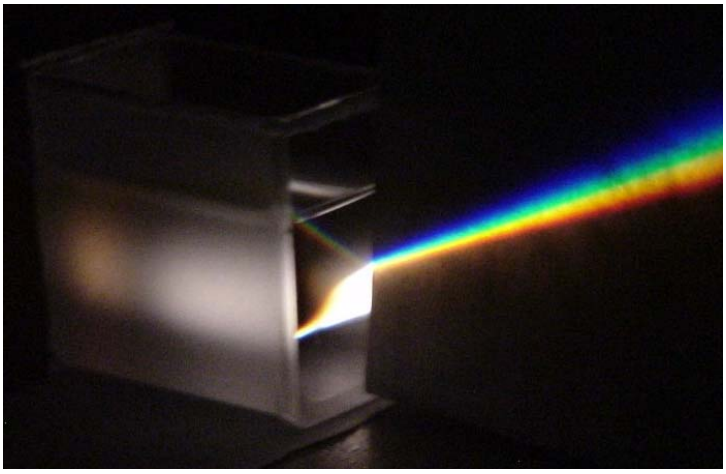

Figure 4: Chromatic dispersion at a Styrene/MMA monomer diffusion boundary.

Further study will also investigate the spot size reduction that occurs in gradient index materials. This is advantageous for spectrometers as a smaller spot, or slit, will result in a higher degree of spectral resolution. The spot size reduction that results in a gradient index material can often be observed by viewing the sun setting over the horizon. The thermal gradient index in our atmosphere can cause the sun to appear compressed, see figure 5.

Figure 5: The sun appears to be compressed by the thermal gradient index in the atmosphere.

2. GRIN lens design for curved image planes.

Many eyes designs found the animal kingdom are curved image plane designs that incorporate a GRIN lens. Figure 6 is the Octopus eye with spherical GRIN lens, and Figure 7 shows the human eye for two accommodated states that has a GRIN crystalline lens that changes shape.

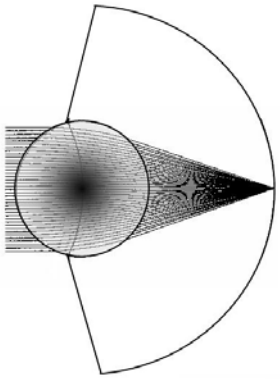

Figure 6: Octopus Eye

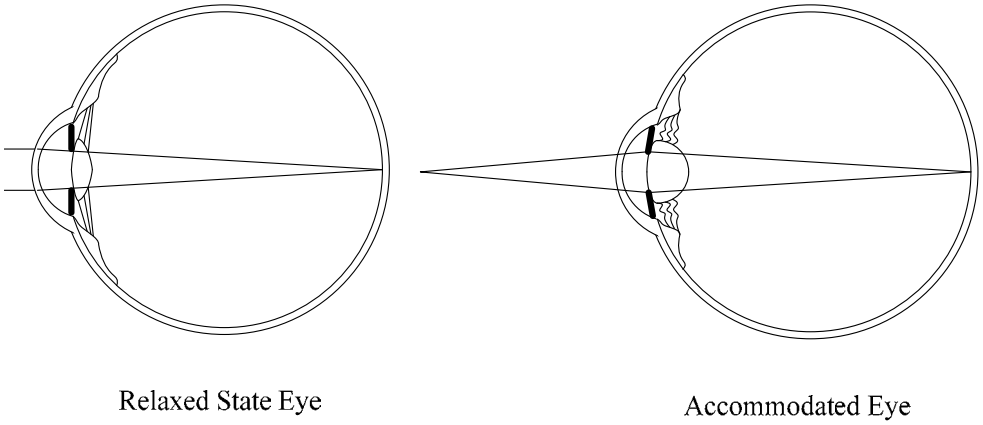

Figure 7: Relaxed and accommodated states of the human eye.

The GRIN lens provides additional focusing power, can reduce or correct aberrations, and material choice can lead to chromatic aberration reduction. These advantages are what allow the system to have so few optical components.

As humans age they suffer from presbyopia, the hardening of the crystalline lens and loss of ability to focus. Another more severe condition is cataracts, a clouding of the lens that impedes vision.

"Cataracts affect nearly **20.5 million** Americans age 40 and older. By age 80, more than half of all Americans have cataracts. Cataract surgery is the most frequently performed surgery in the United States, with more than **3 million** Americans undergoing cataract surgery each year. It is estimated that the federal government spends more than **$3.4 billion each year** treating cataracts through the Medicare program." *[Source: Vision Problems in* the U.S. report, developed by the National Eye Institute and Prevent Blindness America, 2002]

The common procedure is to remove the clouded lens and replace it with an intraocular lens. Adding a GRIN to intraocular lenses could significantly improve performance and is potentially achievable with an elastomeric material, allowing for accommodation.

The following is an example curved image plane design of the GRIN sphere lens is based on the idea of a Luneberg lens which is a variable-index, spherically symmetric refracting structure that will form perfect geometrical images between two concentric spheres on each other. The Lunerberg lens is theoretically perfect, but not practically manufacturable because the index at its periphery must match that of the surrounding medium and the required index gradient are usually too large. The following design introduces a homogeneous cladding around the GRIN sphere lens in the center. It does not take much spherical GRIN to correct both spherical and chromatic aberrations.

Design specifications

Focal Length = 4.23mm

F/2.2

Object at infinity

Field angle = 10°

Materials: Polycarbonate, PMMA

Homogeneous Cladding

Radius	2.5mm
Thickness	1.5mm
Material	Polycarbonate

GRIN Sphere Lens

Radius	1mm
Material	Mixture of Polycarbonate and PMMA
Index	$n(r) = 1.5225+0.003981r^2+0.01106r^4$

Third-order Aberrations

SA3	0.003421
TCO3	0.002449
AST3	0.000194
PTB3	-0.014768
DIS3	-0.003474

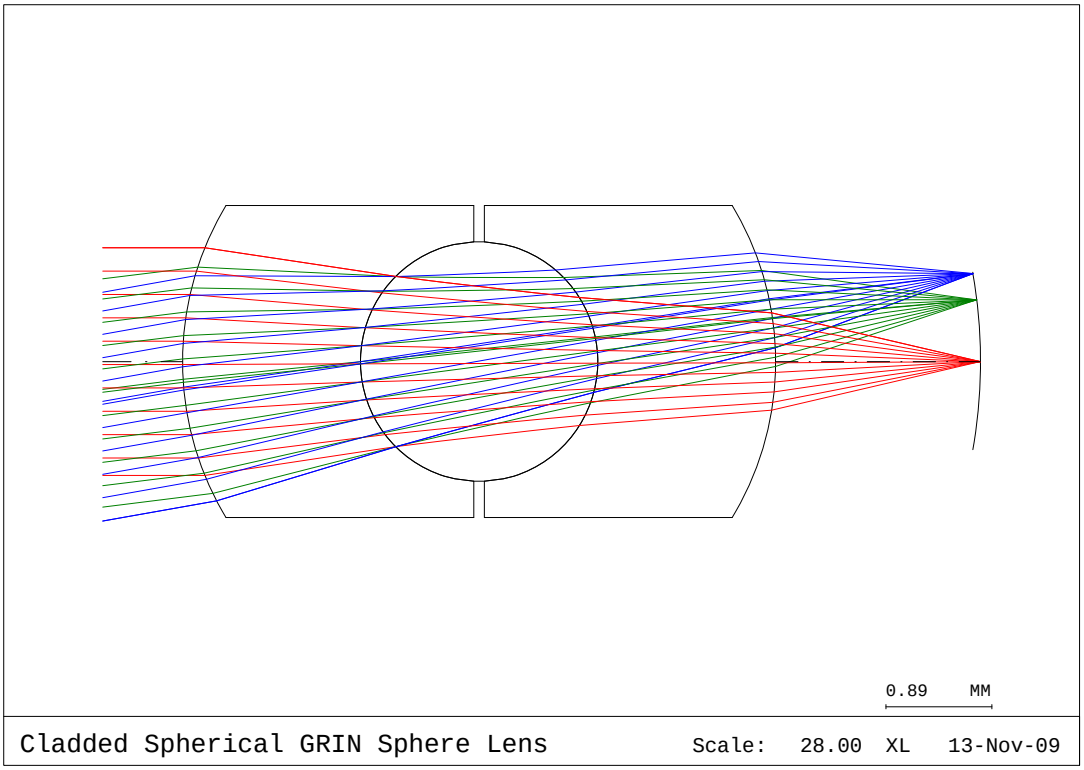
0.89 MM
Cladded Spherical GRIN Sphere Lens
Scale: 28.00 XL 13-Nov-09

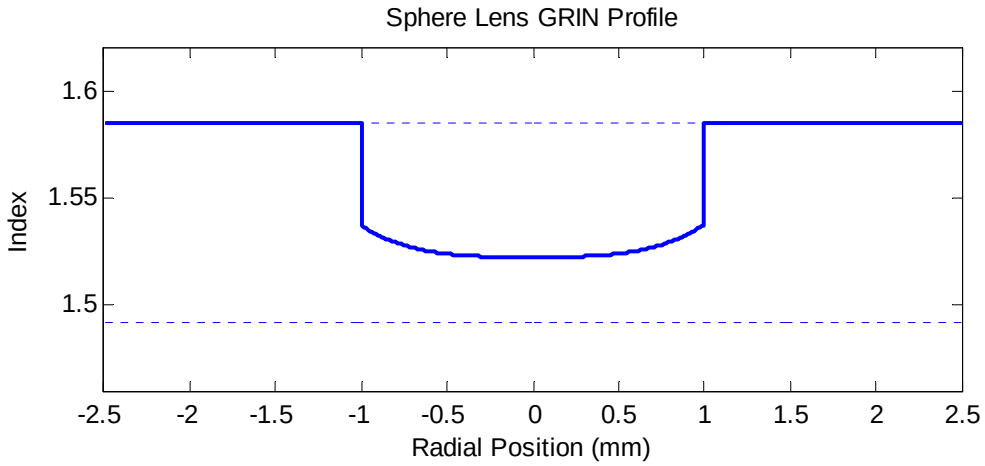
Sphere Lens GRIN Profile
Index
1.6
1.55
1.5
-2.5
-2
-1.5
-1
-0.5
0
0.5
1
1.5
2
2.5
Radial Position (mm)

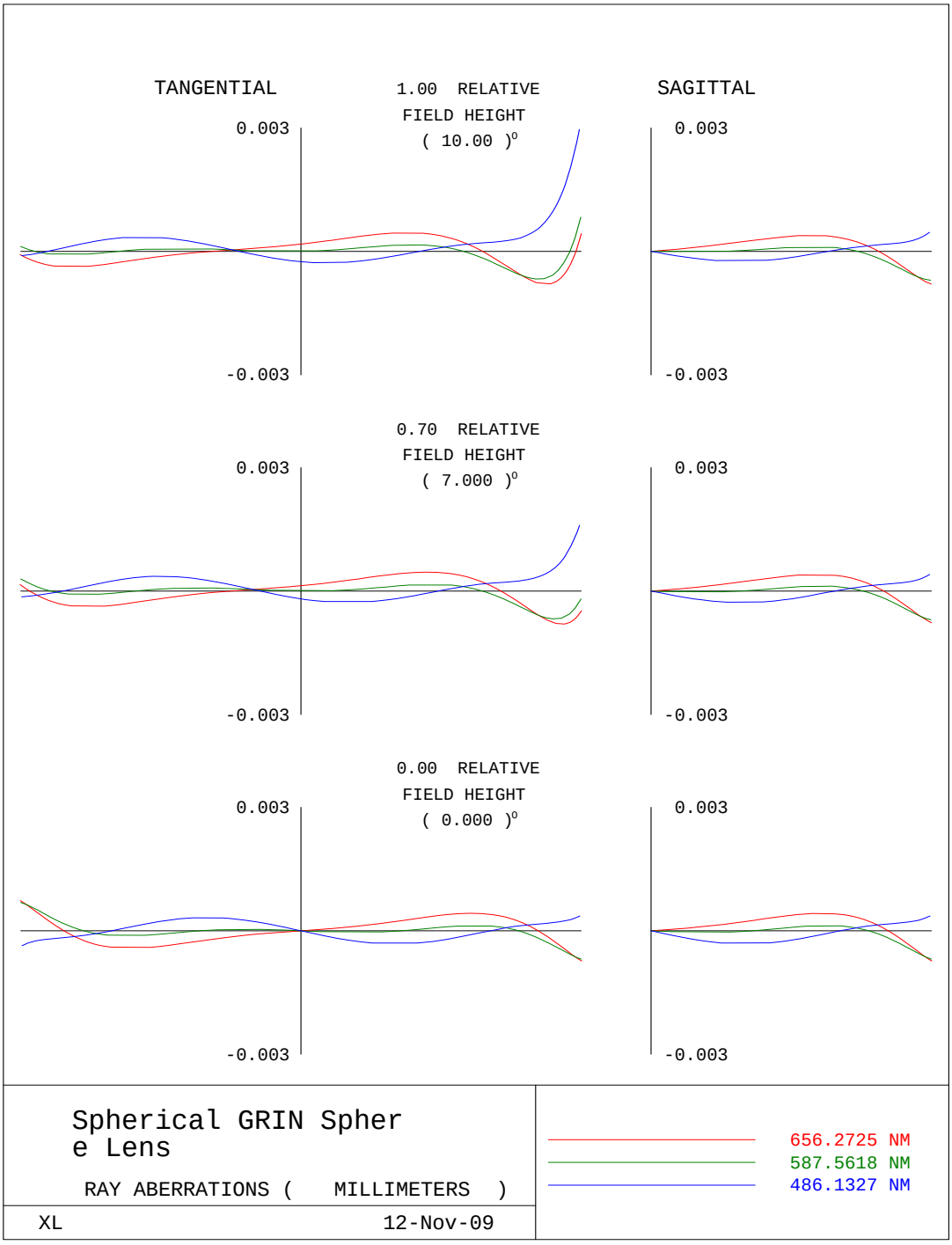
TANGENTIAL
1.00 RELATIVE FIELD HEIGHT (10.00)°
SAGITTAL
0.003
-0.003
0.70 RELATIVE FIELD HEIGHT (7.000)°
0.00 RELATIVE FIELD HEIGHT (0.000)°
Spherical GRIN Spher e Lens
RAY ABERRATIONS (MILLIMETERS)
XL
12-Nov-09
656.2725 NM
587.5618 NM
486.1327 NM

The next example is more applicable to the intraocular lens design. The following singlet uses spherical GRIN to correct chromatic aberrations while keeps the spherical aberration down.

Design specifications

Focal Length = 10mm

F/5

Object at infinity

Materials: Polycarbonate, PMMA

Radius 1	6.1109mm
Radius 2	-13.3680mm
Thickness	1
Index	$n(r) = 1.5009 - 0.01010r^2 + 0.002579r^4$

Third-order Aberrations

SA3	0.013525
TCO3	0.012005
AST3	-0.004299
PTB3	-0.003576
DIS3	-0.000434

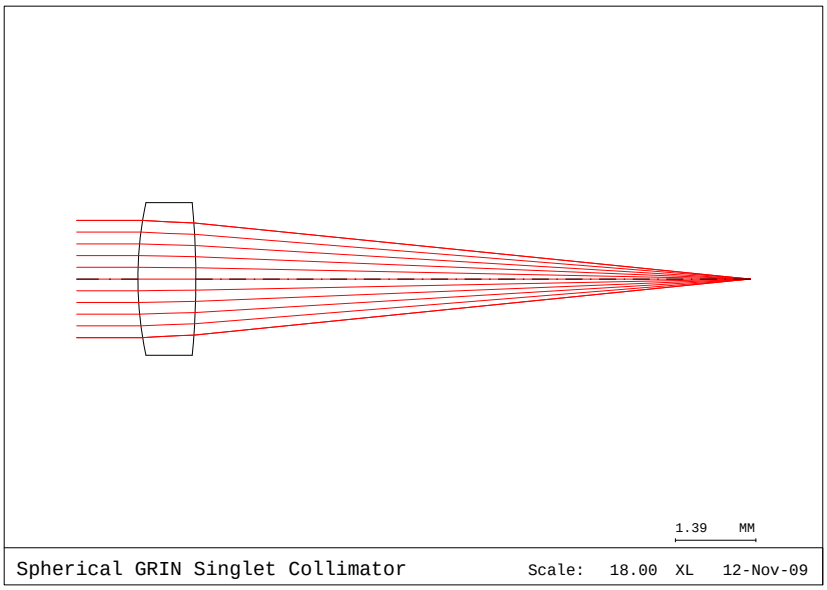
1.39 MM
Spherical GRIN Singlet Collimator
Scale: 18.00 XL 12-Nov-09

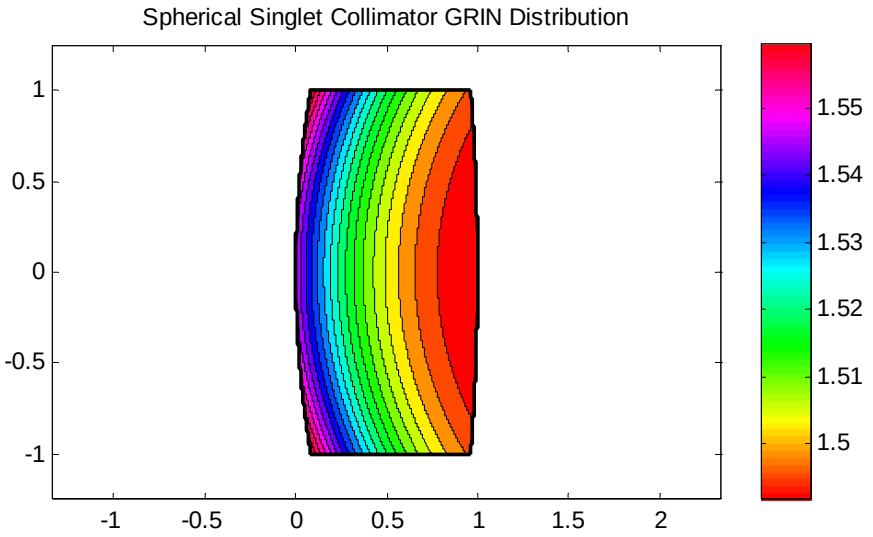
Spherical Singlet Collimator GRIN Distribution
1
0.5
0
-0.5
-1
-1
-0.5
0
0.5
1
1.5
2
1.55
1.54
1.53
1.52
1.51
1.5

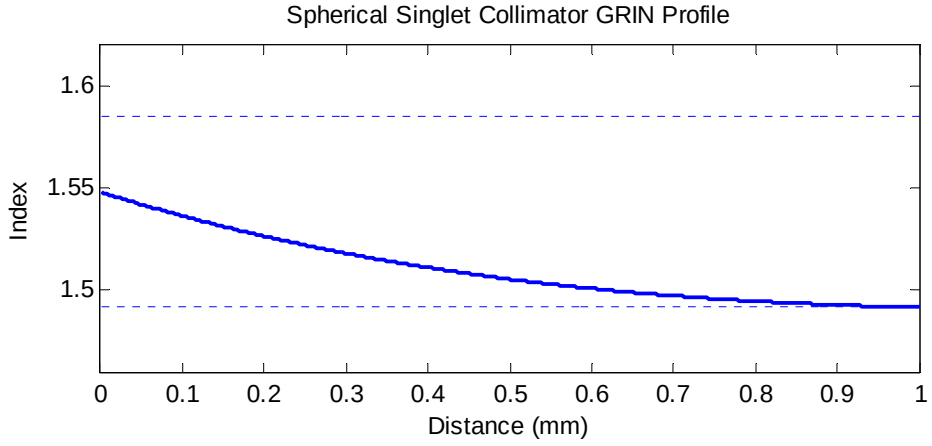
Spherical Singlet Collimator GRIN Profile
Index
1.6
1.55
1.5
0
0.1
0.2
0.3
0.4
0.5
0.6
0.7
0.8
0.9
1
Distance (mm)

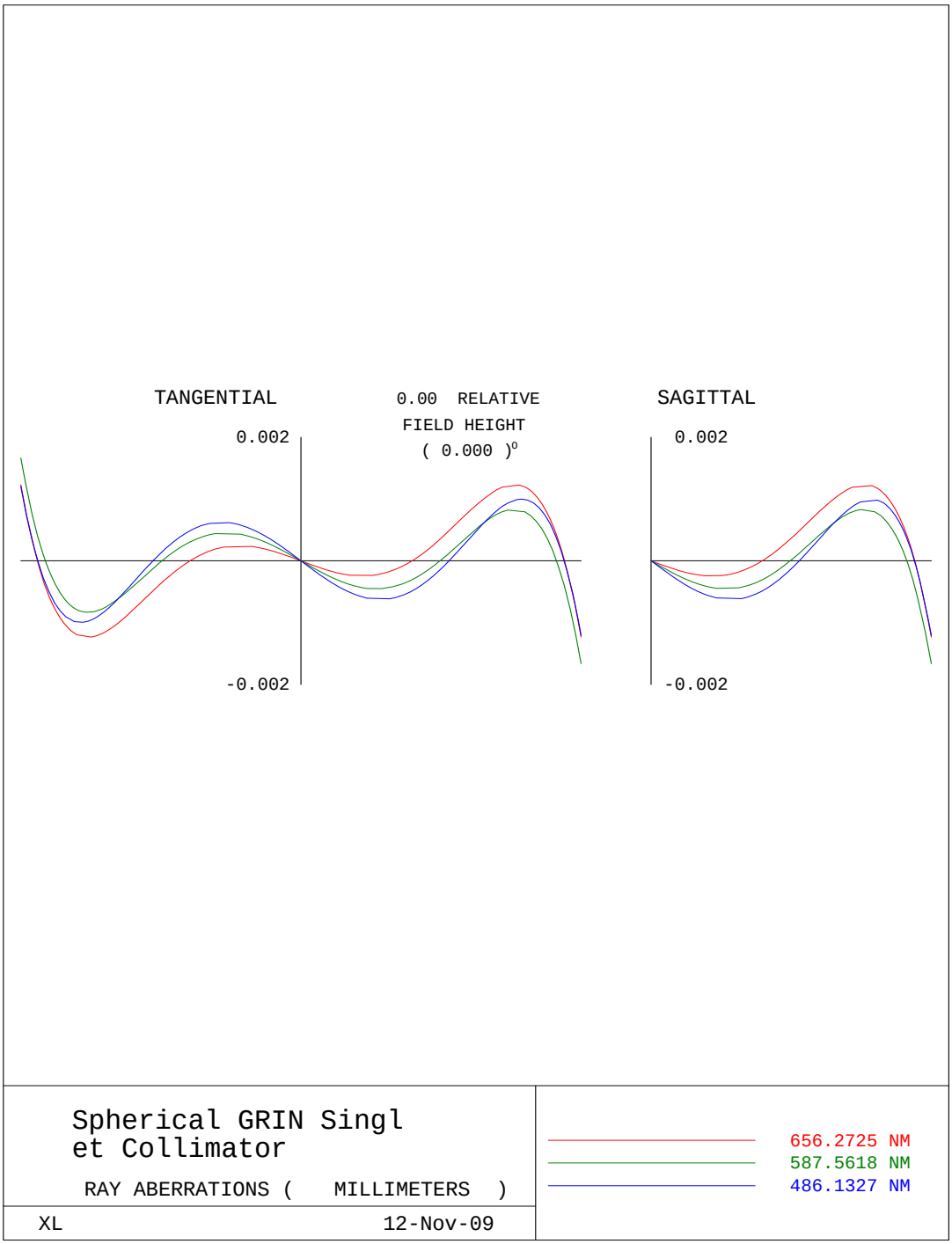
TANGENTIAL
0.00 RELATIVE
FIELD HEIGHT
(0.000)°
SAGITTAL
0.002
-0.002
0.002
-0.002
Spherical GRIN Singl
et Collimator
RAY ABERRATIONS (MILLIMETERS)
XL
12-Nov-09
656.2725 NM
587.5618 NM
486.1327 NM

A similar GRIN singlet lens is applied in a human eye model. If the crystalline lens is modeled as a homogenous polymer material, most aberrations except for chromatic aberration can be removed. When the homogenous lens is replaced with a PMMA/polycarbonate GRIN lens the chromatic aberration is dramatically reduced.

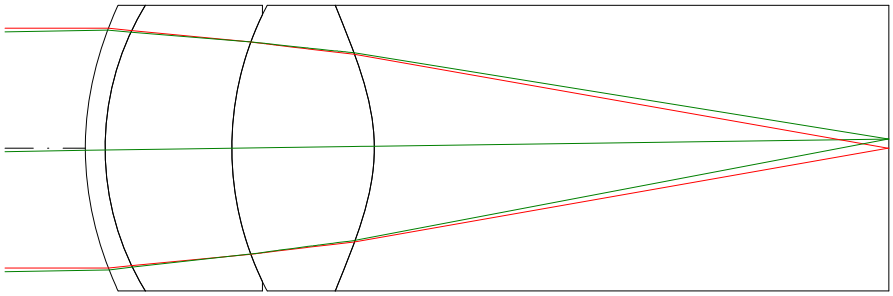

Figure 15: Human Eye Model in CodeV®

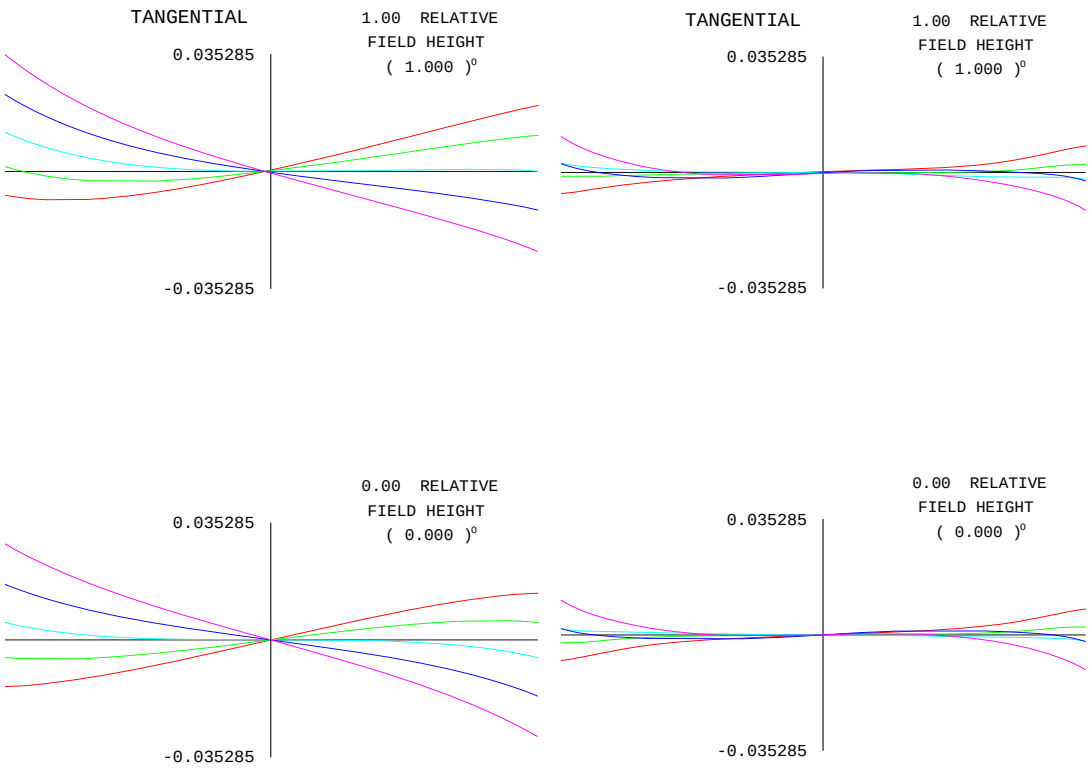

Figure 16: Ray aberration plots Left: Homogenous PMMA lens Right: PMMA/Polycarbonate GRIN lens.

3. Additional GRIN Applications

Utilizing aspheric surfaces and GRIN materials together in lens design may lead to significant improvement in many existing imaging systems. There is the potential to reduce the number of optical elements, improve image quality, reduce chromatic aberration, and possibly use lighter weight and less expensive materials. Below is short list of GRIN lens designs projects that can be reinvestigated:

- **Axial GRIN projects**
  - Night Vision
  - Riflescopes
  - Binoculars
  - Gunners Primary Sight
  - 35mm Camera Lens
- **Radial GRIN projects**
  - Boroscopes
  - Tapered Gradient Index Lenses

The point and shoot camera market is another key target area for the application of hybrid asphere/GRIN lenses, specifically cell phone cameras.

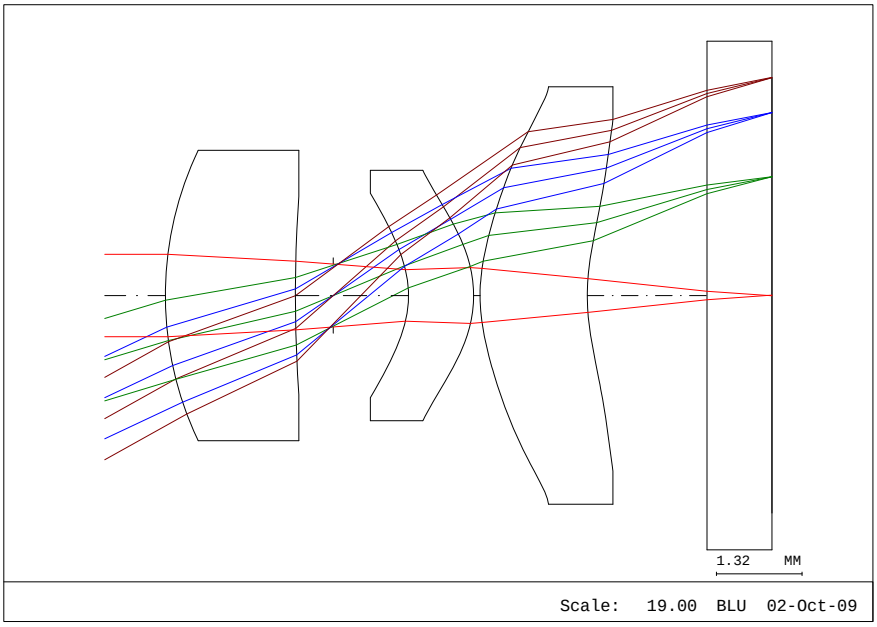

Figure 17: Common cell phone camera lens design.

Figures 18 shows two potential models in the early stages of design that utilize aspheric GRIN elements.

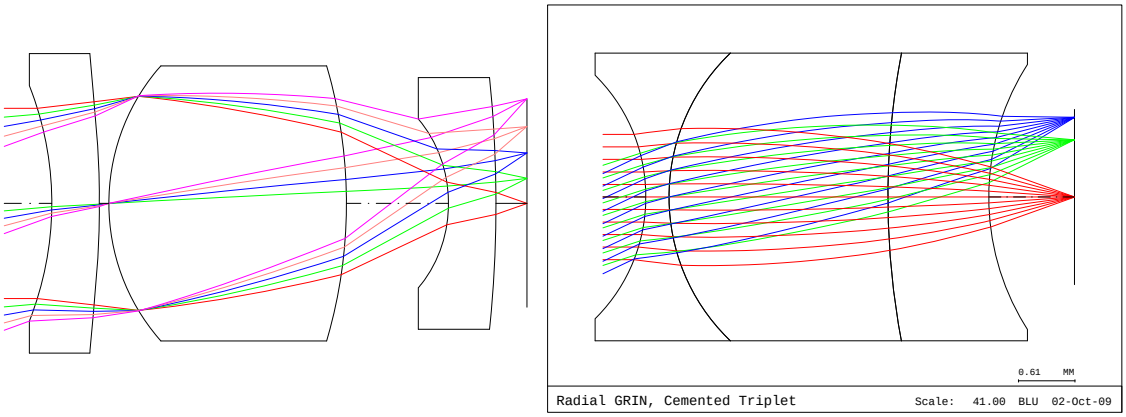

Figure 18: Aspheric/GRIN cell phone camera lens designs.

In addition to improving upon current designs, a key market advantage is to introduce zoom capability. Next generation demand will bring the standard point and shoot camera's 3x optical zoom to the cell phone market.

4. Gradient Index Modeling of Dynamic Materials

Research into the human crystalline lens has brought about the capability to model and understand dynamic gradient index materials. Here the research has been conducted based on the well known properties of the human eye. In the future these tools can be applied towards new dynamic GRIN materials.

As a single element zoom lens in the visual system, the human crystalline lens possesses unique optical and mechanical properties. The lens itself is an elastic material held in place inside the eye chamber by the zonule fibers attached to the ciliary body. The lens zooming function is mainly achieved by its own shape change, a process commonly referred to as accommodation.

The GRIN nature of the lens not only provides extra optical power for both relaxed and accommodated eyes, but presumably plays an important role in balancing and reducing eye aberrations and maintaining image quality. In a relaxed state, the crystalline lens is stretched by the force imposed on the lens equator by the zonule fibers, and thus forms a thin and flat shape. When the eye accommodates, the crystalline lens takes on a more spherical profile that has increased surface curvature and lens thickness. The eye accordingly acquires extra refractive power that allows for imaging for near objects. In addition to the apparent surface profile change, the lens GRIN also undergoes a change in profile.

In this study, a single equation is constructed for the lens GRIN and by changing the GRIN profile a dynamic eye model that provides the right optical power during accommodation is constructed and simulated using CODEV.

4.1 Radial-Symmetric Gradient Index Representation

The majority of GRIN crystalline lens models use the classic GRIN polynomial representation. In general, the refractive index profile for a radial-symmetric gradient lens can be written as

$$n(r,z)=\sum_{j=0}^{\infty}\sum_{i=0}^{\infty}N_{ij}r^{2i}z^{j} \tag{4.1}$$

where r is the radial coordinate, z is the distance along the optical axis. A typical continuous GRIN model uses polynomials up to the second order, which fits a parabolic GRIN profile.

$$n(r,z)=n_{00}+n_{01}z+n_{02}z^{2}+n_{10}r^{2} \tag{4.2}$$

4.1.1 Liou-Brennan Lens Model

To construct a single equation for lens GRIN profile, a template GRIN model is needed to provide index values at various radial and axial points. The chosen template is the crystalline lens model used in Liou-Brennan's schematic eye, as shown in Fig. 4.3. In their modeling work, the GRIN profile is defined by two equations,

$$n(r,z)=\begin{cases}1.368+0.049057z-0.015427z^{2}-0.001978r^{2} & 0<z<1.59\\ 1.407+0.0z-0.006605z^{2}-0.001978r^{2} & 1.59\le z\le 4.02\end{cases} \tag{4.3}$$

which indicates a dummy surface is inserted at $z=1.59mm$.

.

4.1.2 University of Rochester Single Equation Lens Model

The single equation for the entire crystalline lens GRIN profile is constructed as

$$\begin{aligned}N(r,z)=\;& N_{00}+N_{01}\cdot z+N_{02}\cdot z^{2}+N_{03}\cdot z^{3}+N_{04}\cdot z^{4}+N_{05}\cdot z^{5}+N_{07}\cdot z^{7}+\\ & N_{10}\cdot r^{2}+N_{20}\cdot r^{4}+\\ & N_{12}\cdot z^{2}\cdot r^{2}+\\ & N_{01'}\cdot z^{\frac{2}{3}}+N_{02'}\cdot z^{\frac{2}{5}}\end{aligned} \tag{4.4}$$

where the coefficients are

$$N_{00}=1.3675,\ N_{01}=3.6384\times10^{-2},\ N_{02}=4.5041\times10^{-4},\ N_{03}=1.548\times10^{-2},$$
$$N_{05}=-1.0577\times10^{-3},\ N_{07}=9.7575\times10^{-6},\ N_{10}=-1.9713\times10^{-3},\ N_{20}=-1.5484\times10^{-7},$$
$$N_{12}=-2.4527\times10^{-7},\ N_{01'}=8.7407\times10^{-3},\ N_{02'}=-1.9507\times10^{-3}.$$

In Eq. 4.4, three groups of terms have been chosen. The first group (z^2, r^2, z^4, r^4, z^2r^2 and a constant term) is for modeling the overall ellipsoidal shape of the isoindicial surfaces and the symmetrical distribution along the transverse plane. The second group (z, z^3, z^5, z^7) deals with the asymmetrical distribution along the optical axis for the regions where the absolute values of z are greater than one. The last two terms ($z^{2/3}$ *and* $z^{2/5}$) defines the asymmetrical distribution near the anterior vertex where the absolute values of z are much less than one. The reason to add two fraction power terms is to effectively simulate the steep curve of the GRIN profile around the anterior lens vertex. A comparison of the isoindicial surfaces for the Liou-Brennan model and U of R single equation model is shown in Figure 19. As seen from the bottom plots, the refractive index difference between these two GRIN profiles is less than 0.00005 radially and less than 0.00025 axially. This proves that the single equation model has the capability to accurately simulate the GRIN profile of a given template. In future study, if provided with enough measurement data on a real crystalline lens, the entire GRIN distribution profile can be reconstructed using this single equation model.

4.2 Single Equation Crystalline Lens GRIN Model for Accommodated Eye

The next step is to change the GRIN model from the relaxed state into the accommodated states. The following sections illustrate how a 10-diopter lens model is constructed that produces enough optical power for near vision.

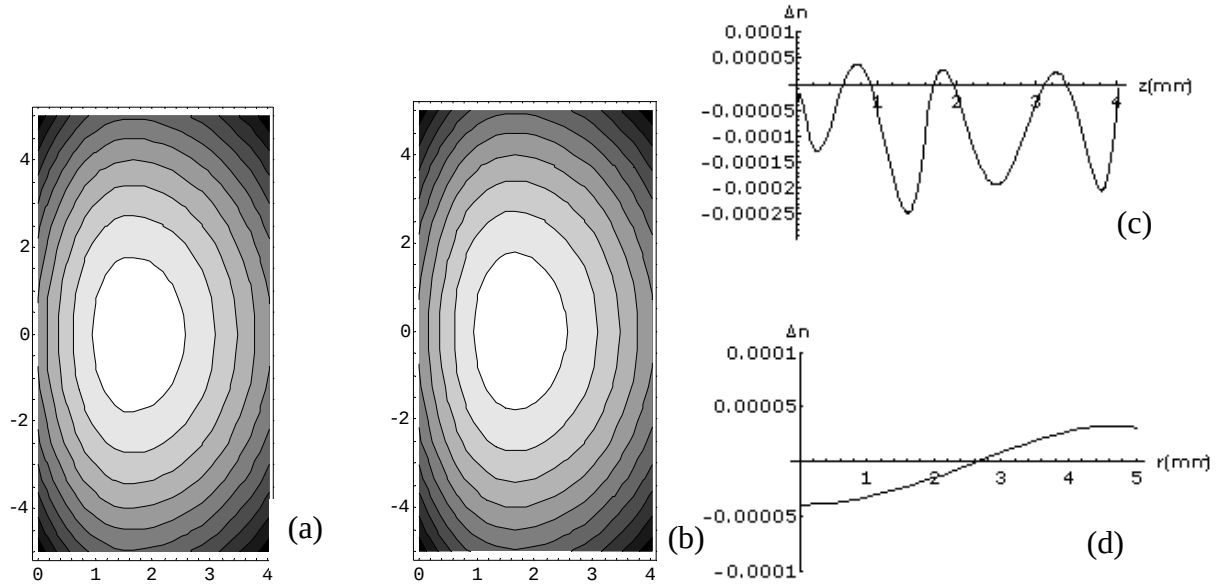

Figure. 19. Insoindicial surfaces plots of the crystalline lens GRIN for the relaxed eye, from Liou-Brennan's schematic eye[5] (a) and U of Rochester's single equation model (b), and their axial GRIN difference plot (c) and the radial GRIN difference plot (d).

4.2.1 Homogeneous Deformation Model for Accommodated Lens

The initial crystalline lens GRIN model for the 10-diopter accommodated eye is transformed from the relaxed state eye model described above under the equal-volume assumption. Because the lens thickness change after accommodation is very small (less than 0.4mm), the lens can be treated as an incompressible material. Therefore it assumes the volume of the crystalline lens is always conserved during the accommodation process. Any increase in axial lens thickness is offset by an equal proportion of decrease in lens width in the radial direction, or

$$\frac{\Delta d}{d}\cdot\frac{\Delta(r^2)}{r^2}=1 \qquad (4.5)$$

where d is the distance between the two vertexes of the lens, and r is the radius of the lens equator. The initial model also assumes the GRIN profile undergoes homogeneous deformation when the lens takes on the morphological changes. Hence the 10+ diopter lens basically has the same GRIN structure as defined in Eq. 4.4, except the axial and radial coordinates are rewritten as

$$\begin{aligned}\bar{z}&=\frac{d}{d+\Delta d}z\\ \bar{r}^2&=\frac{d+\Delta d}{d}r^2\end{aligned} \qquad (4.6)$$

where the factor $\frac{d+\Delta d}{d}$ is considered the expansion coefficient for lens deformation.

5. Absolute index measurement of a GRIN material

Interferograms provide accurate profile of the change in the index of refraction for GRIN materials, but they do not give any information about the absolute index. If a homogeneous region of the polymer is available it can be used as a reference point when the homogenous index is known, otherwise it becomes more complicated to make an accurate index of refraction measurement in a GRIN. Some methods are often destructive or have a large margin of error.

The University of Rochester GRIN group has developed a technique where reference points on the sample are found that match the index of the surrounding medium. Only one matching point is necessary and then the index of refraction at any point on the sample can be extrapolated from a GRIN profile measurement, or multiple measurements at different indices can be used to confirm the accuracy of the profile measurement.

The measurement is made in an interferometer (see Figure 20) on an edge of the sample that exposes the gradient index profile. The sample is placed in an optical cell and immersed in an index matching fluid that has an index somewhere within the gradient index profile. The cell is then placed in the interferometer and held at a steep angle that exposes the edge to be measured. An angle in the range of 30-45 degrees was adequate and does not affect the result.

Light traveling through most of the sample is unaffected, just a small shift due to change in optical path length from tilting the sample. However, the edge is no longer a sharp boundary. It

is shaped like a prism now, a region where the gradient index profile tapers down to zero thickness. The position where the index of the sample matches the index matching fluid is found by observing the behavior of the fringes in the prism shaped region. A fringe represents a path through the sample, cell, and index matching fluid that has equal optical path length. When a fringe in the sample reaches the prism region, it has to follow a path of equal path length and three things can happen. If the fringe is following a path where the index of the sample and index matching fluid are the same, it continues straight through because the change in thickness does not matter since the indices of the two materials are the same. If the index of the sample is lower than the fluid, then in the prism region the path straight to the edge will increase in optical path length. In this case, the path of equal optical path length curves toward lower index polymer in the sample to balance increasing volume of higher index fluid. If the index of the sample is higher than the fluid, then in the prism region, the path straight to the edge decreases in optical path length. In this case, the path of equal optical path length curves toward a higher index polymer to balance the increasing volume of lower index fluid. The position where the fringe does not deviate provides a reference point on the sample with a known index of refraction equal to the index matching fluid. Figure 5.1 illustrates light passing through the sample, and the behavior of fringes in the prism region on the near the index matched position.

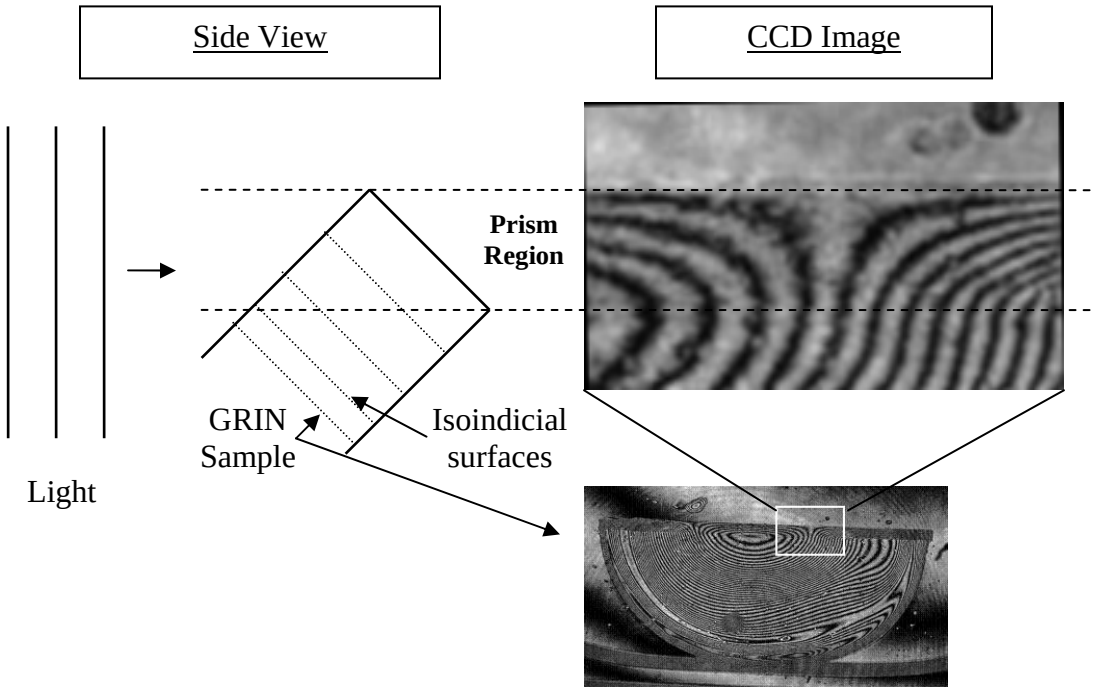

Figure 20. Identifying the absolute index of refraction by fringe deviation in an index matching solution.

The index matched positions are unaffected by any errors in the samples thickness or misaligned tilt in the interferometer, making it and excellent method for confirming accuracy of the profile measurements. If the profile is measured at the same time as the index measurement, the sample must be properly prepared to minimize thickness errors.

5.1 Example Measurement

A Dially Isophthalate DAIP, and mythyl methacrylate polymer diffurions GRIN sample, that has evaporation effects causing the index to rise back up near the boundary, is selected for a test case. The appropriate index matching fluid should match two positions near the edge to verify that the index does indeed rise back up. The peak index of the sample should be less than 1.57, the homogenous index of DAIP, so first the sample is immersed in n = 1.56. The positions matching n = 1.56 are noted in figure 5.1.2 A. An index matching fluid of n = 1.528 is selected that gives $\Delta n = 0.032$. It is slightly higher index so that two index matched positions should be visible near the left edge. The result is seen in figure 5.1.2 B and in figure 5.1.3.

Figure 21 is a blown up view of the two images side by side that shows how well the predicted index matched positions line up with the measured positions.

Index matching fluids used are from Cargille Laboratories. They are accurate to ±0.0002 with a temperature dependence $-dn/dT = 4.0*10^{-4}$.

These results confirm that using the index matching technique in combination with the interferograms can produce a quantitative measurement of the index profile. This experiment can be conducted at multiple wavelengths to accurately determine the Abbe value of a GRIN material.

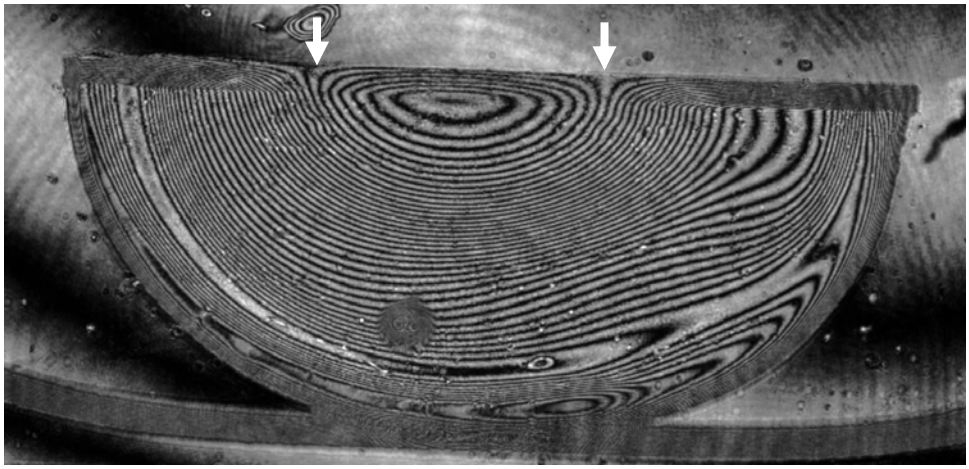

Figure 20 A)

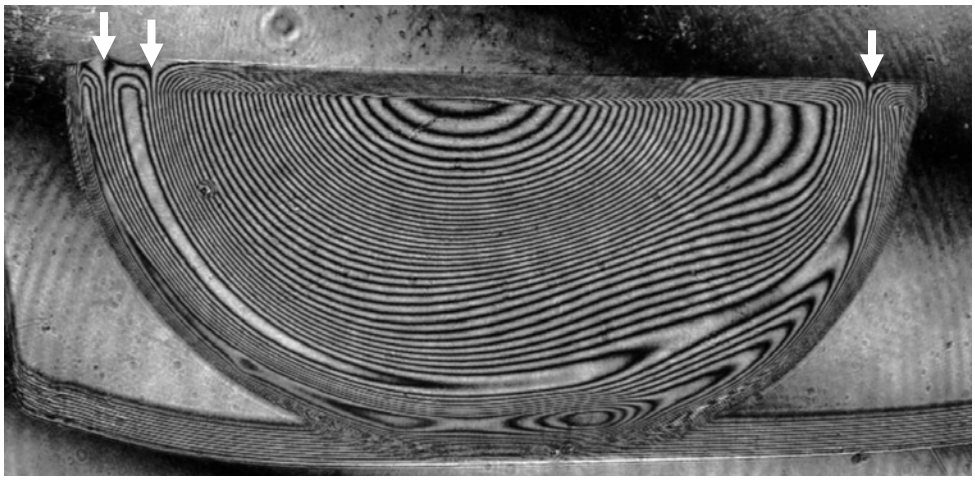

Figure 20 B)

Figure 20. DAIP-MMA sample.A) immersed in n = 1.56. B) Immersed in n = 1.528.Arrows denote index matched positions.

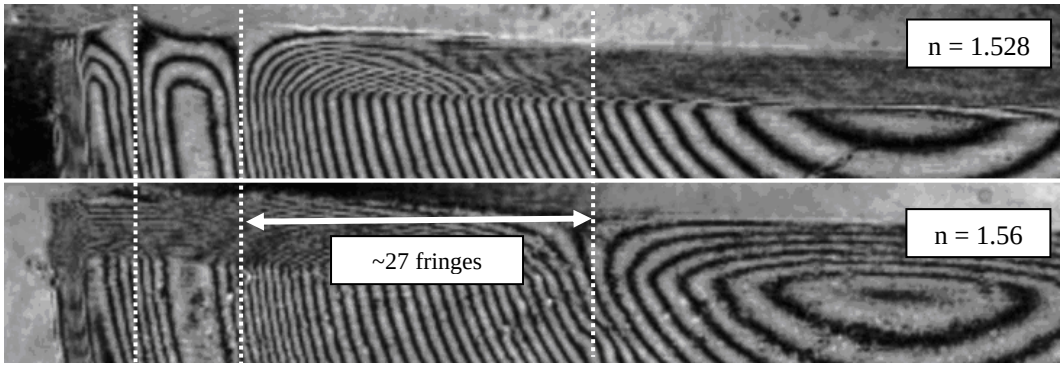

Figure 21. Side by side comparison of DAIP-MMA sample in two index matching fluids. n = 1.528 top, n = 1.56 bottom. The right most dotted line denotes the position that the high index fluid matched the index of the sample. The left two dotted lines denote the positions where the low index fluid was predicted to match with the sample.

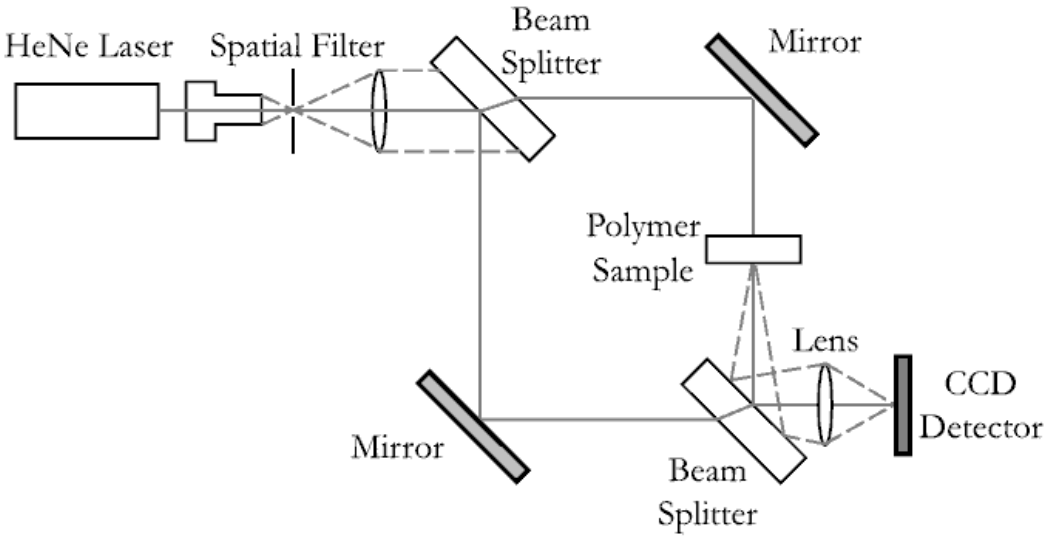

Figure 24. Mach-Zehnder interferometer used for GRIN profile measurements.